Doctoral Dissertation
Doctoral Program in Electrical, Electronics and Communications Engineering
(35th cycle)

Fast Solutions Strategies for Integral Equations in Electromagnetics with Applications to Brain Computer Interfaces

Davide Consoli

* * * * *

Supervisors
Francesco P. Andriulli

Doctoral Examination Committee:
Francesco P. Andriulli, Full Professor, Politecnico di Torino
Kristof Cools, Full Professor, Universiteit Gent
Paolo Rocca, Associate Professor, Università degli Studi di Trento
Amir Boag, Full Professor, Tel Aviv University
Roberto Graglia, Full Professor, Politecnico di Torino
Clément Henry, Associate Professor, IMT Atlantique
Adrien Merlini, Associate Professor, IMT Atlantique

Politecnico di Torino

I hereby declare that the contents and organisation of this dissertation constitute my own original work and does not compromise in any way the rights of third parties, including those relating to the security of personal data.

. . . .
Davide Consoli
Turin,

Summary

This thesis summarizes doctoral research activities on the development of new stable and accelerated solvers for electromagnetic integral equations and their applications. This work aimed at pushing the applications scenarios of numerical solver based on electromagnetic integral equations to new frontiers. The first phase included analytical and bibliographical research to better understand the issues that are encountered in some application scenarios. The results obtained during this phase have been published in the contribution “Adrian, Dely, Consoli, Merlini, Andriulli, *Electromagnetic integral equations: Insights in conditioning and preconditioning* , (IEEE Open Journal of Antennas and Propagation, 2021)”. Electromagnetic integral equations are often solved via the boundary element method (BEM). The BEM has interesting properties that make it one of the most appealing choices between the available numerical methods for electromagnetic scattering problems. Unfortunately, besides its advantages, it also suffers from ill-conditioning of the linear system to be solved. Some of the most relevant sources of ill-conditioning are the low-frequency breakdown, the dense-discretization breakdown, and high-frequency related issues. For this reason, in the work “Merlini, Henry, Consoli, Rahmouni, Dély, Andriulli, *Laplacian Filtered Loop-Star Decompositions and Quasi-Helmholtz Laplacian Filters: Definitions, Analysis, and Efficient Algorithms*, (arXiv:2211.07704, 2022)” we introduced a new class of preconditioners that are capable of simultaneously solving both low-frequency and dense-discretization breakdowns. Some of the numerical results relative to one of the schemes proposed in this work are reported in fig. 1 (fLS labeled curves), where the condition number is low and clearly not varying with frequency nor discretizaion.

Moreover, a new fast direct solver (FDS) for electromagnetic integral equation in the high-frequency regime was developed. In addition to be numerically stable and fast even at very high frequency, the new FDS results in a non-hierarchical skeleton compression of the involved operators. The solver can be efficiently applied to solve the problem for several different excitations. This thesis extends and details the scheme proposed in “Consoli, Henry, Dély, Rahmouni, Guzman, Chhim, Adrian, Merlini, Andriulli, *On the Fast Direct Solution of a Preconditioned Electromagnetic Integral Equation* (International Conference on Electromagnetics in Advanced Applications, 2022)”.

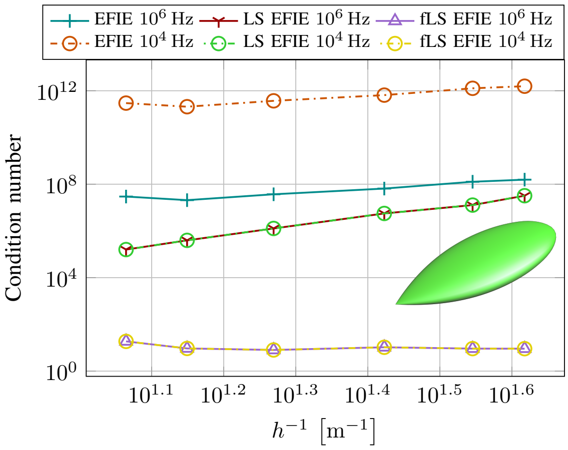

Figure 1: *Condition number of the EFIE, Loop-Star EFIE, and filtered Loop-Star EFIE as a function of discretization on the the NASA almond.*

Finally, among the applications of the developed solvers, a research front that was carried out during the doctoral studies concerns brain-computer interfaces (BCI). Our recent contributions on this front have been presented in "Micheli, Consoli, Merlini, Ricci, Andriulli, *Brain-Computer Interfaces: Investigating the Transition from Visually Evoked to Purely Imagined Steady-State Potential* (Annual International Conference of the IEEE Engineering in Medicine and Biology Society, 2022)". The scheme, based on visual imagery signals, overcomes the drawbacks of steady state visually evoked potential (SSVEP) based BCIs that, differently from our paradigm, need external stimuli for their functioning. Our current research on this front includes the creation of a new strategy that, leveraging brain imaging techniques based on electromagnetic integral equation solvers, improves the overall signal-to-noise ratio and, consequently, the accuracy of the BCI (preliminary results of the imaging technique are shown in fig. 2).

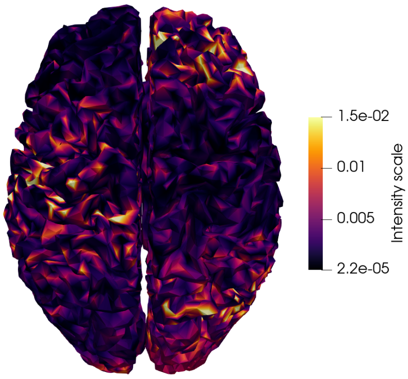

Figure 2: *Dipole activation obtained using ESI techniques on a trial of VI signals.*

Acknowledgements

> *Religion is a culture of faith;*
> *science is a culture of doubt.*
>
> Richard Feynman

Firstly, I am extremely grateful to my supervisors Prof. Francesco Andriulli for teaching me the pillars of the scientific method, the virtue of intellectual honesty and above all, the art of solving big problems in little time. Secondly, I would like to thanks Prof. Adrien Merlini for all his advice and support (both technical and psychological) during the past five years. My gratitude goes also to Prof. Clément Henry and Prof. Simon Adrian. Their plentiful experience and immense patience have encouraged me in all the time of my academic research and daily life. A special thanks goes to Damiano, Viviana, Paolo, Ermanno, Pierrick, Jhoann, Simone, Rui, Alberto and all the past members of the CERL@Polito. It is their kind help and sympathy that have made my workplace a happy environment for me.

In addition, I consider myself lucky to have gone through the lockdown with Clément, Alex, Tiffany and Maxime that being both flatmates and colleagues built a wonderful bridge between my private and working lifes, and the same goes for Francesca. Moreover, an incommensurable credit goes to all my friends for making my life so beautiful. Although I would like to mention all those who deserve it, I am blessed by the friendship of too many special people to do so, but I would like to thank particularly Luca, Paolo and Francesca (Camera caffè secondo Dante), who besides being excellent friends, when necessary they have always been also my remote and local shoulders to cry on, respectively. Finally, I would like to express my gratitude to my parents and to my family. Their tremendous understanding, encouragement and education gave me an intangible heritage without which it would have been impossible for me to complete this path.

Contents

List of Tables

List of Figures

Chapter 1

Introduction and Outline

In most of practical cases, such as antenna design or imaging applications, numerical methods are the only options for the solution of electromagnetic problems, since analytical solutions are available only for specific geometries (e.g. spheres). Among the numerical solvers from the computational electromagnetics (CEM) community, the ones based on electromagnetic integral equations, such as the boundary element method (BEM), show interesting properties in many practical scenarios. Chapter 2 introduce the theory of electromagnetics and the computation of electromagnetic fields via BEM, setting the notation used in following chapters.

Another advantage of BEM, compared to other numerical solvers such the finite element method (FEM), is that in case of homogeneous media, it is possible to discretize only the boundaries of the geometries involved in the problem. This translates into a reduced dimensionality and in a more computationally efficient solution of the problem. However, if employed in their standard version, they often suffer from numerical instabilities due to ill-conditioning of the linear system arising from the discretization of the problem. Some of the most the critical sources of ill-conditioning are the low-frequency breakdown, the dense-discretization breakdown and conditioning issues arising at simulation high-frequency. For this reason, part of this work deals with the development of new preconditioning strategies for electromagnetic integral equation solvers that cure the low-frequency and dense-discretization breakdowns. Details on the source of conditioning issues and the new preconditioning strategies are reported in chapter 3.

Unfortunately, differently form their competitors that rely on differential equations, the matrix arising from BEM is usually not sparse, and the inversion of a full matrix can lessen the computational advantage gained from the reduced dimensionality of the discretization. For this reason, to solve electrically large problems in feasible time, it is necessary to add acceleration techniques (i.e. fast solver) on top of the original BEM solvers. Indeed, part of the research work concerns the development of fast solvers suitable for different application scenarios. Combining them with ad-hoc numerical and preconditioning strategies allowed to develop a fast direct solver (FDS) that works in high-frequency, providing a direct inverse of the system. In addition to be numerically stable and fast, the new FDS results in a non-hierarchical skeleton compression of the involved operators. The solver can be efficiently applied to solve the problem for several different excitation, and it is presented in chapter 4.

Finally, chapter 5 is dedicated to brain-computer interfaces (BCIs). In particular, it presents a new BCI paradigm that overcomes some drawbacks of the BCI pipelines based on steady-state visually evoked potentials (SSVEP), that currently represent state-of-the-art BCIs in terms of bit-rate performances. In addition, it include the introduction of a strategy that leveraging electromagnetic brain modeling and imaging, based on integral equations solvers, aims at improving the classification accuracy of the BCI pipeline. Finally, chapter 6 concludes and discuss future works.

Chapter 2

Background and Notation

This work involves the study of surface electromagnetic integral equations in both the two-dimensional (2D) and three-dimensional (3D) cases. In this section, when not specified, the notation refers to the 3D case, since most of the derivations apply also to the 2D case. Given that this is not always true, when it can not be avoided, the notation is introduced separately for the two cases. Note that with the 2D case we actually refer to a 3D structure characterized by the same 2D section along one axis and that is infinitely long. This is for example a good approximation for the study of structures like wires or waveguides and a great test bench for formulations that will be further generalized to 3D.

2.1 Maxwell's Equations

The behavior of electric and magnetic fields in the presence of matter at macroscopic level is described by Maxwell's equations, and for this reason, any doctoral thesis in computational electromagnetics (CEM) should start with their definition. In the case of homogeneous dielectric media, the differential form of Maxwell's equations, expressed in terms of phasors, reads like

$$\nabla \times \boldsymbol{E} = -j\omega \boldsymbol{B} - \boldsymbol{M}, \tag{2.1}$$

$$\nabla \times \boldsymbol{H} = j\omega \boldsymbol{D} + \boldsymbol{J}, \tag{2.2}$$

$$\nabla \cdot \boldsymbol{D} = \boldsymbol{\rho}_e, \tag{2.3}$$

$$\nabla \cdot \boldsymbol{B} = \boldsymbol{\rho}_m, \tag{2.4}$$

where $\boldsymbol{E}$ is the electric field, $\boldsymbol{H}$ the magnetic field, $\boldsymbol{D}$ the electric induction, $\boldsymbol{B}$ the magnetic induction, $\boldsymbol{J}$ the electric current density, $\boldsymbol{M}$ the magnetic current density, $\boldsymbol{\rho}_e$ the electric charge density, $\boldsymbol{\rho}_m$ the magnetic charge density, and ω the angular frequency [51]. For simplicity, the space variable $\boldsymbol{r}$ has been omitted from all the quantities. Note that $\boldsymbol{M}$ and $\boldsymbol{\rho}_m$, as far as we know, are not physical quantities and are included only to symmetrize the equations and ease the following manipulations.

Alternatively, employing the constitutive relations ($\boldsymbol{D} = \epsilon \boldsymbol{E}$ and $\boldsymbol{B} = \mu \boldsymbol{H}$), the first two equations, describing respectively Faraday's law and Maxwell-Ampère law, can also be expressed as

$$\nabla \times \boldsymbol{E} = -j\omega\mu \boldsymbol{H} - \boldsymbol{M}, \tag{2.5}$$

$$\nabla \times \boldsymbol{H} = j\omega\epsilon \boldsymbol{E} + \boldsymbol{J}, \tag{2.6}$$

where the electric permittivity ϵ and the magnetic permeability μ measures respectively the electric polarizability and the magnetization of the dielectric material. In general cases, both permittivity and permeability are tensorial parameters, but in case of linear, homogeneous and isotropic materials, they reduce to scalar values that can be expressed as

$$\epsilon = \epsilon_r \epsilon_0, \tag{2.7}$$

$$\mu = \mu_r \mu_0 \tag{2.8}$$

where ϵ_r and μ_r are the parameters relative to the dielectric material, while ϵ_0 and μ_0 are the vacuum permittivity and the vacuum permeability, respectively.

2.2 Electromagnetic Fields in Free Space

In this section we manipulate Maxwell's equations in order to obtain the electromagnetic fields generated in free space from electric and magnetic sources.

2.2.1 Vector and scalar potentials

In the following, Maxwell's are rewritten in terms of vector and scalar potentials. This manipulation is necessary to define the formulations of the electromagnetic integral equations that will be solved with the boundary element method (BEM). In the following, the subscripts $_e$ and $_m$ means that the relative quantity is generated form an electric or a magnetic source, respectively.

Electric sources

For fields generated by electric sources, Maxwell's equations read

$$\nabla \times \boldsymbol{E}_e = -j\omega\mu \boldsymbol{H}_e \tag{2.9}$$

$$\nabla \times \boldsymbol{H}_e = j\omega\epsilon \boldsymbol{E}_e + \boldsymbol{J}, \tag{2.10}$$

$$\nabla \cdot \boldsymbol{D}_e = \boldsymbol{\rho}_e, \tag{2.11}$$

$$\nabla \cdot \boldsymbol{B}_e = \boldsymbol{0}. \tag{2.12}$$

Considering eq. (2.12), we now introduce the magnetic vector potential $\boldsymbol{A}$ defining its curl

$$\nabla \times \boldsymbol{A} = \mu \boldsymbol{H}_e, \tag{2.13}$$

such that $\nabla \cdot \boldsymbol{B}_e = \nabla \cdot (\nabla \times \boldsymbol{A}) = \boldsymbol{0}$. Replacing eq. (2.13) in eq. (2.9) we obtain

$$\nabla \times (\boldsymbol{E}_e + j\omega \boldsymbol{A}) = \boldsymbol{0}, \tag{2.14}$$

and now we introduce the electric scalar potential $\varPhi_e$ defining its gradient

$$-\nabla \varPhi_e = \boldsymbol{E}_e + j\omega \boldsymbol{A}, \tag{2.15}$$

such that $\nabla \times (\boldsymbol{E}_e + j\omega \boldsymbol{A}) = -\nabla \times \nabla \varPhi_e = \boldsymbol{0}$.

Magnetic sources

For the case of fields generated by magnetic sources we have that

$$\begin{align} \nabla \times \boldsymbol{E}_m &= -j\omega\mu \boldsymbol{H}_m - \boldsymbol{M}, \tag{2.16}\\ \nabla \times \boldsymbol{H}_m &= j\omega\epsilon \boldsymbol{E}_m, \tag{2.17}\\ \nabla \cdot \boldsymbol{D}_m &= \boldsymbol{0}, \tag{2.18}\\ \nabla \cdot \boldsymbol{B}_m &= \boldsymbol{\rho}_m, \tag{2.19} \end{align}$$

and considering the symmetries of Maxwell's equations, we introduce analogously the electric vector potential $\boldsymbol{F}$ and the magnetic scalar potential $\varPhi_m$ such that

$$\begin{align} \nabla \times \boldsymbol{F} &= -\epsilon \boldsymbol{E}_m, \tag{2.20}\\ -\nabla \varPhi_m &= \boldsymbol{H}_m + j\omega \boldsymbol{F}. \tag{2.21} \end{align}$$

2.2.2 Lorenz gauge and Helmholtz equations

So far, we defined the curl of $\boldsymbol{A}$ and the curl of $\boldsymbol{F}$, but we have not defined yet their divergence. A convenient option to further simplify the following equations is to respect the Lorenz gauge conditions

$$\begin{align} \nabla \cdot \boldsymbol{A} &= -j\omega\epsilon\mu \varPhi_e, \tag{2.22}\\ \nabla \cdot \boldsymbol{F} &= -j\omega\epsilon\mu \varPhi_m. \tag{2.23} \end{align}$$

The convenience of this choice is evident when we substitute respectively eq. (2.13) and eq. (2.15) in eq. (2.10), and eq. (2.20) and eq. (2.21) in eq. (2.16) obtaining

$$\begin{align} \nabla \times \left(\frac{1}{\mu} \nabla \times \boldsymbol{A}\right) &= -j\omega\epsilon \nabla \varPhi_e + \omega^2 \epsilon \boldsymbol{A} + \boldsymbol{J}, \tag{2.24}\\ \nabla \times \left(-\frac{1}{\epsilon} \nabla \times \boldsymbol{F}\right) &= j\omega\mu \nabla \varPhi_m - \omega^2 \mu \boldsymbol{F} - \boldsymbol{M}, \tag{2.25} \end{align}$$

and finally applying the vector identity $\nabla \times \nabla \times \boldsymbol{V} = \nabla(\nabla \cdot \boldsymbol{V}) - \nabla^2 \boldsymbol{V}$, obtaining

$$\nabla(\nabla \cdot \boldsymbol{A}) - \nabla^2 \boldsymbol{A} = -j\omega\epsilon\mu\nabla \mathit{\Phi}_e + \omega^2 \epsilon\mu\boldsymbol{A} + \mu\boldsymbol{J}, \tag{2.26}$$

$$\nabla(\nabla \cdot \boldsymbol{F}) - \nabla^2 \boldsymbol{F} = -j\omega\epsilon\mu\nabla \mathit{\Phi}_m + \omega^2 \epsilon\mu\boldsymbol{F} + \epsilon\boldsymbol{M}. \tag{2.27}$$

Now, thanks to the Lorenz gauge conditions, and defining the wavenumber $k = \omega\sqrt{\epsilon\mu}$ and applying the vector identity $\nabla \times \nabla \times \boldsymbol{V} = \nabla(\nabla \cdot \boldsymbol{V}) - \nabla^2 \boldsymbol{V}$, where ∇^2 is the vector Laplacian operator, we can simplify the previous equations and get

$$\nabla^2 \boldsymbol{A} + k^2 \boldsymbol{A} = -\mu\boldsymbol{J}, \tag{2.28}$$

$$\nabla^2 \boldsymbol{F} + k^2 \boldsymbol{F} = -\epsilon\boldsymbol{M}. \tag{2.29}$$

Equation (2.28) and eq. (2.29) are inhomogeneous Helmholtz equations that can be solved respectively for $\boldsymbol{A}$ and $\boldsymbol{F}$ leveraging the Green's function method.

2.2.3 Green's Function

Defined the dimensionality of the problem and the boundary conditions, a Green's function, or fundamental solution, of a differential equation is the impulse response of the involved differential operator. This section treats the 2D and the 3D cases of the scalar inhomogeneous Helmholtz equations, and further uses these to retrieve the solution of eq. (2.28) and eq. (2.28) presented in the previous section. In this work we will always consider Sommerfeld radiation condition as boundary condition, and hence impose that at infinity the energy radiated by the solution must disperse. In terms of equations, for a solution $u(x)$, in a domain $\mathbb{R}^n$, and for a constant $k > 0$, this translates in

$$\lim_{\|x\| \to \infty} \|x\|^{\frac{n-1}{2}} \left(\frac{\partial}{\partial \|x\|} - jk \right) u(x) = 0. \tag{2.30}$$

Under these conditions, we can define the free-space Green's function $G(\boldsymbol{r}, \boldsymbol{r}')$ as the solution of the scalar inhomogeneous Helmholtz equation

$$\nabla^2 G(\boldsymbol{r}, \boldsymbol{r}') + k^2 G(\boldsymbol{r}, \boldsymbol{r}') = -\delta(\boldsymbol{r}, \boldsymbol{r}'). \tag{2.31}$$

Since we work in the frequency domain, and the definition of the Green's function depends of the sign convention used to obtain the Fourier transform of a function in the time domain, we specify that in our convention the Fourier transform of $f(t)$ is given by

$$F(\omega) = \int_{-\infty}^{\infty} f(t) e^{-j\omega t} dt. \tag{2.32}$$

Three-dimensional case

In 3D instead, the Green's function for $k > 0$ reads like

$$G(\boldsymbol{r}, \boldsymbol{r}') = \frac{\mathrm{e}^{-\mathrm{jk}\|\boldsymbol{r}-\boldsymbol{r}'\|}}{4\pi\|\boldsymbol{r}-\boldsymbol{r}'\|}. \tag{2.33}$$

In the static limit, when $k \to 0$, we simply have

$$G_0(\boldsymbol{r}, \boldsymbol{r}') = \frac{1}{4\pi\|\boldsymbol{r}-\boldsymbol{r}'\|}. \tag{2.34}$$

Two-dimensional case

In 2D, the Green's function for $k > 0$ reads like

$$G(\boldsymbol{r}, \boldsymbol{r}') = -\frac{j}{4} H_0^{(2)}\left(k\|\boldsymbol{r}-\boldsymbol{r}'\|\right), \tag{2.35}$$

where $H_0^{(2)}$ is the Hankel function of the second kind with order zero.

In the static limit, when $k \to 0$, we have instead

$$G_0(\boldsymbol{r}, \boldsymbol{r}') = -\frac{1}{2\pi} \log\left(\|\boldsymbol{r}-\boldsymbol{r}'\|\right). \tag{2.36}$$

2.2.4 Fields generated by arbitrary sources

Three-dimensional case

We can use the Green's function approach and solve eq. (2.28) and eq. (2.29) by convolving eq. (2.31), in the whole domain, respectively with $\mu\boldsymbol{J}$ and $\epsilon\boldsymbol{M}$, obtaining

$$\mu \iiint_V G(\boldsymbol{r}, \boldsymbol{r}') \left[\nabla^2 + k^2\right] \boldsymbol{J}(\boldsymbol{r}')\mathrm{d}\boldsymbol{r}' = -\mu\boldsymbol{J}, \tag{2.37}$$

$$\epsilon \iiint_V G(\boldsymbol{r}, \boldsymbol{r}') \left[\nabla^2 + k^2\right] \boldsymbol{M}(\boldsymbol{r}')\mathrm{d}\boldsymbol{r}' = -\epsilon\boldsymbol{M}. \tag{2.38}$$

Thanks to this passage we can now retrieve the expression for the magnetic and electric vector potential that solves the two Helmholtz equations, which read

$$\boldsymbol{A} = \mu \iiint_V G(\boldsymbol{r}, \boldsymbol{r}')\boldsymbol{J}(\boldsymbol{r}')\mathrm{d}\boldsymbol{r}', \tag{2.39}$$

$$\boldsymbol{F} = \epsilon \iiint_V G(\boldsymbol{r}, \boldsymbol{r}')\boldsymbol{M}(\boldsymbol{r}')\mathrm{d}\boldsymbol{r}'. \tag{2.40}$$

At this point we can use the superimposition principle to compute the electric and the magnetic field in presence of arbitrary electric and magnetic sources. To compute the electric field we can sum the contribution radiated by the magnetic sources $\boldsymbol{E}_m$ from eq. (2.20) to the contribution radiated by the magnetic sources $\boldsymbol{E}_e$ from eq. (2.15), and insert it in eq. (2.22), obtaining

$$\begin{aligned}\boldsymbol{E} &= -j\omega\boldsymbol{A} + \frac{1}{j\omega\epsilon\mu}\nabla\left(\nabla\cdot\boldsymbol{A}\right) - \frac{1}{\epsilon}\nabla\times\boldsymbol{F} && (2.41)\\ &= -j\omega\left[1 + \frac{1}{k^2}\nabla\nabla\cdot\right]\boldsymbol{A} - \frac{1}{\epsilon}\nabla\times\boldsymbol{F} && (2.42)\\ &= -j\omega\mu\iiint_V G(\boldsymbol{r},\boldsymbol{r}')\left[1 + \frac{1}{k^2}\nabla'\nabla'\cdot\right]\boldsymbol{J}(\boldsymbol{r}')\mathrm{d}\boldsymbol{r}' - \iiint_V G(\boldsymbol{r},\boldsymbol{r}')\nabla'\times\boldsymbol{M}(\boldsymbol{r}')\mathrm{d}\boldsymbol{r}'. && (2.43)\end{aligned}$$

The same is done with the magnetic field, we sum the contribution radiated by the electric sources $\boldsymbol{H}_e$ from eq. (2.13) to the contribution radiated by the magnetic sources $\boldsymbol{H}_m$ from eq. (2.21), and substitute in eq. (2.23), yielding

$$\begin{aligned}\boldsymbol{H} &= -j\omega\boldsymbol{F} + \frac{1}{j\omega\epsilon\mu}\nabla\left(\nabla\cdot\boldsymbol{F}\right) + \frac{1}{\mu}\nabla\times\boldsymbol{A} && (2.44)\\ &= -j\omega\left[1 + \frac{1}{k^2}\nabla\nabla\cdot\right]\boldsymbol{F} + \frac{1}{\mu}\nabla\times\boldsymbol{A} && (2.45)\\ &= -j\omega\epsilon\iiint_V G(\boldsymbol{r},\boldsymbol{r}')\left[1 + \frac{1}{k^2}\nabla'\nabla'\cdot\right]\boldsymbol{M}(\boldsymbol{r}')\mathrm{d}\boldsymbol{r}' + \iiint_V G(\boldsymbol{r},\boldsymbol{r}')\nabla'\times\boldsymbol{J}(\boldsymbol{r}')\mathrm{d}\boldsymbol{r}'. && (2.46)\end{aligned}$$

Two-dimensional case

In the two-dimensional problems, described at the beginning of this chapter, the electromagnetic fields can be computed solving the scalar 2D inhomogeneous Helmholtz equation

$$\nabla^2\varphi(\boldsymbol{r}) + k^2\varphi(\boldsymbol{r}) = f(\boldsymbol{r}), \tag{2.47}$$

where $f(\boldsymbol{r})$ represent the source generating the filed [52]. Further developments of the equation are given for the case of an arbitrary shaped object immersed in free space.

2.3 Electromagnetic Integral Equations

Now that we defined a set of equations suitable to compute electromagnetic fields in free-space, we can move to the solution of scattering problems in the presence of an arbitrary obstacle (the scatterer) with known electromagnetic properties. First, we define the setting of a general scattering problem. There are multiple options for the source of the electromagnetic fields (e.g. an impinging plane wave, a dipole, etc.), but in all the cases we call incident field the field generated in free space by the source (in the absence of the scatterer), that is distinguished from the scattered field, that can be seen as the total field in presence of the scatterer to witch the incident field it is subtracted. In the following, the incident, the scattered, and the total fields are denoted with the respective superscripts ^{inc}, ^{s}, ^{tot}, respectively. In particular, because of superposition, we have $(\boldsymbol{E}, \boldsymbol{H}) = \left(\boldsymbol{E}^{tot}, \boldsymbol{H}^{tot}\right) = \left(\boldsymbol{E}^{inc}, \boldsymbol{H}^{inc}\right) + (\boldsymbol{E}^{s}, \boldsymbol{H}^{s})$. In this work, the scattering problems are solved leveraging formulations based on integral equations.

2.3.1 Boundary Conditions

The properties of the scatterers determine the boundary conditions at the interface between two discontinuous regions, which then determine the integral equation formulation required to solve the problems. In the following we present the scenarios that are relevant for this work, both for the 3D and 2D cases.

General Discontinuity

In both 2D and 3D, we consider an object described by the region Ω_0, with boundary Γ_0 defined by the vector normal to its surface $\hat{\boldsymbol{n}}$, and immersed in the infinite region Ω_∞ as depicted in fig. 2.1 and fig. 2.2. Considering the electromagnetic field inside the region Ω_0 is defined as $(\boldsymbol{E}_0, \boldsymbol{H}_0, \boldsymbol{D}_0, \boldsymbol{B}_0)$, while in region Ω_∞ we have $(\boldsymbol{E}_\infty, \boldsymbol{H}_\infty, \boldsymbol{D}_\infty, \boldsymbol{B}_\infty)$, for their limit approaching the two sides of the boundary Γ, they must satisfy the boundary conditions

$$\hat{\boldsymbol{n}} \times (\boldsymbol{E}_\infty - \boldsymbol{E}_0) = -\boldsymbol{M}_\Gamma, \tag{2.48}$$

$$\hat{\boldsymbol{n}} \times (\boldsymbol{H}_\infty - \boldsymbol{H}_0) = \boldsymbol{J}_\Gamma, \tag{2.49}$$

$$\hat{\boldsymbol{n}} \cdot (\boldsymbol{D}_\infty - \boldsymbol{D}_0) = \boldsymbol{\rho}_{e,\Gamma}, \tag{2.50}$$

$$\hat{\boldsymbol{n}} \cdot (\boldsymbol{B}_\infty - \boldsymbol{B}_0) = \boldsymbol{\rho}_{m,\Gamma}, \tag{2.51}$$

at the boundary that determines the discontinuity. This writing is not purely formal since the limits should be explicitly defined, but it helps to concisely express the concept and the notation further needed.

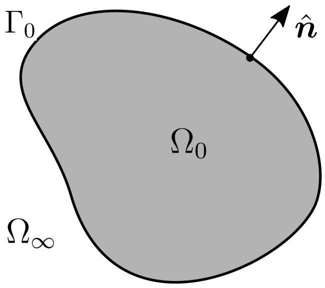

Figure 2.1: *Regions defined by a 2D scatterer.*

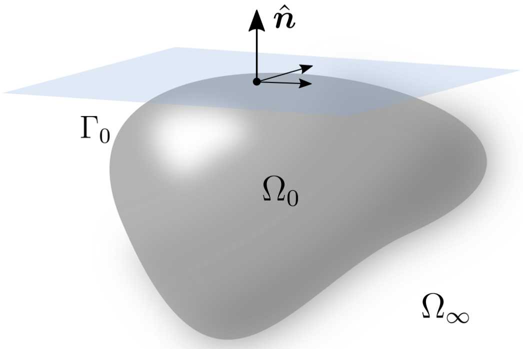

Figure 2.2: *Regions defined by a 3D scatterer.*

Perfect Electric Conductors

For perfect electric conductor (PEC), the boundary conditions become

$$\hat{\boldsymbol{n}} \times (\boldsymbol{E}_\infty - \boldsymbol{E}_0) = \boldsymbol{0}, \tag{2.52}$$

$$\hat{\boldsymbol{n}} \times (\boldsymbol{H}_\infty - \boldsymbol{H}_0) = \boldsymbol{J}_\Gamma, \tag{2.53}$$

$$\hat{\boldsymbol{n}} \cdot (\boldsymbol{D}_\infty - \boldsymbol{D}_0) = \boldsymbol{\rho}_{e,\Gamma}, \tag{2.54}$$

$$\hat{\boldsymbol{n}} \cdot (\boldsymbol{B}_\infty - \boldsymbol{B}_0) = \boldsymbol{0}. \tag{2.55}$$

2.3.2 Love's Equivalence Principle

Three-dimensional case

Equation (2.43) and eq. (2.46) are valid only to compute fields in an infinitely large and homogeneous media. We can leverage the surface equivalence principle to extend their application to the computation of electromagnetic fields in presence of a scatterer. Consider an original problem, depicted in fig. 2.3 (a), in which the scatterer Ω_0 is characterized by (ϵ_0, μ_0), and the media $\Omega_\infty = \mathbb{R}^n \backslash \Omega_0$ is characterized by $(\epsilon_\infty, \mu_\infty)$.

The equivalence principle states that we can replace the fields $(\boldsymbol{E}_0, \boldsymbol{H}_0)$, and eventual current densities $(\boldsymbol{J}_0, \boldsymbol{M}_0)$, inside Ω_0 with alternative fields $(\boldsymbol{E}'_0, \boldsymbol{H}'_0)$ and surface current densities $(\boldsymbol{J}_\Gamma, \boldsymbol{M}_\Gamma)$, while keeping the same total field $(\boldsymbol{E}_\infty, \boldsymbol{H}_\infty)$ in the outside region. The only constraints that need to be respected are that $(\boldsymbol{E}'_0, \boldsymbol{H}'_0)$ satisfy Maxwell's equations, and the boundary conditions

$$\hat{\boldsymbol{n}} \times (\boldsymbol{E}_\infty - \boldsymbol{E}'_0) = -\boldsymbol{M}_\Gamma, \tag{2.56}$$

$$\hat{\boldsymbol{n}} \times (\boldsymbol{H}_\infty - \boldsymbol{H}'_0) = \boldsymbol{J}_\Gamma. \tag{2.57}$$

Now, if we set $(\boldsymbol{E}'_0, \boldsymbol{H}'_0) = (\boldsymbol{0}, \boldsymbol{0})$, the material parameters of the scatterer, in region Ω_0 become irrelevant, so we can replace them with the ones of Ω_∞ and study the

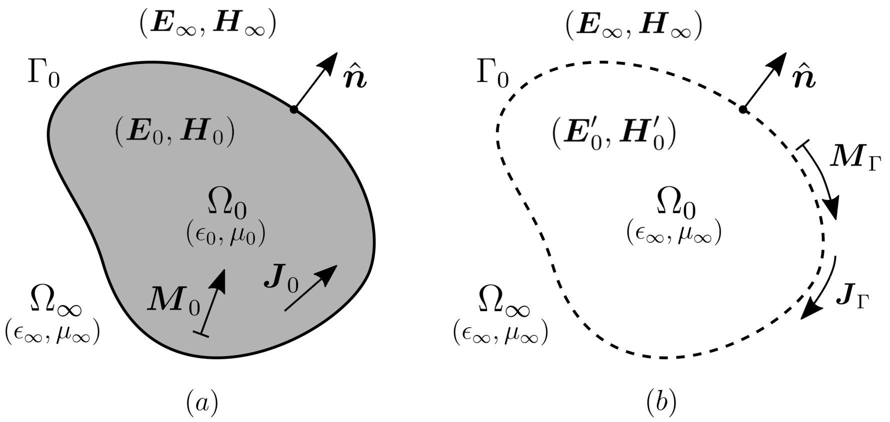

Figure 2.3: *Equivalence principle: (a) original problem; (b) equivalent problem.*

Love's equivalent problem shown in fig. 2.3 (b). This problem needs to satisfy the following boundary conditions

$$\hat{\boldsymbol{n}} \times \boldsymbol{E}_\infty = -\boldsymbol{M}_\Gamma, \tag{2.58}$$

$$\hat{\boldsymbol{n}} \times \boldsymbol{H}_\infty = \boldsymbol{J}_\Gamma, \tag{2.59}$$

and now we can use eq. (2.43) and eq. (2.46) to compute the fields $(\boldsymbol{E}_\infty, \boldsymbol{H}_\infty)$.

Two-dimensional case

The 2D case, as already mentioned, is actually a 3D problem where we assume that the scatterer has no variation along the z-axis. In this case, we can consider only the plane perpendicular to the z-axis. In addition, the problem can be decomposed into Transverse Magnetic (TM) and Transverse Electric (TE) polarizations of the electromagnetic field, and each single problem reduces to the computation of a scalar field along the one-dimensional (1D) manifold.

We use again the Green's function approach and we multiply eq. (2.47) by $G(\boldsymbol{r}, \boldsymbol{r}')$ and eq. (2.31) by $\varphi(\boldsymbol{r})$. Then, integrating their difference in the 2D region, we obtain the equation

$$\iint_{\Omega_{\text{inf}}} \left[G(\boldsymbol{r}, \boldsymbol{r}')\nabla^2\varphi(\boldsymbol{r}) - \varphi(\boldsymbol{r})\nabla^2 G(\boldsymbol{r}, \boldsymbol{r}')\right] \mathrm{d}\boldsymbol{r}' = \iint_{\Omega_s} G(\boldsymbol{r}, \boldsymbol{r}') f(\boldsymbol{r}) \mathrm{d}\boldsymbol{r}' + \iint_{\Omega_{\text{inf}}} \varphi(\boldsymbol{r})\delta(\boldsymbol{r} - \boldsymbol{r}')\mathrm{d}\boldsymbol{r}', \tag{2.60}$$

where Ω_s is the region where $f(\boldsymbol{r})$ is not zero. This equation, with few more manipulations omitted here for the sake of brevity, can lead to

$$\varphi^{inc}(\boldsymbol{r}) + \fint_{\Gamma_0} \left[\varphi(\boldsymbol{r}') \frac{\partial G(\boldsymbol{r}, \boldsymbol{r}')}{\partial \hat{\boldsymbol{n}}} - G(\boldsymbol{r}, \boldsymbol{r}') \frac{\partial \varphi(\boldsymbol{r}')}{\partial \hat{\boldsymbol{n}}}\right] \mathrm{d}\Gamma' = \begin{cases} \varphi(\boldsymbol{r}) & \boldsymbol{r} \in \Omega_{\text{inf}} \\ 0 & \boldsymbol{r} \in \Omega_0, \end{cases} \tag{2.61}$$

where $⨍$ denote the Cauchy principal value integral and $\frac{\partial}{\partial \hat{\boldsymbol{n}}}$ the normal derivative. This equation represents the Huygens' principle for scalar fields, that states that the field can be evaluated everywhere in that domain if the field and its normal derivative are known on the boundary of it. Finally, it can derive the equation that is at the base of 2D electromagnetic integral formulations

$$\varphi^{inc}(\boldsymbol{r}) + ⨍_{\Gamma_0} \left[\varphi(\boldsymbol{r}') \frac{\partial G(\boldsymbol{r}, \boldsymbol{r}')}{\partial \hat{\boldsymbol{n}}} - G(\boldsymbol{r}, \boldsymbol{r}') \frac{\partial \varphi(\boldsymbol{r}')}{\partial \hat{\boldsymbol{n}}} \right] \mathrm{d}\Gamma' = \frac{1}{2}\varphi(\boldsymbol{r}) \qquad \boldsymbol{r} \in \Gamma_0. \tag{2.62}$$

2.3.3 Main Electromagnetic Integral Equations Formulations

Now we have all the ingredients to define a formulation to solve electromagnetic scattering problems based on integral equations. Since the formulation depends on the application scenario, and since in this work we deal with different formulations, here we introduce only the main 2D and 3D formulations for PEC scatterers, mainly to define the notation. The complete formulations used for the research work are shown in their respective chapters, to avoid the reader the need to go back in this section for the definitions. In chapter 5 some electromagnetic solvers involving multi layer dielectric scatterers are employed, however, since they are practically used as a black box, and they are not the focus of this work, we do not give further details on their formulations, but only cite the relevant references for their implementations.

3D PEC dynamic formulations

Since we are considering a PEC object, we are only interested on the solution of the exterior problem. For this reason we recall eq. (2.58) eq. (2.59) and we use the superposition to express them as

$$\boldsymbol{M}_\Gamma = -\hat{\boldsymbol{n}} \times \boldsymbol{E}_\infty = -\hat{\boldsymbol{n}} \times (\boldsymbol{E}^{inc}_\infty + \boldsymbol{E}^{s}_\infty), \tag{2.63}$$
$$\boldsymbol{J}_\Gamma = \hat{\boldsymbol{n}} \times \boldsymbol{H}_\infty = \hat{\boldsymbol{n}} \times (\boldsymbol{H}^{inc}_\infty + \boldsymbol{H}^{s}_\infty). \tag{2.64}$$

To simplify the notation, in the following we omit the subscript $_\infty$ and $_\Gamma$. We now introduce the definition of some boundary integral operators (BIO), in order to simplify the above expressions

$$\boldsymbol{\mathcal{T}}_{s,k}\boldsymbol{X} = \hat{\boldsymbol{n}} \times jk \int_{\Gamma_0} G(\boldsymbol{r}, \boldsymbol{r}') \boldsymbol{X}(\boldsymbol{r}') \mathrm{d}\Gamma', \tag{2.65}$$
$$\boldsymbol{\mathcal{T}}_{h,k}\boldsymbol{X} = -\hat{\boldsymbol{n}} \times \frac{1}{jk} \nabla \int_{\Gamma_0} G(\boldsymbol{r}, \boldsymbol{r}') \nabla \cdot \boldsymbol{X}(\boldsymbol{r}') \mathrm{d}\Gamma', \tag{2.66}$$
$$\boldsymbol{\mathcal{T}}_{k}\boldsymbol{X} = \boldsymbol{\mathcal{T}}_{s,k}\boldsymbol{X} + \boldsymbol{\mathcal{T}}_{h,k}\boldsymbol{X}, \tag{2.67}$$
$$\boldsymbol{\mathcal{K}}_{k}\boldsymbol{X} = \hat{\boldsymbol{n}} \times \int_{\Gamma_0} G(\boldsymbol{r}, \boldsymbol{r}') \nabla' \times \boldsymbol{X}(\boldsymbol{r}') \mathrm{d}\Gamma', \tag{2.68}$$

Now, using Love's equivalence principle, combining this expressions with eq. (2.43) and eq. (2.46) evaluated on the boundary of the scatterer and using the new definition of the operators we get

$$\boldsymbol{M} - \frac{\omega\mu}{k}\boldsymbol{\mathcal{T}}_k\boldsymbol{J} - \boldsymbol{\mathcal{K}}_k\boldsymbol{M} = -\hat{\boldsymbol{n}} \times \boldsymbol{E}^{inc}, \qquad \boldsymbol{r} \in \Gamma_0, \tag{2.69}$$

$$\boldsymbol{J} + \frac{\omega\epsilon}{k}\boldsymbol{\mathcal{T}}_k\boldsymbol{M} - \boldsymbol{\mathcal{K}}_k\boldsymbol{J} = \hat{\boldsymbol{n}} \times \boldsymbol{H}^{inc}, \qquad \boldsymbol{r} \in \Gamma_0. \tag{2.70}$$

At this point, since we are in PEC, we can use the fact that the surface magnetic current is null, as stated in eq. (2.52), leading to

$$\boldsymbol{\mathcal{T}}_k\boldsymbol{J} = \frac{1}{\eta}\hat{\boldsymbol{n}} \times \boldsymbol{E}^{inc}, \qquad \boldsymbol{r} \in \Gamma_0, \tag{2.71}$$

$$\boldsymbol{J} - \boldsymbol{\mathcal{K}}_k\boldsymbol{J} = \hat{\boldsymbol{n}} \times \boldsymbol{H}^{inc}, \qquad \boldsymbol{r} \in \Gamma_0, \tag{2.72}$$

where η is the characteristic impedance of vacuum, and the fact $\omega\mu = \eta k$ was used. However, eq. (2.72) cannot be calculated on Γ_0, because $\boldsymbol{\mathcal{K}}_k$ is singular. In case of closed, smooth and not infinitely thin surfaces, a proper treatment of the singularity [52] yields

$$\boldsymbol{\mathcal{T}}_k\boldsymbol{J} = \boldsymbol{\mathcal{T}}_{s,k}\boldsymbol{J} + \boldsymbol{\mathcal{T}}_{h,k}\boldsymbol{J} = \frac{1}{\eta}\hat{\boldsymbol{n}} \times \boldsymbol{E}^{inc}, \qquad \boldsymbol{r} \in \Gamma_0, \tag{2.73}$$

$$\left(\frac{\boldsymbol{\mathcal{I}}}{2} - \boldsymbol{\mathcal{K}}_k\right)\boldsymbol{J} = \hat{\boldsymbol{n}} \times \boldsymbol{H}^{inc}, \qquad \boldsymbol{r} \in \Gamma_0. \tag{2.74}$$

Equation (2.73) and eq. (2.74) are respectively the 3D-PEC electric field integral equation (EFIE) and the 3D-PEC magnetic field integral equation (MFIE).

2D PEC dynamic formulations

We consider the scenario where we have a 2D structure where the scatterer is a PEC and $k > 0$. For 2D problems, to know all the components of the electric and magnetic fields, we need to solve the problem for both the TM and TE polarizations [48]. Figure 2.4 helps understanding the orientations of the structure along the z-axis $\hat{\boldsymbol{z}}$, the normal vector $\hat{\boldsymbol{n}}$ and the tangent vector $\hat{\boldsymbol{t}}$, relevant in the following developments. Note that since the orientation of the tangent vector is not unique, particular attention should be given to the used convention.

TM-EFIE For the TM polarization we know that the electric field satisfies the Helmholtz equation and the boundary conditions

$$\nabla^2 E_z + k^2 E_z = jk\eta J_z^{inc} \qquad \boldsymbol{r} \in \Omega_\infty, \tag{2.75}$$

$$E_z = 0 \qquad \boldsymbol{r} \in \Gamma_0, \tag{2.76}$$

$$\frac{\partial E_z}{\partial \hat{\boldsymbol{n}}} = jk\eta J_z^s = jk\eta H_t \qquad \boldsymbol{r} \in \Gamma_0, \tag{2.77}$$

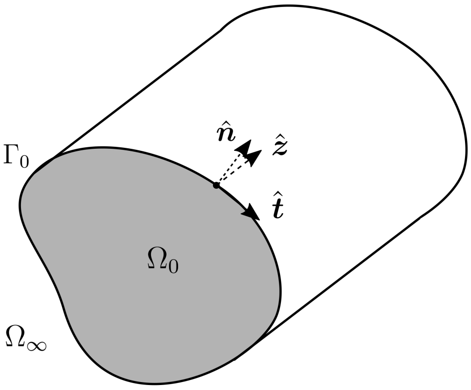

Figure 2.4: *Orientation of the vectors* $\hat{\boldsymbol{z}}$, $\hat{\boldsymbol{n}}$ *and* $\hat{\boldsymbol{t}}$ *in 2D structures.*

where $\eta = \sqrt{\frac{\mu_0}{\epsilon_0}}$ is the impedance of free-space, J_z^{inc} the source generating the incident field and J_z^s the surface current density induced by the incident field. Substituting these quantities and boundary conditions in eq. (2.62) we get

$$jk \int_{\Gamma_0} G(\boldsymbol{r}, \boldsymbol{r}') J_z^s(\boldsymbol{r}') \mathrm{d}\Gamma' = \frac{1}{\eta} E_z^{inc}(\boldsymbol{r}) \qquad \boldsymbol{r} \in \Gamma_0. \tag{2.78}$$

We refer to this equation as the Electric Field Integral Equation (EFIE) with TM polarization (TM-EFIE). We further simplify the notation defining the Single Layer Potential operator in 2D (SLP-2D) as

$$\mathcal{S} J_z^s(\boldsymbol{r}) = \int_{\Gamma_0} G(\boldsymbol{r}, \boldsymbol{r}') J_z^s(\boldsymbol{r}') \mathrm{d}\Gamma' \tag{2.79}$$

getting

$$jk \mathcal{S} J_z^s(\boldsymbol{r}) = \frac{1}{\eta} E_z^{inc}(\boldsymbol{r}) \qquad \boldsymbol{r} \in \Gamma_0. \tag{2.80}$$

A similar procedure can be applied to retrieve the other formulations starting form eq. (2.62) and proper boundary conditions. For the following formulations we report only the definitions of the operators and the final equation.

TM-MFIE For the H field with TM polarization we get

$$\left[\frac{1}{2} \mathcal{I} + ⨍_{\Gamma_0} \mathrm{d}\Gamma' \frac{\partial G(\boldsymbol{r}, \boldsymbol{r}')}{\partial \hat{\boldsymbol{n}}} \right] J_z^s(\boldsymbol{r}') = H_t^{inc}(\boldsymbol{r}) \qquad \boldsymbol{r} \in \Gamma_0. \tag{2.81}$$

We refer to this equation as the Magnetic Field Integral Equation (MFIE) with TM polarization (TM-MFIE). We further simplify the notation defining the adjoint double layer potential operator in 2D (ADLP-2D) as

$$\mathcal{D}^* J_z^s(\boldsymbol{r}) = ⨍_{\Gamma_0} \frac{\partial G(\boldsymbol{r}, \boldsymbol{r}')}{\partial \hat{\boldsymbol{n}}} J_z^s(\boldsymbol{r}') \mathrm{d}\Gamma', \tag{2.82}$$

getting

$$\left(\frac{1}{2}\mathcal{I} + \mathcal{D}^*\right) J_z^s(\boldsymbol{r}') = H_t^{inc}(\boldsymbol{r}) \qquad \boldsymbol{r} \in \Gamma_0. \tag{2.83}$$

TE-EFIE For the E field with TE polarization we get

$$-\frac{1}{jk}\int_{\Gamma_0} \frac{\partial}{\partial \hat{\boldsymbol{n}}} \frac{\partial G(\boldsymbol{r}, \boldsymbol{r}')}{\partial \hat{\boldsymbol{n}}'} J_t^s(\boldsymbol{r}')\mathrm{d}\Gamma' = \frac{1}{\eta} E_t^{inc}(\boldsymbol{r}) \qquad \boldsymbol{r} \in \Gamma_0. \tag{2.84}$$

We refer to this equation as the EFIE with TM polarization (TE-EFIE). We further simplify the notation defining the hypersingular operator in 2D (HS-2D) as

$$\mathcal{N} J_t^s(\boldsymbol{r}) = -\frac{\partial}{\partial \hat{\boldsymbol{n}}} \int_{\Gamma_0} \frac{\partial G(\boldsymbol{r}, \boldsymbol{r}')}{\partial \hat{\boldsymbol{n}}'} J_t^s(\boldsymbol{r}')\mathrm{d}\Gamma' \tag{2.85}$$

$$= -\int_{\Gamma_0} \left[k^2 + \frac{\partial^2}{\partial \hat{\boldsymbol{r}}}\right] G(\boldsymbol{r}, \boldsymbol{r}') J_t^s(\boldsymbol{r}')\mathrm{d}\Gamma', \tag{2.86}$$

getting

$$\frac{1}{jk}\mathcal{N} J_t^s(\boldsymbol{r}) = \frac{1}{\eta} E_t^{inc}(\boldsymbol{r}) \qquad \boldsymbol{r} \in \Gamma_0. \tag{2.87}$$

TE-MFIE For the H field with TE polarization we get

$$-\left[\frac{1}{2}\mathcal{I} - \fint_{\Gamma_0} \frac{\partial G(\boldsymbol{r}, \boldsymbol{r}')}{\partial \hat{\boldsymbol{n}}}\right] J_t^s(\boldsymbol{r}') = H_z^{inc}(\boldsymbol{r}) \qquad \boldsymbol{r} \in \Gamma_0. \tag{2.88}$$

We refer to this equation as the MFIE with TM polarization (TE-MFIE). We further simplify the notation defining the double layer potential operator in 2D (DLP-2D) as

$$\mathcal{D} J_t^s(\boldsymbol{r}) = \fint_{\Gamma_0} \frac{\partial G(\boldsymbol{r}, \boldsymbol{r}')}{\partial \hat{\boldsymbol{n}}'} J_t^s(\boldsymbol{r}')\mathrm{d}\Gamma', \tag{2.89}$$

getting

$$-\left(\frac{1}{2}\mathcal{I} - \mathcal{D}\right) J_t^s(\boldsymbol{r}') = H_t^{inc}(\boldsymbol{r}) \qquad \boldsymbol{r} \in \Gamma_0. \tag{2.90}$$

Note that the operator $\mathcal{D}$ is simply the adjoint version of the operator $\mathcal{D}^*$.

2.4 Boundary Element Method

The integral equations defined in the previous section, along with most of differential and integral equations that arise in physics, can be solved analytically only for few special geometries. For this reason numerical methods are generally necessary to solve such equations. Boundary integral equations can be solved via BEM, also known as Method of Moments (MoM), or in some cases Galerkin Method.

2.4.1 Geometry Discretization

As for most of numerical methods, the problem is discretized dividing the geometry of the studied scenario in small sub elements. In scattering problems solved with BEM, it is sufficient to discretize the surface of the scatterer, in contrast to other solvers such as the Finite Element Method (FEM) or solvers based on Volume Integral Equations (VIE) where a volumetric discretization is necessary.

Three-dimensional case

In 3D the geometry is discretized N_t with admissible triangular elements, as depicted in fig. 2.5. Each triangle is parameterized by two-dimensional local coordinates that are used to compute the integrals involved in the formulation. The mesh is also consisting of N_v vertices, connected by N_e edges, that in triplets form the triangles and being oriented define the outward-pointing normal vector. In addition, we also define the global mesh size h as the average edge length, that will be a relevant parameter in the following section.

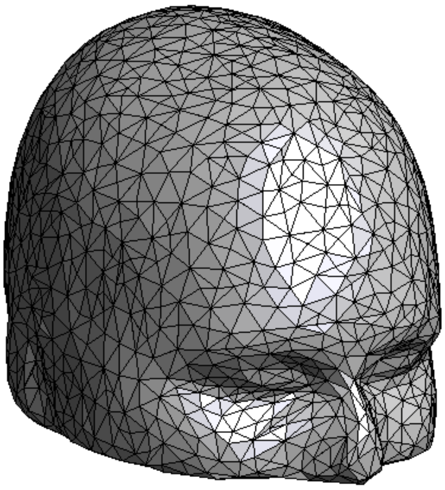

Figure 2.5: *Human head discretized with triangles.*

Two-dimensional case

For the 2D case, the boundary of the scatterer is discretized with N_s segments defined by the connection of N_v vertices. For closed structures we have $N_s = N_v$. An example is depicted in fig. 2.6. In this case, h is the average segment length.

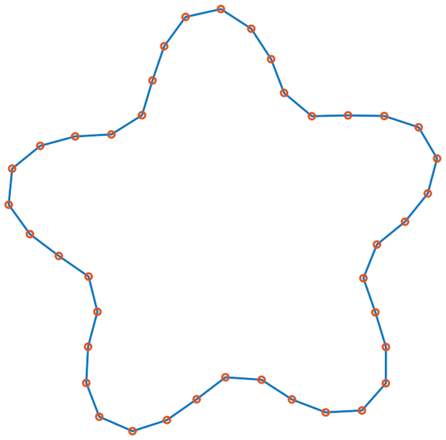

Figure 2.6: *Star like shape discretized with segments.*

2.4.2 Basis Functions

In this work the solution of the integral equation solution is approximated using the Galerkin method or, for some formulations, Petrov-Galerkin method [96]. Using the Galerkin method, the functional space used to discretize the solution and the one used for the testing coincide, while using Petrov-Galerkin method they do not coincide. The geometrical elements described in the previous section serve as domain for the functions used to discretize the problem. An alternative option is to use the Nyström (or collocation) method, that can be seen as a degenerate case of the Galerkin method where Dirac-deltas are used as testing functions, but since with this method it is trickier to prove numerical stability and set error bounds, in this work we avoid its usage. In the following, the functional spaces used to discretize our formulations are presented.

Three-dimensional case

Patch basis functions are scalar polynomial functions of order 0 associated with the triangular cells of the 3D mesh. Each basis function ρ_i has as domain associated cell c_i, and is defined as

$$\rho_i(\boldsymbol{r}) = \begin{cases} A_i^{-1} & \text{if } \boldsymbol{r} \in c_i\,, \\ 0 & \text{otherwise,} \end{cases} \tag{2.91}$$

where A_i is the area of c_i.

Pyramid basis functions are scalar polynomial functions of order 1 associated with the vertices of the 3D mesh. Each basis function λ_i has as domain the cells that have the vertex v_i as one of their vertices, and is defined as

$$\lambda_i(\boldsymbol{r}) = \begin{cases} 1 & \boldsymbol{r} = \boldsymbol{v}_i\,, \\ 0 & \boldsymbol{r} = \boldsymbol{v}_n\,, n \neq i\,, \\ \text{linear} & \text{otherwise.} \end{cases} \tag{2.92}$$

Rao-Wilton-Glisson (RWG) basis functions are vectorial and div-conforming (their divergence is well defined) functions that are capable of correctly discretizing current densities. Each RWG function $\boldsymbol{f}_i$ is associated with one of the N_e edges, and it is defined as

$$\boldsymbol{f}_i(\boldsymbol{r}) = \begin{cases} \dfrac{\boldsymbol{r} - \boldsymbol{r}_i^+}{2A_i^+} & \text{if } \boldsymbol{r} \in c_i^+ \\ -\dfrac{\boldsymbol{r} - \boldsymbol{r}_i^-}{2A_i^-} & \text{if } \boldsymbol{r} \in c_i^-\,, \end{cases} \tag{2.93}$$

where the notation of fig. 2.8 was employed and where $A_i^\pm$ is the area of the cell $c_i^\pm$ [92].

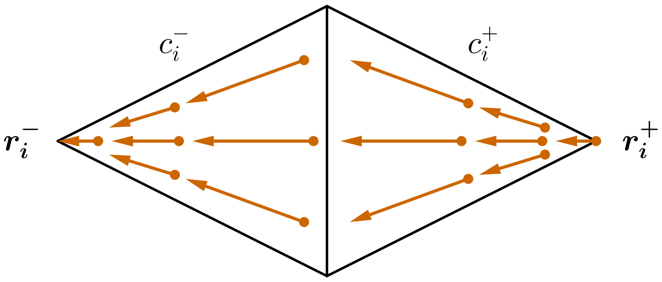

Figure 2.7: *RWG basis functions.*

Two-dimensional case

Triangular basis functions are scalar polynomial functions of order 1 (piecewise linear) associated with the vertices of the 2D mesh, as depicted in fig. 2.8. Each function lives on two segment elements, one relative to its increasing part τ_i^+, and one relative to its decreasing part τ_i^-, defined as

$$\tau_i^+(x) = \frac{x - x_{i-1}}{x_i - x_{i-1}}, \tag{2.94}$$

$$\tau_i^-(x) = \frac{x_{i+1} - x}{x_{i+1} - x_i}. \tag{2.95}$$

The solution and the right hand side (RHS) are approximated by computing or sampling their value at the vertices of the mesh, to which they are associated the coefficients $a_1, a_2, \ldots a_{N_v}$.

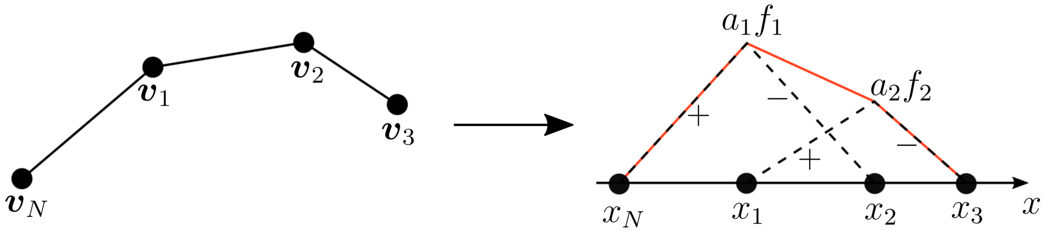

Figure 2.8: *Triangular basis functions in 2D.*

2.4.3 Matrix Building

As anticipated, the defined basis functions are used both to discretize the solution of the problem and as testing functions when using the Galerkin method [96]. The problem is now translated in the solution of a linear algebraic system. In the following we define some of the matrices arising from the discretization of the problems in the standard formulations. In order to simplify the following notation we define the inner product $\langle \boldsymbol{a}, \boldsymbol{b} \rangle = \int_{R^n} \boldsymbol{a} \cdot \boldsymbol{b} \mathrm{d}R^n$.

Three-dimensional case

The unknown current density in the EFIE defined in eq. (2.73) is discretized with RWG basis functions, resulting in the approximation

$$J(\boldsymbol{r}) \approx \sum_{i=1}^{N_e} \langle \boldsymbol{f}_i(\boldsymbol{r}), J(\boldsymbol{r}) \rangle \boldsymbol{f}_i(\boldsymbol{r}), \tag{2.96}$$

from which we define the elements of the vector of the unknown coefficients as

$$\mathbf{j} = \langle f_n, J \rangle. \tag{2.97}$$

Using RWG basis functions also for the testing, the elements of the matrix relative to the $\mathcal{T}_k$ operator defined in eq. (2.67) are computed as

$$\mathbf{T}^{\boldsymbol{f}}_{m,n} = \mathbf{T}_{m,n} = \langle \hat{\boldsymbol{n}} \times f_m, \mathcal{T}_k\left(f_n\right) \rangle, \tag{2.98}$$

and similarly

$$\mathbf{T}^{\boldsymbol{f}}_{\mathrm{s},(m,n)} = \mathbf{T}_{\mathrm{s},(m,n)} = \langle \hat{\boldsymbol{n}} \times f_m, \mathcal{T}_{s,k}\left(f_n\right) \rangle \tag{2.99}$$

$$\mathbf{T}^{\boldsymbol{f}}_{\mathrm{h},(m,n)} = \mathbf{T}_{\mathrm{h},(m,n)} = \langle \hat{\boldsymbol{n}} \times f_m, \mathcal{T}_{h,k}\left(f_n\right) \rangle, \tag{2.100}$$

while the coefficients of the RHS vector as

$$\mathbf{e}_m = \langle \hat{\boldsymbol{n}} \times \boldsymbol{f}_m, \hat{\boldsymbol{n}} \times E^{inc} \rangle.$$

Note that particular attention is required for the computation of the matrix elements in which the Green's function is singular or nearly-singular. Summarizing, the solution of the integral equation is approximated by solving the linear system

$$\mathbf{T}\mathbf{j} = (\mathbf{T}_\mathrm{s} + \mathbf{T}_\mathrm{h})\,\mathbf{j} = \frac{1}{\eta}\mathbf{e}. \tag{2.101}$$

Alternatively, the EFIE can also be discretized using basis functions on the dual mesh defined on the barycentric refinement. For the dual RWG discretization, both Buffa-Christiansen (BC) [21] and Chen-Wilton [24] basis functions can be used. Since this is not the focus of the work, we omit the explicit definitions of the dual elements BC that will be denoted by $\boldsymbol{g}_i$. The reader can refer to [6] and references therein for more details.

In chapter 3 we also need the definition of the standard (RWG) and dual (BC) Gram matrices in 3D whose entries are respectively computed as $\mathbf{G}^{\boldsymbol{f}}{}_{mn} = \mathbf{G}_{mn} = \langle \boldsymbol{f}_m, \boldsymbol{f}_n \rangle$ and $\mathbb{G}^{\boldsymbol{g}}_{mn} = \mathbb{G}_{mn} = \langle \boldsymbol{g}_m, \boldsymbol{g}_n \rangle$. Finally, we also define the Gram matrices corresponding to the patch functions with entries $\mathbf{G}^{\rho}_{mn} = \langle \rho_m, \rho_n \rangle$, and to the pyramids functions with entries $\mathbf{G}^{\lambda}_{mn} = \langle \lambda_m, \lambda_n \rangle$. Also in this case, for the sake of brevity, we omit the definition their dual version, respectively denoted as $\tilde{\rho}_n$ and $\tilde{\lambda}_n$, that can be found in [4]. However, we define the corresponding Gram matrices with entries $\mathbb{G}^{\tilde{\rho}}_{mn} = \langle \tilde{\rho}_m, \tilde{\rho}_n \rangle$ and $\mathbb{G}^{\tilde{\lambda}}_{mn} = \left\langle \tilde{\lambda}_m, \tilde{\lambda}_n \right\rangle$.

Two-dimensional case

The unknown current density present in the TM-EFIE defined in eq. (2.80) is discretized with triangular basis functions, resulting in the approximation

$$J_{s,z}(\boldsymbol{r}) \approx \sum_{i=1}^{N_v} \langle \tau_i(\boldsymbol{r}), J_{s,z}(\boldsymbol{r}) \rangle \tau_i(\boldsymbol{r}), \tag{2.102}$$

from which we define the elements of the vector of the unknown coefficients as

$$\mathbf{j}_{z,n} = \langle \tau_n, J_{s,z} \rangle. \tag{2.103}$$

Using triangular basis functions also for the testing, the elements of the matrix relative to the SLP-2D operator defined in eq. (2.79) are computed as

$$\mathbf{S}^{\tau}_{m,n} = \mathbf{S}_{m,n} = \langle \tau_m, \mathcal{S}\tau_n \rangle \tag{2.104}$$

and the coefficients of the RHS vector as

$$\mathbf{e}_{z,m} = \langle \tau_m, E_z^{inc} \rangle. \tag{2.105}$$

Note that, also in this case, particular attention is required for the computation of the matrix elements in which the Green's function is singular or nearly-singular.

Summarizing, the solution of the integral equation is approximated by solving the linear system

$$jk\mathbf{S}\mathbf{j}_z = \frac{1}{\eta}\mathbf{e}_z. \tag{2.106}$$

Similarly, we can get the linear systems relative to the other formulations, respectively the TM-MFIE, the TE-MFIE and the TE-MFIE, that we report here omitting straightforward passages

$$\left(\frac{1}{2}\mathbf{G} + \mathbf{D}^*\right)\mathbf{j}_z = \mathbf{h}_t \tag{2.107}$$

$$\frac{1}{jk}\mathbf{N}\mathbf{j}_t = \frac{1}{\eta}\mathbf{e}_t \tag{2.108}$$

$$-\left(\frac{1}{2}\mathbf{G} - \mathbf{D}\right)\mathbf{j}_t = \mathbf{h}_z, \tag{2.109}$$

where that $\mathbf{G} = \mathbf{G}^\tau$ is the Gram matrix of the triangular basis functions, with elements computed as $\mathbf{G}^\tau_{m,n} = \langle \tau_m, \tau_n \rangle$.

Chapter 3

New Frontiers in Preconditioning of Electromagnetic Integral Equations

3.1 Computational Complexity and Preconditioning

The computational complexity is a crucial factor for a numerical method. A high computational complexity limits the range of application of a given method, because a simulation requiring years of computation is clearly infeasible. For this reason, it is important to introduce some consideration about the computational complexity of the MoM and to compare it with the one of other computational methods. The FEM, for some applications, is a direct competitor of the MoM for the numerical solution of scattering problems. Pragmatically, both FEM and MoM require the inversion of a matrix to obtain the solution of scattering problems. From this point of view, the main difference between the two methods is that since FEM relies on the discretization of differential equations instead of integral equations, the matrix that needs to be inverted to retrieve the solution is sparse, while for MoM it is generally dense. This fact, in case of equal number of unknowns N in the system, translates into a different computational complexity required for the direct solution of the system, respectively $\mathcal{O}(N^2)$ for FEM and $\mathcal{O}(N^3)$ for MoM. However, if we consider surface integral equations formulations, we actually need to discretize only the surface of the scatterers, while with FEM a volume discretization is always required. In addition, even with the usage of a perfectly matched layer (PML), the discretization of a part of the region external to the scatterer is also required. Moreover, FEM shows numerical instabilities, such as pollution or dispersion [36], that makes the usage of MoM often preferable.

Finally, with proper manipulation of the formulations and compression techniques, it is possible to develop solvers based on MoM that can work in quasi-linear complexity ($N \log N$). Such solvers, denoted as fast solvers, also keep the aforementioned advantages, making MoM a preferential choice over FEM in certain scenarios. In the following we introduce the main steps necessary to build a fast solver.

3.1.1 Iterative Solvers

Alternatively to the direct inversion of the matrix, that requires $\mathcal{O}(N^3)$ operations, linear systems can be solved with iterative solvers based on Krylov subspace methods (or orthogonalized versions of it), such as conjugate gradient, conjugate gradient squared, biconjugate gradient, minimal residual, transpose free quasi-minimal residual or generalized minimal residual methods [98, 63, 94, 100].

These methods require multiple iterations of matrix-vector products (MVPs) between the MoM matrix and a vector that converges to the solution of the system. The number of iteration necessary to converge depends on many characteristics of the involved linear system, and it is difficult to accurately estimate it in advance [91, 55, 98, 17], but one very important parameter is the condition number of the matrix, that is the ratio between the highest and the lowest singular values of the matrix. In addition to its impact on the convergence of the iterative solver, the condition number also limits the numerical accuracy that can be achieved with the computation, and in both cases a low condition number is desirable.

In practical cases, if the MoM matrix is well conditioned and shows other spectral proprieties, such as clustering of eigenvalues, an iterative solver can converge in a number of iterations N_I that is negligible when compared with the number of unknowns N. In this case, if also N_I does not depend on N, the computational complexity required to solve the problem scales as the one of the MVP operation, that in case of general dense matrices is $\mathcal{O}(N^2)$.

3.1.2 Conditioning and Preconditioning

Because of the aforementioned reasons, when using MoM, it is really important to study the behavior of the condition number in the regimes that are relevant for its application. If a scenario where the condition number grows problematically is encountered, in some cases, it is also possible to avoid this growth and reduce the condition number by using preconditioning schemes. Those techniques allow reducing the condition number of the matrix to be inverted and thus improve the quality of the solution and the computational speed of the solver. For this reason, preconditioning is in itself a research topic in the CEM community and a central one in this work.

Considering the linear system $\mathbf{Ax} = \mathbf{v}$, we talk about left preconditioning if we solve the system $\mathbf{LAx} = \mathbf{Lb}$ inverting the preconditioned matrix $\mathbf{LA}$, while we talk about right preconditioning if we solve the system $\mathbf{AR}\tilde{\mathbf{x}} = \mathbf{b}$ inverting the preconditioned matrix $\mathbf{AR}$ and we then retrieve the solution with $\mathbf{x} = \mathbf{R}\tilde{\mathbf{x}}$. In general, nothing prevents us from using both right and left preconditioning at the same time, and it is actually necessary if we want the matrix to be inverted to be symmetric (useful property for certain applications).

3.1.3 Fast Solvers

We have seen already that when we use an iterative solver, and we have $N \gg N_I$ and N_I does not depend on N, the computational complexity is leaded by the one required for the MVP. Leveraging fast algorithms, it is possible to reduce the computational complexity from $\mathcal{O}(N^2)$ of the dense MoM matrix MVP to $\mathcal{O}(N \log N)$. There are different fast algorithms suitable for different applications. Between them we cite here the Adaptive Cross Approximation (ACA) [16, 114] and its Multi Level variant (MLACA) [44, 22], that can be used to compress matrices relative to static, quasi-static and low frequency problems, and the Fast Multiple Method (FMM) [29] and its multilevel variant (MLFMM) [83] that instead can be used to compress matrices arising from medium and high frequency simulations. Summarizing, with fast algorithms we have all the ingredients necessary to build a fast numerical solver for electromagnetic integral equations.

3.2 Conditioning Issues of Electromagnetic Integral Equations

The boundary element method suffers from conditioning issues that can make it unusable in certain regimes. In the following, the main regimes of interest in practical applications are reported, as well as an overview of the currently available preconditioning solutions in such regimes.

3.2.1 Low-Frequency Breakdown

For the three-dimensional case, in the static limit, the decoupling of the electric and the magnetic fields translates in a source of ill-conditioning of the problem [75]. This phenomenon is known in literature as the low-frequency breakdown. In addition to the conditioning issue, it implies other challenges to be faced to accurately compute the scattered field, such as numerical cancellation in the RHS of the equation. Several strategies have been proposed to solve those problems, and among them we mention the loop-star and loop-tree decomposition [106], quasi-Helmholtz projectors [7, 9], the current-charge formulation [104], the augmented EFIE [90] and the potential-based formulations [107, 66]. Details on their characteristic and implementation can be found in [5] and references therein.

3.2.2 Dense-Discretization Breakdown

Another relevant phenomenon that yields ill-conditioning of BEM formulations is the dense-discretization breakdown. In the usage and testing of numerical solvers, it is fundamental to have the possibility to improve the numerical accuracy by further discretizing the geometry. The regime in which we reduce the average edge length of the mesh h, attempting to improve the numerical accuracy of the solver, is called h-refinement.

Unfortunately, several of the standard EFIE-based formulations, both in 2D and in 3D, show a condition number that grows when $h \to 0$. A way to explain this phenomenon relies on pseudo-differential operators theory [27, 78]. Indeed, without going into theoretical details, the pseudo-differential order of an operator is related with its spectral properties in the elliptic region, the region associated with the high spatial frequency component of the operator. In particular, there is a relation between the pseudo-differential order of an operator and the behavior of the singular values in its elliptic region when $h \to 0$. For instance, if we consider operators with positive pseudo-differential order, behave as a derivative operator, showing a divergent singular values spectrum, while operators with negative pseudo-differential order, showing a spectrum clustering to zero singular values. Both behaviors are undesirable since in such cases the condition number grows. Indeed, it is fundamental that the operator to be inverted has singular values that accumulate to a constant values when performing h-refinement.

A category of operators with this propriety are the ones involved in second-kind Fredholm integral equations, that for brevity we call second-kind operators. Typically, such operators $\mathcal{F}$, for which we have $\mathcal{F} = \mathcal{O} + \mathcal{K}$, where the operator $\mathcal{O}$ is spectrally equivalent to the identity operator ($\mathcal{O} \asymp \mathcal{I}$) and $\mathcal{K}$ is a compact operator, whose discretization gives rise to matrices with singular values clustering to 0. For such operators, we have $\mathcal{F} \asymp \mathcal{I}$, so the singular values accumulates to a constant value. For this reason, to solve the dense-discretization breakdown, many preconditioning techniques, such as Calderón-based schemes [8], aim to get a preconditioned operator that results in a second-kind operator. In order to achieve this, those preconditioning techniques rely on the key fact that when an operator is applied to another operator their pseudo-differential order is summed. Indeed, preconditioning a pseudo-differential operator with another operator of opposite pseudo-differential order often gives rise to a well-conditioned operator of pseudo-differential order 0 that spectrally behaves like a second-kind operator. In the following section 3.3 we present a new preconditioning technique, recently proposed in [80], that tackles simultaneously both the low-frequency and the dense-discretization breakdowns.

3.2.3 High-Frequency Issues

At high-frequency, or more precisely for electrically-large scatterers, there are two main sources of ill-conditioning occurring in electromagnetic integral equations. When the wavelength λ is comparable with the size of the scatterer, we enter in the resonant regime of the structure. In this regime, the operators involved in the EFIEs and the ones involved in the MFIEs suffer from interior resonances. This phenomenon translates in operators that, when correctly discretized [32], show a nullspace, and are thus ill-conditioned. For this reason, in the resonant regime, Combined Field Integral Equations (CFIEs) [1] or Combined Source Integral Equations (CSIEs) [74] are usually employed. When combined with Calderón strategies, particular attention should be given to the discretization and the wave numbers of the operator involved in the preconditioning [79].

If we consider the so called high-frequency regime, in which we keep constant the ratio between the wave number λ and the mesh size h ($\lambda/h = c$, where we should have at least $c > 5$ to properly discretize the problem), we have other issues occurring that limit the convergence speed of the iterative solvers and the numerical accuracy. Since the solution of these problems is part of the focus of chapter 4, more details are presented in it, and are not repeated here.

3.3 A Novel Preconditioning Technique for Electromagnetic Integral Equations

As anticipated, in this section we present a preconditioning scheme recently introduced in [80]. The scheme is used to solve both the low-frequency and the dense-discretization breakdowns of the 3D EFIE, as defined in eq. (2.101). The work also relies on the usage of the quasi-Helmholtz decomposition mentioned in section 3.2.1, that we introduce here.

If we consider the continuous problem defined in eq. (2.73), the solution $\boldsymbol{J}$ can be decomposed into solenoidal, irrotational and harmonic components

$$\boldsymbol{J} = \nabla \times \hat{\boldsymbol{n}}\lambda + \nabla_s \phi + \boldsymbol{h}\,. \tag{3.1}$$

Notice that on simply-connected boundary of the scatterer (genus-0 surface) the harmonic component, that is both solenoidal and irrotational, is not present. When using BEM with RWGs as testing and source basis functions, eq. (3.1) has its discrete counterpart

$$\mathbf{j} = \mathbf{\Lambda}\mathbf{l} + \mathbf{\Sigma}\boldsymbol{\sigma} + \mathbf{H}\mathbf{h}\,, \tag{3.2}$$

where $\mathbf{\Lambda} \in \mathbb{R}^{N \times N_L}$ and $\mathbf{\Sigma} \in \mathbb{R}^{N \times N_S}$ (with $N = N_e$, $N_S = N_t$, $N_L = N_v$) are the Loop-to-RWG and Star-to-RWG transformation matrices [76, 64, 111, 105, 10]. Since RWG basis functions are not curl-conforming, the discretized counterparts of the irrotational and harmonic components are only non-solenoidal and quasi-harmonic. Following the convention of fig. 2.7 and eq. (2.93), we can compute their elements as

$$[\mathbf{\Lambda}]_{mn} = \begin{cases} 1 & \text{if node } n \text{ equals } v_m^+\,, \\ -1 & \text{if node } n \text{ equals } v_m^-\,, \\ 0 & \text{otherwise,} \end{cases} \tag{3.3}$$

and

$$[\mathbf{\Sigma}]_{mn} = \begin{cases} 1 & \text{if the cell } n \text{ equals } c_m^+\,, \\ -1 & \text{if the cell } n \text{ equals } c_m^-\,, \\ 0 & \text{otherwise.} \end{cases} \tag{3.4}$$

Since not needed, the explicit definition of the matrix $\mathbf{H}$ is omitted, however it could be found in [6] and references therein.

We highlight the fact that $\mathbf{\Lambda}^{\mathrm{T}}\mathbf{\Lambda}$ and $\mathbf{\Sigma}^{\mathrm{T}}\mathbf{\Sigma}$ are respectively the vertices- and the cells-based graph Laplacians [10]. We can now define the standard quasi-Helmholtz projectors as

$$\begin{aligned} \mathbf{P}^{\Sigma} &= \mathbf{\Sigma}\left(\mathbf{\Sigma}^{\mathrm{T}}\mathbf{\Sigma}\right)^{+}\mathbf{\Sigma}^{\mathrm{T}}\,, \\ \mathbf{P}^{\Lambda H} &= \mathbf{I} - \mathbf{P}^{\Sigma} \end{aligned} \tag{3.5}$$

for the primal ones (where $^{+}$ denotes the Moore-Penrose pseudo-inverse),

$$\begin{aligned} \mathbb{P}^{\Lambda} &= \mathbf{\Lambda}\left(\mathbf{\Lambda}^{\mathrm{T}}\mathbf{\Lambda}\right)^{+}\mathbf{\Lambda}^{\mathrm{T}}\,, \\ \mathbb{P}^{\Sigma H} &= \mathbf{I} - \mathbb{P}^{\Lambda} \end{aligned} \tag{3.6}$$

for the dual ones, and

$$\mathbf{P}^{H}\left(=\mathbb{P}^{H}\right) = \mathbf{I} - \mathbf{P}^{\Sigma} - \mathbb{P}^{\Lambda} \tag{3.7}$$

for the projector to quasi-harmonic subspace [10, 12].

3.3.1 Laplacian Filtered Loop-Star Decomposition

We now introduce the concept of filtered Loop-Star bases. After introducing their standard forms and related properties, we generalize to the case of inhomogeneous meshes.

The Standard Case

In the following, with $\mathbf{X} \in \mathbb{R}^{N \times N_x}$ we refer to a matrix that could be ether $\mathbf{\Sigma}$ or $\mathbf{\Lambda}$. To facilitate the introduction of the concept we make use of the singular values decomposition (SVD)

$$\mathbf{X} = \mathbf{U_X}\mathbf{S_X}\mathbf{V_X}^{\dagger}, \tag{3.8}$$

with $\mathbf{U_X} \in \mathbb{R}^{N\times N}$, $\mathbf{V_X} \in \mathbb{R}^{N_x\times N_x}$, and $\mathbf{S_X} \in \mathbb{R}^{N\times N_x}$ [40]. The matrix $\mathbf{S_X}$ is block diagonal and contains the singular values $\sigma_{\mathbf{X},i}$ of $\mathbf{X}$ as entries (in decreasing order), while the matrices $\mathbf{U_X}$ and $\mathbf{V_X}$ are unitary and their columns are the left/right singular vectors of $\mathbf{X}$. Since in both cases $\mathbf{X}$ is a real matrix, we have that the SVD of $(\mathbf{X}^{\mathrm{T}}\mathbf{X})$ equals $\mathbf{V_X}\mathbf{S}_\mathbf{X}^{\mathrm{T}}\mathbf{S_X}\mathbf{V}_\mathbf{X}^{\dagger}$. We define the diagonal matrix $\mathbf{L}_{\mathbf{X},n} \in \mathbb{R}^{N_x\times N_x}$, with $1 \leq n \leq N_x$, such that

$$[\mathbf{L}_{\mathbf{X},n}]_{ii} = \begin{cases} \sigma_{\mathbf{X},i} & \text{if } i > N_x - n\,, \\ 0 & \text{otherwise,} \end{cases} \tag{3.9}$$

and the filtered graph Laplacians

$$(\mathbf{X}^{\mathrm{T}}\mathbf{X})_n \coloneqq \mathbf{V_X}\mathbf{L}^2_{\mathbf{X},n}\mathbf{V}^{\dagger}_{\mathbf{X}}\,, \tag{3.10}$$

that we use to finally introduce the filtered Star-to-RWG matrices and filtered Loop-to-RWG

$$\mathbf{\Sigma}_n = \mathbf{\Sigma}\left(\mathbf{\Sigma}^{\mathrm{T}}\mathbf{\Sigma}\right)^+\left(\mathbf{\Sigma}^{\mathrm{T}}\mathbf{\Sigma}\right)_n\,, \tag{3.11}$$

$$\mathbf{\Lambda}_n = \mathbf{\Lambda}\left(\mathbf{\Lambda}^{\mathrm{T}}\mathbf{\Lambda}\right)^+\left(\mathbf{\Lambda}^{\mathrm{T}}\mathbf{\Lambda}\right)_n\,. \tag{3.12}$$

Properties

We now mention some properties of the filtered Loop-Star matrices. Because $\mathbf{\Sigma}^{\mathrm{T}}\mathbf{\Lambda} = \mathbf{0}$ [6], we have

$$\mathbf{\Sigma}^{\mathrm{T}}_n\mathbf{\Lambda}_m = \left(\mathbf{\Sigma}^{\mathrm{T}}\mathbf{\Sigma}\right)_n\left(\mathbf{\Sigma}^{\mathrm{T}}\mathbf{\Sigma}\right)^+\mathbf{\Sigma}^{\mathrm{T}}\mathbf{\Lambda}\left(\mathbf{\Lambda}^{\mathrm{T}}\mathbf{\Lambda}\right)^+\left(\mathbf{\Lambda}^{\mathrm{T}}\mathbf{\Lambda}\right)_m = \mathbf{0} \qquad \forall n,m, \tag{3.13}$$

meaning that the filtered Loop-Star functions are coefficient-orthogonal (l^2-orthogonal) like their non-filtered counterparts.

From the definition of $\mathbf{L}_{\mathbf{X},n}$ in (3.9), it follows that $\mathbf{L}_{\mathbf{X},n}\mathbf{L}_{\mathbf{X},m} = \mathbf{L}^2_{\mathbf{X},\min\{n,m\}}$. Thus from (3.10)

$$\begin{aligned}(\mathbf{X}^{\mathrm{T}}\mathbf{X})_n(\mathbf{X}^{\mathrm{T}}\mathbf{X})_m &= \mathbf{V_X}\mathbf{L}_{\mathbf{X},n}\mathbf{V}^{\mathrm{T}}_{\mathbf{X}}\mathbf{V_X}\mathbf{L}_{\mathbf{X},m}\mathbf{V}^{\mathrm{T}}_{\mathbf{X}} \\ &= \mathbf{V_X}\mathbf{L}_{\mathbf{X},n}\mathbf{L}_{\mathbf{X},m}\mathbf{V}^{\mathrm{T}}_{\mathbf{X}} = \mathbf{V_X}\mathbf{L}_{\mathbf{X},\min\{n,m\}}\mathbf{L}_{\mathbf{X},\min\{n,m\}}\mathbf{V}^{\mathrm{T}}_{\mathbf{X}} \\ &= \mathbf{V_X}\mathbf{L}_{\mathbf{X},\min\{n,m\}}\mathbf{V}^{\mathrm{T}}_{\mathbf{X}}\mathbf{V_X}\mathbf{L}_{\mathbf{X},\min\{n,m\}}\mathbf{V}^{\mathrm{T}}_{\mathbf{X}} \\ &= (\mathbf{X}^{\mathrm{T}}\mathbf{X})^2_{\min\{n,m\}}\,.\end{aligned} \tag{3.14}$$

We thus have

$$\begin{aligned}\mathbf{\Sigma}^{\mathrm{T}}_m\mathbf{\Sigma}_n &= \left(\mathbf{\Sigma}^{\mathrm{T}}\mathbf{\Sigma}\right)_m\left(\mathbf{\Sigma}^{\mathrm{T}}\mathbf{\Sigma}\right)^+\mathbf{\Sigma}^{\mathrm{T}}\mathbf{\Sigma}\left(\mathbf{\Sigma}^{\mathrm{T}}\mathbf{\Sigma}\right)^+\left(\mathbf{\Sigma}^{\mathrm{T}}\mathbf{\Sigma}\right)_n \\ &= \left(\mathbf{\Sigma}^{\mathrm{T}}\mathbf{\Sigma}\right)^+\left(\mathbf{\Sigma}^{\mathrm{T}}\mathbf{\Sigma}\right)_m\left(\mathbf{\Sigma}^{\mathrm{T}}\mathbf{\Sigma}\right)_n \\ &= \left(\mathbf{\Sigma}^{\mathrm{T}}\mathbf{\Sigma}\right)^+\left(\mathbf{\Sigma}^{\mathrm{T}}\mathbf{\Sigma}\right)_{\min\{n,m\}}\left(\mathbf{\Sigma}^{\mathrm{T}}\mathbf{\Sigma}\right)_{\min\{n,m\}} \\ &= \mathbf{\Sigma}^{\mathrm{T}}_{\min\{n,m\}}\mathbf{\Sigma}_{\min\{n,m\}}\,.\end{aligned} \tag{3.15}$$

Similarly,

$$\mathbf{\Lambda}_m^{\mathrm{T}}\mathbf{\Lambda}_n = \mathbf{\Lambda}_{\min\{n,m\}}^{\mathrm{T}}\mathbf{\Lambda}_{\min\{n,m\}}. \tag{3.16}$$

We now introduce two properties that show that non-intersecting differences of filtered Star or Loop bases are mutually orthogonal and thus generate linearly independent spaces. Given integers such that $m < n < p < q$, we have

$$\left(\mathbf{\Sigma}_m - \mathbf{\Sigma}_n\right)^{\mathrm{T}}\left(\mathbf{\Sigma}_p - \mathbf{\Sigma}_q\right) = \mathbf{\Sigma}_m^{\mathrm{T}}\left(\mathbf{\Sigma}_p - \mathbf{\Sigma}_q\right) - \mathbf{\Sigma}_n^{\mathrm{T}}\left(\mathbf{\Sigma}_p - \mathbf{\Sigma}_q\right) = \mathbf{0}, \tag{3.17}$$

and similarly,

$$\left(\mathbf{\Lambda}_m - \mathbf{\Lambda}_n\right)^{\mathrm{T}}\left(\mathbf{\Lambda}_p - \mathbf{\Lambda}_q\right) = \mathbf{0}\,. \tag{3.18}$$

These properties are useful to build invertible changes of basis.

Generalization for Inhomogeneous Meshes

When the discretization of the geometry is inhomogeneous, both the standard discretizations of the EFIE and the graph Laplacian matrices may fail to properly mimic the spectral properties of their continuous counterparts, resulting in an ill-conditioning of the matrix. In order to improve the performance of the solver in such cases, we introduce a version of EFIE and Loop-Star matrices normalized with fractional power of Gram matrices, in particular we define

$$\tilde{\mathbf{T}} = \mathbf{G}^{-1/2}\mathbf{T}\mathbf{G}^{-1/2}\,, \tag{3.19}$$

$$\tilde{\mathbf{T}}_{\mathrm{s}} = \mathbf{G}^{-1/2}\mathbf{T}_{\mathrm{s}}\mathbf{G}^{-1/2}\,, \tag{3.20}$$

$$\tilde{\mathbf{T}}_{\mathrm{h}} = \mathbf{G}^{-1/2}\mathbf{T}_{\mathrm{h}}\mathbf{G}^{-1/2}\,, \tag{3.21}$$

and

$$\tilde{\mathbf{\Sigma}} = \mathbf{G}^{-1/2}\mathbf{\Sigma}\mathbf{G}_p^{1/2}\,, \tag{3.22}$$

$$\tilde{\mathbf{\Lambda}} = \mathbf{G}^{1/2}\mathbf{\Lambda}\mathbf{G}_\lambda^{-1/2}\,. \tag{3.23}$$

Consistently, the normalized filtered Loop-Star matrices ((3.11) and (3.12)) are defined as

$$\tilde{\mathbf{\Sigma}}_n = \tilde{\mathbf{\Sigma}}\left(\tilde{\mathbf{\Sigma}}^{\mathrm{T}}\tilde{\mathbf{\Sigma}}\right)^{+}\left(\tilde{\mathbf{\Sigma}}^{\mathrm{T}}\tilde{\mathbf{\Sigma}}\right)_n\,, \tag{3.24}$$

$$\tilde{\mathbf{\Lambda}}_n = \tilde{\mathbf{\Lambda}}\left(\tilde{\mathbf{\Lambda}}^{\mathrm{T}}\tilde{\mathbf{\Lambda}}\right)^{+}\left(\tilde{\mathbf{\Lambda}}^{\mathrm{T}}\tilde{\mathbf{\Lambda}}\right)_n\,. \tag{3.25}$$

When we work with dual Loop-Star decomposition matrices, the normalization need to be consistent with the dual basis functions used for the discretization, so we also define the dually-normalized Loop and Star transformation matrices as

$$\tilde{\mathbb{\Sigma}} = \mathbb{G}^{1/2}\mathbf{\Sigma}\mathbb{G}_{\tilde{\lambda}}^{-1/2}\,, \tag{3.26}$$

$$\tilde{\mathbb{\Lambda}} = \mathbb{G}^{-1/2}\mathbf{\Lambda}\mathbb{G}_{\tilde{p}}^{1/2}\,, \tag{3.27}$$

and consequently

$$\tilde{\mathbb{\Sigma}}_n = \tilde{\mathbb{\Sigma}} \left(\tilde{\mathbb{\Sigma}}^{\mathrm{T}} \tilde{\mathbb{\Sigma}} \right)^{+} \left(\tilde{\mathbb{\Sigma}}^{\mathrm{T}} \tilde{\mathbb{\Sigma}} \right)_n , \tag{3.28}$$

$$\tilde{\mathbb{\Lambda}}_n = \tilde{\mathbb{\Lambda}} \left(\tilde{\mathbb{\Lambda}}^{\mathrm{T}} \tilde{\mathbb{\Lambda}} \right)^{+} \left(\tilde{\mathbb{\Lambda}}^{\mathrm{T}} \tilde{\mathbb{\Lambda}} \right)_n . \tag{3.29}$$

The orthogonality properties are maintained also from the primal and dual normalized Loop-Star, so we have

$$\tilde{\mathbf{\Lambda}}^{\mathrm{T}} \tilde{\mathbf{\Sigma}} = \mathbf{G}_{\lambda}^{-1/2} \mathbf{\Lambda}^{\mathrm{T}} \mathbf{G}^{1/2} \mathbf{G}^{-1/2} \mathbf{\Sigma} \mathbf{G}_{p}^{1/2} = \mathbf{0} , \tag{3.30}$$

$$\tilde{\mathbb{\Sigma}}^{\mathrm{T}} \tilde{\mathbb{\Lambda}} = \mathbb{G}_{\tilde{p}}^{1/2} \mathbf{\Sigma}^{\mathrm{T}} \mathbb{G}^{-1/2} \mathbb{G}^{1/2} \mathbf{\Lambda} \mathbb{G}_{\tilde{\lambda}}^{-1/2} = \mathbf{0} , \tag{3.31}$$

because $\mathbf{\Sigma}^{\mathrm{T}} \mathbf{\Lambda} = \mathbf{0}$. Moreover, since (3.14) holds, we also have that

$$\tilde{\mathbf{\Sigma}}_m^{\mathrm{T}} \tilde{\mathbf{\Sigma}}_n = \tilde{\mathbf{\Sigma}}_{\min\{n,m\}}^{\mathrm{T}} \tilde{\mathbf{\Sigma}}_{\min\{n,m\}} , \tag{3.32}$$

$$\tilde{\mathbf{\Lambda}}_m^{\mathrm{T}} \tilde{\mathbf{\Lambda}}_n = \tilde{\mathbf{\Lambda}}_{\min\{n,m\}}^{\mathrm{T}} \tilde{\mathbf{\Lambda}}_{\min\{n,m\}} , \tag{3.33}$$

$$\tilde{\mathbb{\Lambda}}_m^{\mathrm{T}} \tilde{\mathbb{\Lambda}}_n = \tilde{\mathbb{\Lambda}}_{\min\{n,m\}}^{\mathrm{T}} \tilde{\mathbb{\Lambda}}_{\min\{n,m\}} , \tag{3.34}$$

$$\tilde{\mathbb{\Sigma}}_m^{\mathrm{T}} \tilde{\mathbb{\Sigma}}_n = \tilde{\mathbb{\Sigma}}_{\min\{n,m\}}^{\mathrm{T}} \tilde{\mathbb{\Sigma}}_{\min\{n,m\}} . \tag{3.35}$$

Finally, also the counterparts of (3.17) and (3.18) can be obtained by replacing each matrix with its normalized ("tilde") counterpart. The other properties previously presented for the the standard non-normalized filtered Loop-Star matrices also hold.

3.3.2 Quasi-Helmholtz Laplacian Filters

We now leverage the above defined filtered Loop-Star functions to introduce the quasi-Helmholtz Laplacian filters. Similarly to what is done with the quasi-Helmholtz projectors, we have an implicit Helmholtz decomposition, that allows us to implement the proposed preconditioning approach. Indeed, similarly to what is done with the standard quasi-Helmholtz projectors, we can obtain the quasi-Helmholtz Laplacian filters, which offer the same preconditioning capabilities as the filtered Loop and Star bases and at the same the advantages of a basis-free technique, avoiding the need of detection of global-loop for multiply connected scatterers.

The Standard Case

Following the definitions (3.5) and (3.6), and replacing the standard Loop-Star basis with the new filtered sets, we obtain

$$\begin{aligned}\boldsymbol{\Sigma}_n\left(\boldsymbol{\Sigma}_n^{\mathrm{T}}\boldsymbol{\Sigma}_n\right)^{+}\boldsymbol{\Sigma}_n^{\mathrm{T}} = \boldsymbol{\Sigma}\left(\boldsymbol{\Sigma}^{\mathrm{T}}\boldsymbol{\Sigma}\right)^{+}\left(\boldsymbol{\Sigma}^{\mathrm{T}}\boldsymbol{\Sigma}\right)_n &\\ \left(\left(\boldsymbol{\Sigma}^{\mathrm{T}}\boldsymbol{\Sigma}\right)_n\left(\boldsymbol{\Sigma}^{\mathrm{T}}\boldsymbol{\Sigma}\right)^{+}\boldsymbol{\Sigma}^{\mathrm{T}}\boldsymbol{\Sigma}\left(\boldsymbol{\Sigma}^{\mathrm{T}}\boldsymbol{\Sigma}\right)^{+}\left(\boldsymbol{\Sigma}^{\mathrm{T}}\boldsymbol{\Sigma}\right)_n\right)^{+} &\\ \left(\boldsymbol{\Sigma}^{\mathrm{T}}\boldsymbol{\Sigma}\right)_n\left(\boldsymbol{\Sigma}^{\mathrm{T}}\boldsymbol{\Sigma}\right)^{+}\boldsymbol{\Sigma}^{\mathrm{T}} = \boldsymbol{\Sigma}\left(\boldsymbol{\Sigma}^{\mathrm{T}}\boldsymbol{\Sigma}\right)_n^{+}\boldsymbol{\Sigma}^{\mathrm{T}}\,, &\end{aligned} \tag{3.36}$$

and, similarly,

$$\boldsymbol{\Lambda}_n\left(\boldsymbol{\Lambda}_n^{\mathrm{T}}\boldsymbol{\Lambda}_n\right)^{+}\boldsymbol{\Lambda}_n^{\mathrm{T}} = \boldsymbol{\Lambda}\left(\boldsymbol{\Lambda}^{\mathrm{T}}\boldsymbol{\Lambda}\right)_n^{+}\boldsymbol{\Lambda}^{\mathrm{T}}\,. \tag{3.37}$$

From this we define the primal quasi-Helmholtz Laplacian filters

$$\mathbf{P}_n^{\Sigma} = \boldsymbol{\Sigma}\left(\boldsymbol{\Sigma}^{\mathrm{T}}\boldsymbol{\Sigma}\right)_n^{+}\boldsymbol{\Sigma}^{\mathrm{T}}\,, \tag{3.38}$$

$$\mathbf{P}_n^{\Lambda H} = \boldsymbol{\Lambda}\left(\boldsymbol{\Lambda}^{\mathrm{T}}\boldsymbol{\Lambda}\right)_n^{+}\boldsymbol{\Lambda}^{\mathrm{T}} + \mathbf{I} - \mathbf{P}^{\Sigma} - \mathbb{P}^{\Lambda} \tag{3.39}$$

and dual ones

$$\mathbb{P}_n^{\Lambda} = \boldsymbol{\Lambda}\left(\boldsymbol{\Lambda}^{\mathrm{T}}\boldsymbol{\Lambda}\right)_n^{+}\boldsymbol{\Lambda}^{\mathrm{T}}\,, \tag{3.40}$$

$$\mathbb{P}_n^{\Sigma H} = \boldsymbol{\Sigma}\left(\boldsymbol{\Sigma}^{\mathrm{T}}\boldsymbol{\Sigma}\right)_n^{+}\boldsymbol{\Sigma}^{\mathrm{T}} + \mathbf{I} - \mathbb{P}^{\Lambda} - \mathbf{P}^{\Sigma}\,. \tag{3.41}$$

Note that, in the special case of simply connected geometries $\mathbf{P}_n^{\Lambda H} = \boldsymbol{\Lambda}\left(\boldsymbol{\Lambda}^{\mathrm{T}}\boldsymbol{\Lambda}\right)_n^{+}\boldsymbol{\Lambda}^{\mathrm{T}}$ and $\mathbb{P}_n^{\Sigma H} = \boldsymbol{\Sigma}\left(\boldsymbol{\Sigma}^{\mathrm{T}}\boldsymbol{\Sigma}\right)_n^{+}\boldsymbol{\Sigma}^{\mathrm{T}}$ since $\mathbb{P}^{\Lambda} + \mathbf{P}^{\Sigma} = \mathbf{I}$. In addition, in case $n = N_X$, we have

$$\mathbf{P}_{N_S}^{\Sigma} = \mathbf{P}^{\Sigma}\,, \tag{3.42}$$

$$\mathbb{P}_{N_L}^{\Lambda} = \mathbb{P}^{\Lambda}\,, \tag{3.43}$$

$$\mathbf{P}_{N_L}^{\Lambda H} = \mathbb{P}^{\Lambda} + \mathbf{I} - \mathbf{P}^{\Sigma} - \mathbb{P}^{\Lambda} = \mathbf{P}^{\Lambda H}\,, \tag{3.44}$$

$$\mathbb{P}_{N_S}^{\Sigma H} = \mathbf{P}^{\Sigma} + \mathbf{I} - \mathbb{P}^{\Lambda} - \mathbf{P}^{\Sigma} = \mathbb{P}^{\Sigma H}\,, \tag{3.45}$$

which means that, the quasi-Helmholtz Laplacian filters converge to the standard quasi-Helmholtz projectors in such cases.

Properties

Here we list some useful properties of the quasi-Helmholtz Laplacian filters that are retrieved from their definitions. Primarily, we can see that the filters are still projectors, since

$$\begin{aligned}\mathbf{P}^{\Sigma}_{n}\mathbf{P}^{\Sigma}_{n} &= \boldsymbol{\Sigma}\left(\boldsymbol{\Sigma}^{\mathrm{T}}\boldsymbol{\Sigma}\right)^{+}_{n}\boldsymbol{\Sigma}^{\mathrm{T}}\boldsymbol{\Sigma}\left(\boldsymbol{\Sigma}^{\mathrm{T}}\boldsymbol{\Sigma}\right)^{+}_{n}\boldsymbol{\Sigma}^{\mathrm{T}}\\ &= \boldsymbol{\Sigma}\left(\boldsymbol{\Sigma}^{\mathrm{T}}\boldsymbol{\Sigma}\right)^{+}_{n}\boldsymbol{\Sigma}^{\mathrm{T}} = \mathbf{P}^{\Sigma}_{n}\,,\end{aligned}\tag{3.46}$$

$$\begin{aligned}\mathbb{P}^{\Lambda}_{n}\mathbb{P}^{\Lambda}_{n} &= \boldsymbol{\Lambda}\left(\boldsymbol{\Lambda}^{\mathrm{T}}\boldsymbol{\Lambda}\right)^{+}_{n}\boldsymbol{\Lambda}^{\mathrm{T}}\boldsymbol{\Lambda}\left(\boldsymbol{\Lambda}^{\mathrm{T}}\boldsymbol{\Lambda}\right)^{+}_{n}\boldsymbol{\Lambda}^{\mathrm{T}}\\ &= \boldsymbol{\Lambda}\left(\boldsymbol{\Lambda}^{\mathrm{T}}\boldsymbol{\Lambda}\right)^{+}_{n}\boldsymbol{\Lambda}^{\mathrm{T}} = \mathbb{P}^{\Lambda}_{n}\,,\end{aligned}\tag{3.47}$$

and, similarly,

$$\mathbf{P}^{\Lambda H}_{n}\mathbf{P}^{\Lambda H}_{n} = \mathbf{P}^{\Lambda H}_{n}\,,\tag{3.48}$$

$$\mathbb{P}^{\Sigma H}_{n}\mathbb{P}^{\Sigma H}_{n} = \mathbb{P}^{\Sigma H}_{n}\,.\tag{3.49}$$

In addition, using the properties $\boldsymbol{\Sigma}^{\mathrm{T}}\boldsymbol{\Lambda} = \mathbf{0}$ and $\boldsymbol{\Sigma}^{\mathrm{T}}\left(\mathbf{I} - \mathbf{P}^{\Sigma} - \mathbb{P}^{\Lambda}\right) = \mathbf{0}$, we also have that $\forall m, n$

$$\mathbf{P}^{\Sigma}_{m}\mathbf{P}^{\Lambda H}_{n} = \boldsymbol{\Sigma}\left(\boldsymbol{\Sigma}^{\mathrm{T}}\boldsymbol{\Sigma}\right)^{+}_{n}\boldsymbol{\Sigma}^{\mathrm{T}}\boldsymbol{\Lambda}\left(\boldsymbol{\Lambda}^{\mathrm{T}}\boldsymbol{\Lambda}\right)^{+}_{n}\boldsymbol{\Lambda}^{\mathrm{T}} + \boldsymbol{\Sigma}\left(\boldsymbol{\Sigma}^{\mathrm{T}}\boldsymbol{\Sigma}\right)^{+}_{n}\boldsymbol{\Sigma}^{\mathrm{T}}\left(\mathbf{I} - \mathbf{P}^{\Sigma} - \mathbb{P}^{\Lambda}\right)\tag{3.50}$$

$$= \mathbf{0}\,,\tag{3.51}$$

and similarly for the dual projectors

$$\mathbb{P}^{\Lambda}_{m}\mathbb{P}^{\Sigma H}_{n} = \mathbf{0}\,,\quad \forall m, n\,.\tag{3.52}$$

For integers $m < n < p < q$, using (3.14), we have the following orthogonality properties

$$\begin{aligned}&\left(\mathbf{P}^{\Sigma}_{m} - \mathbf{P}^{\Sigma}_{n}\right)\left(\mathbf{P}^{\Sigma}_{p} - \mathbf{P}^{\Sigma}_{q}\right)\\ &\quad= \left(\boldsymbol{\Sigma}\left(\boldsymbol{\Sigma}^{\mathrm{T}}\boldsymbol{\Sigma}\right)^{+}_{m}\boldsymbol{\Sigma}^{\mathrm{T}} - \boldsymbol{\Sigma}\left(\boldsymbol{\Sigma}^{\mathrm{T}}\boldsymbol{\Sigma}\right)^{+}_{n}\boldsymbol{\Sigma}^{\mathrm{T}}\right)\\ &\qquad\left(\boldsymbol{\Sigma}\left(\boldsymbol{\Sigma}^{\mathrm{T}}\boldsymbol{\Sigma}\right)^{+}_{p}\boldsymbol{\Sigma}^{\mathrm{T}} - \boldsymbol{\Sigma}\left(\boldsymbol{\Sigma}^{\mathrm{T}}\boldsymbol{\Sigma}\right)^{+}_{q}\boldsymbol{\Sigma}^{\mathrm{T}}\right)\\ &\quad= \boldsymbol{\Sigma}\left(\boldsymbol{\Sigma}^{\mathrm{T}}\boldsymbol{\Sigma}\right)^{+}_{m}\boldsymbol{\Sigma}^{\mathrm{T}} - \boldsymbol{\Sigma}\left(\boldsymbol{\Sigma}^{\mathrm{T}}\boldsymbol{\Sigma}\right)^{+}_{m}\boldsymbol{\Sigma}^{\mathrm{T}}\\ &\qquad+ \boldsymbol{\Sigma}\left(\boldsymbol{\Sigma}^{\mathrm{T}}\boldsymbol{\Sigma}\right)^{+}_{n}\boldsymbol{\Sigma}^{\mathrm{T}} - \boldsymbol{\Sigma}\left(\boldsymbol{\Sigma}^{\mathrm{T}}\boldsymbol{\Sigma}\right)^{+}_{n}\boldsymbol{\Sigma}^{\mathrm{T}} = \mathbf{0}\,,\end{aligned}\tag{3.53}$$

and

$$\left(\mathbb{P}^{\Lambda}_{m} - \mathbb{P}^{\Lambda}_{n}\right)\left(\mathbb{P}^{\Lambda}_{p} - \mathbb{P}^{\Lambda}_{q}\right) = \mathbf{0}\,.\tag{3.54}$$

Finally, given that $\mathbf{P}^{\Lambda H}_{n} - \mathbf{P}^{\Lambda H}_{m} = \mathbb{P}^{\Lambda}_{n} - \mathbb{P}^{\Lambda}_{m}$ and $\mathbb{P}^{\Sigma H}_{n} - \mathbb{P}^{\Sigma H}_{m} = \mathbf{P}^{\Sigma}_{n} - \mathbf{P}^{\Sigma}_{m}$ $\forall n, m$—which can be deduced from (3.39) and (3.41)—the remaining properties

$$\left(\mathbf{P}^{\Lambda H}_{m} - \mathbf{P}^{\Lambda H}_{n}\right)\left(\mathbf{P}^{\Lambda H}_{p} - \mathbf{P}^{\Lambda H}_{q}\right) = \mathbf{0}\,,\tag{3.55}$$

$$\left(\mathbb{P}^{\Sigma H}_{m} - \mathbb{P}^{\Sigma H}_{n}\right)\left(\mathbb{P}^{\Sigma H}_{p} - \mathbb{P}^{\Sigma H}_{q}\right) = \mathbf{0}\tag{3.56}$$

follow. All the properties listed above are used to build invertible transforms, similarly to what is done with their basis-based counterpart (3.17).

Generalization for Inhomogeneous Meshes

Also in this case we propose the generalized version for inhomogeneous mesh, similarly to what is done for the non-filtered counterpart, defining the normalized quasi-Helmholtz projectors

$$\tilde{\mathbf{P}}^{\Sigma} = \tilde{\mathbf{\Sigma}}\left(\tilde{\mathbf{\Sigma}}^{\mathrm{T}}\tilde{\mathbf{\Sigma}}\right)^{+}\tilde{\mathbf{\Sigma}}^{\mathrm{T}}, \tag{3.57}$$

$$\tilde{\mathbf{P}}^{\Lambda} = \tilde{\mathbf{\Lambda}}\left(\tilde{\mathbf{\Lambda}}^{\mathrm{T}}\tilde{\mathbf{\Lambda}}\right)^{+}\tilde{\mathbf{\Lambda}}^{\mathrm{T}}. \tag{3.58}$$

As it is proved in appendix A, also the complementarity property

$$\tilde{\mathbf{P}}^{\Sigma} = \mathbf{I} - \tilde{\mathbf{P}}^{\Lambda} \tag{3.59}$$

holds on simply connected geometries, while on general geometries, using the definitions (3.24) and (3.25), we define the normalized quasi-Helmholtz Laplacian filters

$$\tilde{\mathbf{P}}_{n}^{\Sigma} = \tilde{\mathbf{\Sigma}}\left(\tilde{\mathbf{\Sigma}}^{\mathrm{T}}\tilde{\mathbf{\Sigma}}\right)_{n}^{+}\tilde{\mathbf{\Sigma}}^{\mathrm{T}}, \tag{3.60}$$

$$\tilde{\mathbf{P}}_{n}^{\Lambda H} = \tilde{\mathbf{\Lambda}}\left(\tilde{\mathbf{\Lambda}}^{\mathrm{T}}\tilde{\mathbf{\Lambda}}\right)_{n}^{+}\tilde{\mathbf{\Lambda}}^{\mathrm{T}} + \mathbf{I} - \tilde{\mathbf{P}}^{\Sigma} - \tilde{\mathbf{P}}^{\Lambda}. \tag{3.61}$$

Analogously we define the normalized dual quasi-Helmholtz projectors as

$$\tilde{\mathbb{P}}^{\Lambda} = \tilde{\mathbb{\Lambda}}\left(\tilde{\mathbb{\Lambda}}^{\mathrm{T}}\tilde{\mathbb{\Lambda}}\right)^{+}\tilde{\mathbb{\Lambda}}^{\mathrm{T}}, \tag{3.62}$$

$$\tilde{\mathbb{P}}^{\Sigma} = \tilde{\mathbb{\Sigma}}\left(\tilde{\mathbb{\Sigma}}^{\mathrm{T}}\tilde{\mathbb{\Sigma}}\right)^{+}\tilde{\mathbb{\Sigma}}^{\mathrm{T}}, \tag{3.63}$$

again with the property

$$\tilde{\mathbb{P}}^{\Lambda} = \mathbf{I} - \tilde{\mathbb{P}}^{\Sigma} \tag{3.64}$$

holding on simply connected geometries (see appendix A). Finally, we define the normalized dual quasi-Helmholtz Laplacian filters

$$\tilde{\mathbb{P}}_{n}^{\Lambda} = \tilde{\mathbb{\Lambda}}\left(\tilde{\mathbb{\Lambda}}^{\mathrm{T}}\tilde{\mathbb{\Lambda}}\right)_{n}^{+}\tilde{\mathbb{\Lambda}}^{\mathrm{T}}, \tag{3.65}$$

$$\tilde{\mathbb{P}}_{n}^{\Sigma H} = \tilde{\mathbb{\Sigma}}\left(\tilde{\mathbb{\Sigma}}^{\mathrm{T}}\tilde{\mathbb{\Sigma}}\right)_{n}^{+}\tilde{\mathbb{\Sigma}}^{\mathrm{T}} + \mathbf{I} - \tilde{\mathbb{P}}^{\Lambda} - \tilde{\mathbb{P}}^{\Sigma}. \tag{3.66}$$

Since the primal and dual normalized Loop-Star bases still satisfy the orthogonality properties (3.30) and (3.31) and because of the properties (3.32)-(3.35), the same reasoning yields all counterparts of the properties (3.46)-(3.56), after replacing each matrix with its normalized ("tilde") counterpart.

3.3.3 Efficient Filtering Algorithms

The filtered Loop-Star functions as previously defined, require the usage of the SVD that requires a number of operations that scales as $\mathcal{O}(N^2)$ for sparse matrices and as $\mathcal{O}(N^3)$ for full matrices. As mentioned in section 3.1, these scalings are not compatible with the computational complexity required on fast solvers. For this reason, in this section we present some algorithms that allow to build in linear or quasi-linear complexity the filtered Loop-Star functions and of the quasi-Helmholtz Laplacian filters. The proposed approach deals with the standard $\mathbf{\Sigma}$ and $\mathbf{\Lambda}$, but, with minor modifications, similar strategies can be applied when replacing those matrices with their normalized counterparts $\tilde{\mathbf{\Sigma}}$ and $\tilde{\mathbf{\Lambda}}$. In particular, the additional products with the inverse square roots of well-conditioned Gram matrices can be obtained efficiently by using matrix function strategies [50].

Power Method Filtering

Fixing the filtering index n to a quantity that does not depend on the number of unknowns N, it is possible to use filters built with preconditioned inverse power methods [40]. This algorithm allows to get the n smallest singular values and singular vectors of sparse matrices in $\mathcal{O}(nN)$ operations. The scheme is well known in literature and their application for the filters building comes straightforwardly from their definition, but particular attention should be given in case of degenerate spectra. For these cases, similar schemes such as the subspace iteration [19] or Lanczos methods [88] can be employed, or alternatively other schemes presented in the following.

Butterworth Matrix Filters

Considering again the scenario in which the filtering index n fixed to a quantity that does not depend on the number of unknowns N, an alternative is to combine a matrix function approach with a filtering one. Given a scalar squared Butterworth filter of positive order m and cutoff parameter $x_c > 0$, described by

$$f_{m,x_c}(x) = \left(1 + (x/x_c)^m\right)^{-1}\,, \quad x \geq 0\,, \tag{3.67}$$

the spectrum of a positive semidefinite matrix $\mathbf{A} \in \mathbb{R}^{N\times N}$ composed of the set of singular values $\{\sigma_i(\mathbf{A})\}_i$ can be filtered by generalizing f_{m,x_c} to matrix arguments and applying it to $\mathbf{A}$, yielding the filtered matrix

$$\mathbf{A}_{\text{filt}} := f_{m,x_c}(\mathbf{A}) = \left(\mathbf{I} + (\mathbf{A}/x_c)^m\right)^{-1}\,, \tag{3.68}$$

with singular values $\{f_{m,x_c}(\sigma_i(\mathbf{A}))\}_i$. So, the matrix $\left(\mathbf{\Sigma}^{\mathrm{T}}\mathbf{\Sigma}\right)_n$ can be expressed as

$$\left(\mathbf{\Sigma}^{\mathrm{T}}\mathbf{\Sigma}\right)_n = \left(\mathbf{\Sigma}^{\mathrm{T}}\mathbf{\Sigma}\right) \lim_{m\to\infty} f_{m,\sigma_n(\mathbf{\Sigma}^{\mathrm{T}}\mathbf{\Sigma})}\left(\mathbf{\Sigma}^{\mathrm{T}}\mathbf{\Sigma}\right)\,. \tag{3.69}$$

However, the presence of high exponents in (3.69) may render its computation unstable. For this reason, we propose the usage of the following factorization formula that leverages the roots of unity

$$\left(\boldsymbol{\Sigma}^{\mathrm{T}}\boldsymbol{\Sigma}\right)_n = \left(\boldsymbol{\Sigma}^{\mathrm{T}}\boldsymbol{\Sigma}\right)\lim_{m\to\infty}\prod_{k=1}^{m}\left(\frac{\boldsymbol{\Sigma}^{\mathrm{T}}\boldsymbol{\Sigma}}{\sigma_n(\boldsymbol{\Sigma}^{\mathrm{T}}\boldsymbol{\Sigma})} - \mathrm{e}^{(2k+1)\mathrm{i}\pi/N}\mathbf{I}\right)^{-1} . \tag{3.70}$$

Clearly, in practice the infinite products in this expression is truncated when the desired precision is reached. Regarding the value of $\sigma_n(\boldsymbol{\Sigma}^{\mathrm{T}}\boldsymbol{\Sigma})$, an approximation can be obtained either with ad-hoc heuristics or by the approximation $\sigma_n(\boldsymbol{\Sigma}^{\mathrm{T}}\boldsymbol{\Sigma}) \approx (N_s - n)/\| \left(\boldsymbol{\Sigma}^{\mathrm{T}}\boldsymbol{\Sigma}\right)^+ \|$. Finally, when the filtering point is a constant with respect to the number of unknowns, a multigrid approach is effective in providing the inversion required by (3.70) [102].

Filter Approximation via Chebyshev Polynomials

We now propose a strategy for the scenarios where the filtering index n is proportional to the number of unknowns N (for instance, $n = N_S/2$). To avoid the computational burden previously described, we leverage the ideas of polynomial preconditioning and graph wavelets [53, 14, 47, 62] and adopt a method based on a polynomial expansion of the spectral filter. In particular, we leverage a polynomial approximation of f_{m,x_c} on the interval $[0, \sigma_{N_S}(\boldsymbol{\Sigma}^{\mathrm{T}}\boldsymbol{\Sigma})]$. The Chebyshev polynomials $\{T_n(x)\}_n$ represent a natural basis for this approximation, and we define them by the recurrence relation

$$T_n(x) = \begin{cases} 1 & \text{if } n = 0 \\ x & \text{if } n = 1 \\ 2xT_{n-1}(x) - T_{n-2}(x) & \text{otherwise.} \end{cases} \tag{3.71}$$

The approximated filtered matrix now reads

$$\left(\boldsymbol{\Sigma}^{\mathrm{T}}\boldsymbol{\Sigma}\right)_n \approx -\frac{c_0}{2}\mathbf{I} + \sum_{k=1}^{n_c} c_k T_k\left(\frac{\boldsymbol{\Sigma}^{\mathrm{T}}\boldsymbol{\Sigma}}{\sigma_n(\boldsymbol{\Sigma}^{\mathrm{T}}\boldsymbol{\Sigma})}\right) , \tag{3.72}$$

where the c_n are the expansion coefficients of $f_{m,\sigma_n(\boldsymbol{\Sigma}^{\mathrm{T}}\boldsymbol{\Sigma})}$ in the basis of the first n_c+1 Chebyshev polynomials that can be computed as proposed in [89]. The order of the polynomial required to obtain a given approximation of the Butterworth filter, does not need to be changed with increasing discretizations, because the cutoff frequency of this filter is proportional to the number of unknowns and so is the domain size. In other words, the filters obtained by following this approach require the same number of sparse matrix-vector multiplication for increasing discretization when the filtering index is proportional to the number of degrees of freedom.

3.3.4 Laplacian Filter Applied to Preconditioning

A first application case of the introduced filters is their usage in developing two families of preconditioners for the EFIE defined in (2.101). As already mentioned in section 3.2, this equation is known to suffer from both the low-frequency and dense-discretization breakdowns. Both these conditioning issues are cured by the preconditioners obtained with the filtered functions decompositions or with the quasi-Helmholtz Laplacian filters.

Note that in this Section and in the subsequent ones, we will study the singular value spectrum of potentially singular matrices. When dealing with such matrices, the condition number will be defined as $\operatorname{cond}(\mathbf{A}) = \|\mathbf{A}\|\|\mathbf{A}^{+}\|$. Moreover, inverse powers of singular matrices in the following will always denote the corresponding positive power of the pseudoinverse of the matrix.

Filtered Bases Approach

There exists in literature some preconditioning techniques for the single layer and the hypersingular operator based on primal and dual Laplacians [85, 84, 3, 87]. This means that $\mathbf{V}_{\boldsymbol{\Lambda}}$, and $\mathbf{V}_{\boldsymbol{\Sigma}}$ combined with proper diagonal preconditioning are valid bases for regularizing the vector and scalar potential parts of the EFIE and avoid the dense-discretization breakdown.

For the hypersingular operator matrix $\mathbf{T}_{\mathrm{h}}$, this results comes from the fact that an operator spectrally equivalent to the single layer can be obtained from it. In fact, noticing that $\mathbf{T}_{\mathrm{h}} = \boldsymbol{\Sigma}\mathbf{T}_{\mathrm{s}}^{\rho}\boldsymbol{\Sigma}^{\mathrm{T}}$ [113], where $\mathbf{T}_{\mathrm{s}}^{\rho}$ is the patch-function discretization of the single layer operator, i.e. $[\mathbf{T}_{\mathrm{s}}^{\rho}]_{mn} = \langle \rho_m, \mathcal{S}\rho_n \rangle$. We also define $\tilde{\mathbf{T}}_{\mathrm{s}}^{\rho} := \mathbf{G}_p^{-1/2}\mathbf{T}_{\mathrm{s}}^{\rho}\mathbf{G}_p^{-1/2}$, we obtain $\tilde{\mathbf{T}}_{\mathrm{h}} = \tilde{\boldsymbol{\Sigma}}\tilde{\mathbf{T}}_{\mathrm{s}}^{\rho}\tilde{\boldsymbol{\Sigma}}^{\mathrm{T}}$, and it follows the equivalence between $\left(\tilde{\boldsymbol{\Sigma}}^{\mathrm{T}}\tilde{\boldsymbol{\Sigma}}\right)^{+}\tilde{\boldsymbol{\Sigma}}^{\mathrm{T}}\tilde{\mathbf{T}}_{\mathrm{h}}\tilde{\boldsymbol{\Sigma}}\left(\tilde{\boldsymbol{\Sigma}}^{\mathrm{T}}\tilde{\boldsymbol{\Sigma}}\right)^{+}$ and $\tilde{\mathbf{T}}_{\mathrm{s}}^{\rho}$. We know from pseudo-differential theory that

$$\left(\tilde{\boldsymbol{\Sigma}}^{\mathrm{T}}\tilde{\boldsymbol{\Sigma}}\right)^{1/4}\tilde{\mathbf{T}}_{\mathrm{s}}^{\rho}\left(\tilde{\boldsymbol{\Sigma}}^{\mathrm{T}}\tilde{\boldsymbol{\Sigma}}\right)^{1/4} = \tilde{\mathbf{V}}_{\tilde{\boldsymbol{\Sigma}}}\left(\tilde{\mathbf{S}}_{\tilde{\boldsymbol{\Sigma}}}^{\mathrm{T}}\tilde{\mathbf{S}}_{\tilde{\boldsymbol{\Sigma}}}\right)^{1/4}\tilde{\mathbf{V}}_{\tilde{\boldsymbol{\Sigma}}}^{\mathrm{T}}\tilde{\mathbf{T}}_{\mathrm{s}}^{\rho}\tilde{\mathbf{V}}_{\tilde{\boldsymbol{\Sigma}}}\left(\tilde{\mathbf{S}}_{\tilde{\boldsymbol{\Sigma}}}^{\mathrm{T}}\tilde{\mathbf{S}}_{\tilde{\boldsymbol{\Sigma}}}\right)^{1/4}\tilde{\mathbf{V}}_{\tilde{\boldsymbol{\Sigma}}}^{\mathrm{T}}, \tag{3.73}$$

is well conditioned even for increasing discretization, as is proven in [87]. This is because $\tilde{\boldsymbol{\Sigma}}^{\mathrm{T}}\tilde{\boldsymbol{\Sigma}}$ is a valid discretization of a Laplacian matrix [13] and for $h \to 0$ we have

$$\operatorname{cond}\left(\tilde{\mathbf{V}}_{\tilde{\boldsymbol{\Sigma}}}\left(\tilde{\mathbf{S}}_{\tilde{\boldsymbol{\Sigma}}}^{\mathrm{T}}\tilde{\mathbf{S}}_{\tilde{\boldsymbol{\Sigma}}}\right)^{1/4}\tilde{\mathbf{V}}_{\tilde{\boldsymbol{\Sigma}}}^{\mathrm{T}}\left(\tilde{\boldsymbol{\Sigma}}^{\mathrm{T}}\tilde{\boldsymbol{\Sigma}}\right)^{+}\tilde{\boldsymbol{\Sigma}}^{\mathrm{T}}\tilde{\mathbf{T}}_{\mathrm{h}}\,\tilde{\boldsymbol{\Sigma}}\left(\tilde{\boldsymbol{\Sigma}}^{\mathrm{T}}\tilde{\boldsymbol{\Sigma}}\right)^{+}\tilde{\mathbf{V}}_{\tilde{\boldsymbol{\Sigma}}}\left(\tilde{\mathbf{S}}_{\tilde{\boldsymbol{\Sigma}}}^{\mathrm{T}}\tilde{\mathbf{S}}_{\tilde{\boldsymbol{\Sigma}}}\right)^{1/4}\tilde{\mathbf{V}}_{\tilde{\boldsymbol{\Sigma}}}^{\mathrm{T}}\right) = \mathcal{O}(1). \tag{3.74}$$

Since $\tilde{\mathbf{V}}_{\tilde{\boldsymbol{\Sigma}}}$ is unitary, we can simplify the previous equation and get

$$\operatorname{cond}\left(\tilde{\mathbf{V}}_{\tilde{\boldsymbol{\Sigma}}}\left(\tilde{\mathbf{S}}_{\tilde{\boldsymbol{\Sigma}}}^{\mathrm{T}}\tilde{\mathbf{S}}_{\tilde{\boldsymbol{\Sigma}}}\right)^{1/4}\tilde{\mathbf{V}}_{\tilde{\boldsymbol{\Sigma}}}^{\mathrm{T}}\left(\tilde{\boldsymbol{\Sigma}}^{\mathrm{T}}\tilde{\boldsymbol{\Sigma}}\right)^{+}\tilde{\boldsymbol{\Sigma}}^{\mathrm{T}}\tilde{\mathbf{T}}_{\mathrm{h}}\;\tilde{\boldsymbol{\Sigma}}\left(\tilde{\boldsymbol{\Sigma}}^{\mathrm{T}}\tilde{\boldsymbol{\Sigma}}\right)^{+}\tilde{\mathbf{V}}_{\tilde{\boldsymbol{\Sigma}}}\left(\tilde{\mathbf{S}}_{\tilde{\boldsymbol{\Sigma}}}^{\mathrm{T}}\tilde{\mathbf{S}}_{\tilde{\boldsymbol{\Sigma}}}\right)^{1/4}\tilde{\mathbf{V}}_{\tilde{\boldsymbol{\Sigma}}}^{\mathrm{T}}\right)= \tag{3.75}$$

$$\operatorname{cond}\left(\left(\tilde{\mathbf{S}}_{\tilde{\boldsymbol{\Sigma}}}^{\mathrm{T}}\tilde{\mathbf{S}}_{\tilde{\boldsymbol{\Sigma}}}\right)^{1/4}\tilde{\mathbf{V}}_{\tilde{\boldsymbol{\Sigma}}}^{\mathrm{T}}\left(\tilde{\boldsymbol{\Sigma}}^{\mathrm{T}}\tilde{\boldsymbol{\Sigma}}\right)^{+}\tilde{\boldsymbol{\Sigma}}^{\mathrm{T}}\tilde{\mathbf{T}}_{\mathrm{h}}\;\tilde{\boldsymbol{\Sigma}}\left(\tilde{\boldsymbol{\Sigma}}^{\mathrm{T}}\tilde{\boldsymbol{\Sigma}}\right)^{+}\tilde{\mathbf{V}}_{\tilde{\boldsymbol{\Sigma}}}\left(\tilde{\mathbf{S}}_{\tilde{\boldsymbol{\Sigma}}}^{\mathrm{T}}\tilde{\mathbf{S}}_{\tilde{\boldsymbol{\Sigma}}}\right)^{1/4}\right). \tag{3.76}$$

However, such an approach would require the computation of the matrix $\tilde{\mathbf{V}}_{\tilde{\boldsymbol{\Sigma}}}$ and $\tilde{\mathbf{S}}_{\tilde{\boldsymbol{\Sigma}}}$ which are prohibitively expensive to obtain. Fortunately, we do not need to use the entire diagonal of $\tilde{\mathbf{S}}_{\tilde{\boldsymbol{\Sigma}}}$, but it is sufficient to take a logarithmic sampling of its elements only. In mathematical terms, we define $\mathbf{D}_{\tilde{\boldsymbol{\Sigma}}}$ the vector containing the entries of the diagonal of $\tilde{\mathbf{S}}_{\tilde{\boldsymbol{\Sigma}}}^{\mathrm{T}}\tilde{\mathbf{S}}_{\tilde{\boldsymbol{\Sigma}}}$ and the block diagonal matrix

$$\tilde{\mathbf{D}}_{\tilde{\boldsymbol{\Sigma}},\alpha}=\operatorname{diag}\left(\left[\mathbf{D}_{\tilde{\boldsymbol{\Sigma}}}\right]_{N_S-N_{S,\alpha}+1}\mathbf{I}_{N_{S,\alpha}^{\mathrm{rem}}},\;\left[\mathbf{D}_{\tilde{\boldsymbol{\Sigma}}}\right]_{N_S-\frac{N_{S,\alpha}}{\alpha}+1}\mathbf{I}_{\frac{N_{S,\alpha}}{\alpha}},\ldots,\left[\mathbf{D}_{\tilde{\boldsymbol{\Sigma}}}\right]_{N_S}\mathbf{I}_1\right), \tag{3.77}$$

where $N_{S,\alpha}=\alpha^{\lfloor\log_\alpha(N_S)\rfloor}$, $N_{S,\alpha}^{\mathrm{rem}}=N_S-\left(1-N_{S,\alpha}\right)\left(1-\alpha\right)^{-1}$, and $\mathbf{I}_n$ is the identity matrix of size n. With more implementation-oriented definition, we can compute the diagonal elements of $\tilde{\mathbf{D}}_{\tilde{\boldsymbol{\Sigma}},\alpha}$ as

$$\left[\tilde{\mathbf{D}}_{\tilde{\boldsymbol{\Sigma}},\alpha}\right]_{ii}=\left[\mathbf{D}_{\tilde{\boldsymbol{\Sigma}}}\right]_{f_{\tilde{\boldsymbol{\Sigma}}}(i)}, \tag{3.78}$$

with $f_{\tilde{\boldsymbol{\Sigma}}}(i)=N_S-\alpha^{\lfloor\log_\alpha(N_S-i+1)\rfloor}+1$. Note that the construction of this matrix only requires explicit knowledge of $\log_\alpha(N_S)$ terms of $\mathbf{D}_{\tilde{\boldsymbol{\Sigma}}}$. Similarly to what happen with hierarchical strategies [6], it can be shown that for $h\to0$ we have

$$\operatorname{cond}\left(\tilde{\mathbf{D}}_{\tilde{\boldsymbol{\Sigma}},\alpha}^{1/4}\tilde{\mathbf{V}}_{\tilde{\boldsymbol{\Sigma}}}^{\mathrm{T}}\left(\tilde{\boldsymbol{\Sigma}}^{\mathrm{T}}\tilde{\boldsymbol{\Sigma}}\right)^{+}\tilde{\boldsymbol{\Sigma}}^{\mathrm{T}}\tilde{\mathbf{T}}_{\mathrm{h}}\tilde{\boldsymbol{\Sigma}}\left(\tilde{\boldsymbol{\Sigma}}^{\mathrm{T}}\tilde{\boldsymbol{\Sigma}}\right)^{+}\tilde{\mathbf{V}}_{\tilde{\boldsymbol{\Sigma}}}\tilde{\mathbf{D}}_{\tilde{\boldsymbol{\Sigma}},\alpha}^{1/4}\right)=\mathcal{O}(\alpha)=\mathcal{O}(1), \tag{3.79}$$

Because $\tilde{\mathbf{V}}_{\tilde{\boldsymbol{\Sigma}}}$ is unitary, we obtain equivalently

$$\operatorname{cond}\left(\tilde{\mathbf{V}}_{\tilde{\boldsymbol{\Sigma}}}\tilde{\mathbf{D}}_{\tilde{\boldsymbol{\Sigma}},\alpha}^{1/4}\tilde{\mathbf{V}}_{\tilde{\boldsymbol{\Sigma}}}^{\mathrm{T}}\left(\tilde{\boldsymbol{\Sigma}}^{\mathrm{T}}\tilde{\boldsymbol{\Sigma}}\right)^{+}\tilde{\boldsymbol{\Sigma}}^{\mathrm{T}}\tilde{\mathbf{T}}_{\mathrm{h}}\;\tilde{\boldsymbol{\Sigma}}\left(\tilde{\boldsymbol{\Sigma}}^{\mathrm{T}}\tilde{\boldsymbol{\Sigma}}\right)^{+}\tilde{\mathbf{V}}_{\tilde{\boldsymbol{\Sigma}}}\tilde{\mathbf{D}}_{\tilde{\boldsymbol{\Sigma}},\alpha}^{1/4}\tilde{\mathbf{V}}_{\tilde{\boldsymbol{\Sigma}}}^{\mathrm{T}}\right)=\mathcal{O}(\alpha)=\mathcal{O}(1). \tag{3.80}$$

Note that this is symmetric left and right preconditioning scheme. We now introduce an additional Laplacian in (3.74), adjusting the exponent of $\tilde{\mathbf{S}}_{\tilde{\boldsymbol{\Sigma}}}^{\mathrm{T}}\tilde{\mathbf{S}}_{\tilde{\boldsymbol{\Sigma}}}$ accordingly, so we have

$$\tilde{\boldsymbol{\Sigma}}\left(\tilde{\boldsymbol{\Sigma}}^{\mathrm{T}}\tilde{\boldsymbol{\Sigma}}\right)^{+}\tilde{\mathbf{V}}_{\tilde{\boldsymbol{\Sigma}}}\left(\tilde{\mathbf{S}}_{\tilde{\boldsymbol{\Sigma}}}^{\mathrm{T}}\tilde{\mathbf{S}}_{\tilde{\boldsymbol{\Sigma}}}\right)^{1/4}\tilde{\mathbf{V}}_{\tilde{\boldsymbol{\Sigma}}}^{\mathrm{T}}=\tilde{\boldsymbol{\Sigma}}\left(\tilde{\boldsymbol{\Sigma}}^{\mathrm{T}}\tilde{\boldsymbol{\Sigma}}\right)^{+}\left(\tilde{\boldsymbol{\Sigma}}^{\mathrm{T}}\tilde{\boldsymbol{\Sigma}}\right)\tilde{\mathbf{V}}_{\tilde{\boldsymbol{\Sigma}}}\left(\tilde{\mathbf{S}}_{\tilde{\boldsymbol{\Sigma}}}^{\mathrm{T}}\tilde{\mathbf{S}}_{\tilde{\boldsymbol{\Sigma}}}\right)^{-3/4}\tilde{\mathbf{V}}_{\tilde{\boldsymbol{\Sigma}}}^{\mathrm{T}}. \tag{3.81}$$

This allows to leverage the filtered basis presented in section 3.3.1, in particular, thanks to the properties introduced there, we have

$$\tilde{\boldsymbol{\Sigma}}\left(\tilde{\boldsymbol{\Sigma}}^{\mathrm{T}}\tilde{\boldsymbol{\Sigma}}\right)^{+}\left(\tilde{\boldsymbol{\Sigma}}^{\mathrm{T}}\tilde{\boldsymbol{\Sigma}}\right)\tilde{\mathbf{V}}_{\tilde{\boldsymbol{\Sigma}}}\tilde{\mathbf{D}}_{\tilde{\boldsymbol{\Sigma}},\alpha}^{-3/4}\tilde{\mathbf{V}}_{\tilde{\boldsymbol{\Sigma}}}^{\mathrm{T}} = \tag{3.82}$$

$$\sum_{l=2}^{N_{S,\alpha}}\left(\tilde{\boldsymbol{\Sigma}}_{\alpha^{l}-1}-\tilde{\boldsymbol{\Sigma}}_{\alpha^{l-1}-1}\right)\left[\mathbf{D}_{\tilde{\boldsymbol{\Sigma}}}\right]_{N_S-\alpha^{l-1}+1}^{-3/4}+\left(\tilde{\boldsymbol{\Sigma}}-\tilde{\boldsymbol{\Sigma}}_{\alpha^{N_{S,\alpha}}-1}\right)\left[\mathbf{D}_{\tilde{\boldsymbol{\Sigma}}}\right]_{N_S-N_{S,\alpha}+1}^{-3/4} =: \tilde{\boldsymbol{\Sigma}}_{\mathrm{p},\alpha} \tag{3.83}$$

and thus from (3.81) and (3.82) it follows that

$$\operatorname{cond}\left(\tilde{\boldsymbol{\Sigma}}_{\mathrm{p},\alpha}^{\mathrm{T}}\tilde{\mathbf{T}}_{\mathrm{h}}\tilde{\boldsymbol{\Sigma}}_{\mathrm{p},\alpha}\right) = \mathcal{O}(1)\,, h \to 0\,. \tag{3.84}$$

A similar approach can be used to precondition $\tilde{\mathbf{T}}_{\mathrm{s}}$, starting from the fact that

$$\operatorname{cond}\left(\left(\tilde{\mathbf{S}}_{\tilde{\boldsymbol{\Lambda}}}^{\mathrm{T}}\tilde{\mathbf{S}}_{\tilde{\boldsymbol{\Lambda}}}\right)^{-1/4}\tilde{\mathbf{V}}_{\tilde{\boldsymbol{\Lambda}}}^{\mathrm{T}}\tilde{\boldsymbol{\Lambda}}^{\mathrm{T}}\tilde{\mathbf{T}}_{\mathrm{s}}\tilde{\boldsymbol{\Lambda}}\tilde{\mathbf{V}}_{\tilde{\boldsymbol{\Lambda}}}\left(\tilde{\mathbf{S}}_{\tilde{\boldsymbol{\Lambda}}}^{\mathrm{T}}\tilde{\mathbf{S}}_{\tilde{\boldsymbol{\Lambda}}}\right)^{-1/4}\right) = \mathcal{O}(1) \tag{3.85}$$

and that for $h \to 0$

$$\operatorname{cond}\left(\tilde{\mathbf{V}}_{\tilde{\boldsymbol{\Lambda}}}\left(\tilde{\mathbf{S}}_{\tilde{\boldsymbol{\Lambda}}}^{\mathrm{T}}\tilde{\mathbf{S}}_{\tilde{\boldsymbol{\Lambda}}}\right)^{-1/4}\tilde{\mathbf{V}}_{\tilde{\boldsymbol{\Lambda}}}^{\mathrm{T}}\tilde{\boldsymbol{\Lambda}}^{\mathrm{T}}\tilde{\mathbf{T}}_{\mathrm{s}}\,\tilde{\boldsymbol{\Lambda}}\tilde{\mathbf{V}}_{\tilde{\boldsymbol{\Lambda}}}\left(\tilde{\mathbf{S}}_{\tilde{\boldsymbol{\Lambda}}}^{\mathrm{T}}\tilde{\mathbf{S}}_{\tilde{\boldsymbol{\Lambda}}}\right)^{-1/4}\tilde{\mathbf{V}}_{\tilde{\boldsymbol{\Lambda}}}^{\mathrm{T}}\right) = \mathcal{O}(1)\,. \tag{3.86}$$

Dually to what is done in the previous section, for $h \to 0$ we also have

$$\operatorname{cond}\left(\tilde{\boldsymbol{\Lambda}}_{\mathrm{p},\alpha}^{\mathrm{T}}\tilde{\mathbf{T}}_{\mathrm{s}}\tilde{\boldsymbol{\Lambda}}_{\mathrm{p},\alpha}\right) = \mathcal{O}(1). \tag{3.87}$$

where

$$\tilde{\boldsymbol{\Lambda}}\left(\tilde{\boldsymbol{\Lambda}}^{\mathrm{T}}\tilde{\boldsymbol{\Lambda}}\right)^{+}\left(\tilde{\boldsymbol{\Lambda}}^{\mathrm{T}}\tilde{\boldsymbol{\Lambda}}\right)\tilde{\mathbf{V}}_{\tilde{\boldsymbol{\Lambda}}}\tilde{\mathbf{D}}_{\tilde{\boldsymbol{\Lambda}},\alpha}^{-1/4}\tilde{\mathbf{V}}_{\tilde{\boldsymbol{\Lambda}}}^{\mathrm{T}} = \tag{3.88}$$

$$\sum_{l=2}^{N_{L,\alpha}}\left(\tilde{\boldsymbol{\Lambda}}_{\alpha^{l}-1}-\tilde{\boldsymbol{\Lambda}}_{\alpha^{l-1}-1}\right)\left[\mathbf{D}_{\tilde{\boldsymbol{\Lambda}}}\right]_{N_L-\alpha^{l-1}+1}^{-1/4}+\left(\tilde{\boldsymbol{\Lambda}}-\tilde{\boldsymbol{\Lambda}}_{\alpha^{N_{L,\alpha}}-1}\right)\left[\mathbf{D}_{\tilde{\boldsymbol{\Lambda}}}\right]_{N_L-N_{L,\alpha}+1}^{-1/4} =: \tilde{\boldsymbol{\Lambda}}_{\mathrm{p},\alpha}\,, \tag{3.89}$$

and

$$\tilde{\mathbf{D}}_{\tilde{\boldsymbol{\Lambda}},\alpha} = \operatorname{diag}\left(\left[\mathbf{D}_{\tilde{\boldsymbol{\Lambda}}}\right]_{N_L-N_{L,\alpha}+1}\mathbf{I}_{N_{L,\alpha}^{\mathrm{rem}}},\ \left[\mathbf{D}_{\tilde{\boldsymbol{\Lambda}}}\right]_{N_L-\frac{N_{L,\alpha}}{\alpha}+1}\mathbf{I}_{\frac{N_{L,\alpha}}{\alpha}},\dots,\left[\mathbf{D}_{\tilde{\boldsymbol{\Lambda}}}\right]_{N_L}\mathbf{I}_{1}\right)\,, \tag{3.90}$$

with $N_{L,\alpha}^{\mathrm{rem}} = N_L - \left(1 - N_{L,\alpha}\right)\left(1-\alpha\right)^{-1}$, $\mathbf{D}_{\tilde{\boldsymbol{\Lambda}}}$ the vector containing the elements of the diagonal of $\tilde{\mathbf{S}}_{\tilde{\boldsymbol{\Lambda}}}^{\mathrm{T}}\tilde{\mathbf{S}}_{\tilde{\boldsymbol{\Lambda}}}$, and $N_{L,\alpha} = \alpha^{\lfloor \log_{\alpha}(N_L)\rfloor}$.

The previous preconditioners can then be combined to obtain a complete regularization of the EFIE system, for both low-frequency and dense-discretization breakdowns, that reads

$$\tilde{\mathbf{W}}^{\mathrm{T}}\tilde{\mathbf{T}}\tilde{\mathbf{W}}\tilde{\mathbf{j}} = \tilde{\mathbf{W}}^{\mathrm{T}}\tilde{\mathbf{v}}\,, \tag{3.91}$$

where $\tilde{\mathbf{v}} = \mathbf{G}^{-1/2}\mathbf{v}$, $\mathbf{j} = \mathbf{G}^{-1/2}\tilde{\mathbf{W}}\tilde{\mathbf{j}}$, $\tilde{\mathbf{W}} = \left[\sqrt{c_{\tilde{\mathbf{\Lambda}}}}\tilde{\mathbf{\Lambda}}_{\mathrm{p},\alpha} \quad \sqrt{c_{\tilde{\mathbf{\Sigma}}}}\tilde{\mathbf{\Sigma}}_{\mathrm{p},\alpha}\right]$, $c_{\tilde{\mathbf{\Sigma}}} = \|\tilde{\mathbf{\Sigma}}_{\mathrm{p},\alpha}^{\mathrm{T}}\tilde{\mathbf{T}}_{\mathrm{h}}\tilde{\mathbf{\Sigma}}_{\mathrm{p},\alpha}\|^{-1}$, $c_{\tilde{\mathbf{\Lambda}}} = \|\tilde{\mathbf{\Lambda}}_{\mathrm{p},\alpha}^{\mathrm{T}}\tilde{\mathbf{T}}_{\mathrm{s}}\tilde{\mathbf{\Lambda}}_{\mathrm{p},\alpha}\|^{-1}$, and where we assume that the appropriate number of columns have been removed from $\tilde{\mathbf{\Sigma}}_{\mathrm{p},\alpha}$ and $\tilde{\mathbf{\Lambda}}_{\mathrm{p},\alpha}$. In particular, for a simply connected and closed scatterer, one column must be removed from each of the two, to account for the linear dependence in the underlying Loop and Star bases [108], as is done in standard Loop-Star preconditioning. Lamentably, as in the case of standard Loop-Star functions, this operations creates a small number of isolated zero singular values, that however will not impact the convergence properties of the preconditioned equation. Differently, this effect is not present in the scheme presented in the next Section.

The dense-discretization regularization effect of this preconditioner can be deduced from the previous derivations for each of the potentials [20]. The low frequency regularization, can be demonstrated following the same reasoning as for standard Loop-Star approaches [6], since the new filtered bases retain the crucial properties that made Loop-Star so adapted for low-frequency regularization in the first place—$\tilde{\mathbf{\Lambda}}_{\mathrm{p},\alpha}^{\mathrm{T}}\tilde{\mathbf{T}}_{\mathrm{h}} = \mathbf{0}$, $\tilde{\mathbf{T}}_{\mathrm{h}}\tilde{\mathbf{\Lambda}}_{\mathrm{p},\alpha} = \mathbf{0}$, and $\tilde{\mathbf{\Lambda}}_{\mathrm{p},\alpha}^{\mathrm{T}}\tilde{\mathbf{\Sigma}}_{\mathrm{p},\alpha} = \mathbf{0}$. Finally, we have

$$\operatorname{cond}\left(\tilde{\mathbf{W}}^{\mathrm{T}}\tilde{\mathbf{T}}\tilde{\mathbf{W}}\right) = \mathcal{O}(1)\,, \text{ when } h \to 0\,, k \to 0\,. \tag{3.92}$$

Quasi-Helmholtz Filters Approach

In several application scenarios, an explicit quasi-Helmholtz decomposition, such as the Loop-Star decomposition, is not necessary, and quasi-Helmholtz projectors could be used instead [6]. Similarly, instead of using filtered Loop-Star preconditioning approaches, basis-free approaches based on the quasi-Helmholtz Laplacian filters, are often more effective. In this section we explore this approach that, as an additional advantage, avoid the computational overhead of global-loop detection for multiply connected scatterers.

Similarly to what is done in the previous section, we combine a preconditioner for the solenoidal part of $\tilde{\mathbf{T}}_{\mathrm{s}}$ with a preconditioner for $\tilde{\mathbf{T}}_{\mathrm{h}}$, in order to precondition the full EFIE. The transition from the bases approach to the projector one is done by leveraging the correspondences between $\tilde{\mathbf{\Sigma}}$ and $\tilde{\mathbf{\Lambda}}$ and their respective projectors $\tilde{\mathbf{P}}^{\Sigma}$ and $\tilde{\mathbf{P}}^{\Lambda}$. In particular, because

$$\tilde{\mathbf{B}}_{\tilde{\mathbf{\Sigma}}} := \tilde{\mathbf{\Sigma}}\left(\tilde{\mathbf{\Sigma}}^{\mathrm{T}}\tilde{\mathbf{\Sigma}}\right)^{+}\left(\tilde{\mathbf{\Sigma}}^{\mathrm{T}}\tilde{\mathbf{\Sigma}}\right)\tilde{\mathbf{V}}_{\tilde{\mathbf{\Sigma}}}\tilde{\mathbf{D}}_{\tilde{\mathbf{\Sigma}},\alpha}^{-3/4}\tilde{\mathbf{V}}_{\tilde{\mathbf{\Sigma}}}^{\mathrm{T}} \tag{3.93}$$

is a valid left and right symmetric preconditioner for $\tilde{\mathbf{T}}_\mathrm{h}$, we can apply $\begin{bmatrix}\tilde{\mathbf{B}}_{\tilde{\boldsymbol{\Sigma}}} & \mathbf{0}\end{bmatrix}$ left and right to $\tilde{\mathbf{T}}_\mathrm{h}$, yielding a block diagonal matrix which, away from its large nullspace, is well conditioned. This, in turns, means that using $\begin{bmatrix}\tilde{\mathbf{C}}_{\tilde{\boldsymbol{\Sigma}}} & \mathbf{0}\end{bmatrix}$, with

$$\tilde{\mathbf{C}}_{\tilde{\boldsymbol{\Sigma}}} \coloneqq \tilde{\boldsymbol{\Sigma}}\left(\tilde{\boldsymbol{\Sigma}}^\mathrm{T}\tilde{\boldsymbol{\Sigma}}\right)^{+}\left(\tilde{\boldsymbol{\Sigma}}^\mathrm{T}\tilde{\boldsymbol{\Sigma}}\right)\tilde{\mathbf{V}}_{\tilde{\boldsymbol{\Sigma}}}\tilde{\mathbf{D}}_{\tilde{\boldsymbol{\Sigma}}}^{-5/4}\tilde{\mathbf{V}}_{\tilde{\boldsymbol{\Sigma}}}^\mathrm{T}\tilde{\mathbf{V}}_{\tilde{\boldsymbol{\Sigma}}}\tilde{\mathbf{D}}_{\tilde{\boldsymbol{\Sigma}}}^{1/2} \tag{3.94}$$

also yields a well-conditioned matrix (up to its nullspace). Finally, because multiplications by unitary matrices do not compromise conditioning properties, we can form the preconditioner

$$\tilde{\boldsymbol{\Sigma}}\left(\tilde{\boldsymbol{\Sigma}}^\mathrm{T}\tilde{\boldsymbol{\Sigma}}\right)^{+}\left(\tilde{\boldsymbol{\Sigma}}^\mathrm{T}\tilde{\boldsymbol{\Sigma}}\right)\tilde{\mathbf{V}}_{\tilde{\boldsymbol{\Sigma}}}\tilde{\mathbf{D}}_{\tilde{\boldsymbol{\Sigma}}}^{-5/4}\tilde{\mathbf{V}}_{\tilde{\boldsymbol{\Sigma}}}^\mathrm{T}\tilde{\mathbf{V}}_{\tilde{\boldsymbol{\Sigma}}}\begin{bmatrix}\tilde{\mathbf{D}}_{\tilde{\boldsymbol{\Sigma}}}^{1/2} & \mathbf{0}\end{bmatrix}\tilde{\mathbf{U}}_{\tilde{\boldsymbol{\Sigma}}}^\mathrm{T} = \tilde{\boldsymbol{\Sigma}}\left(\tilde{\boldsymbol{\Sigma}}^\mathrm{T}\tilde{\boldsymbol{\Sigma}}\right)^{+}\tilde{\mathbf{V}}_{\tilde{\boldsymbol{\Sigma}}}\tilde{\mathbf{D}}_{\tilde{\boldsymbol{\Sigma}}}^{-1/4}\tilde{\mathbf{V}}_{\tilde{\boldsymbol{\Sigma}}}^\mathrm{T}\tilde{\boldsymbol{\Sigma}}^\mathrm{T}\,. \tag{3.95}$$

This allows us to form the preconditioner $\tilde{\mathbf{Q}}^{\tilde{\boldsymbol{\Sigma}}}_{\mathrm{p},\alpha}$, of additive Schwarz type, based on quasi-Helmholtz Laplacian filters

$$\tilde{\boldsymbol{\Sigma}}\left(\tilde{\boldsymbol{\Sigma}}^\mathrm{T}\tilde{\boldsymbol{\Sigma}}\right)^{+}\tilde{\mathbf{V}}_{\tilde{\boldsymbol{\Sigma}}}\tilde{\mathbf{D}}_{\tilde{\boldsymbol{\Sigma}}}^{-1/4}\tilde{\mathbf{V}}_{\tilde{\boldsymbol{\Sigma}}}^\mathrm{T}\tilde{\boldsymbol{\Sigma}}^\mathrm{T} = \tag{3.96}$$

$$\sum_{l=2}^{N_{S,\alpha}}\left(\tilde{\mathbf{P}}^{\tilde{\boldsymbol{\Sigma}}}_{\alpha^{l}-1} - \tilde{\mathbf{P}}^{\tilde{\boldsymbol{\Sigma}}}_{\alpha^{l-1}-1}\right)\left[\mathbf{D}_{\tilde{\boldsymbol{\Sigma}}}\right]^{-1/4}_{N_S-\alpha^{l-1}+1} + \left(\tilde{\mathbf{P}}^{\tilde{\boldsymbol{\Sigma}}} - \tilde{\mathbf{P}}^{\tilde{\boldsymbol{\Sigma}}}_{\alpha^{N_{S,\alpha}}-1}\right)\left[\mathbf{D}_{\tilde{\boldsymbol{\Sigma}}}\right]^{-1/4}_{N_S-N_{S,\alpha}+1} \eqqcolon \tilde{\mathbf{Q}}^{\tilde{\boldsymbol{\Sigma}}}_{\mathrm{p},\alpha} \tag{3.97}$$

for which

$$\operatorname{cond}\left(\tilde{\mathbf{Q}}^{\tilde{\boldsymbol{\Sigma}}}_{\mathrm{p},\alpha}\tilde{\mathbf{T}}_\mathrm{h}\tilde{\mathbf{Q}}^{\tilde{\boldsymbol{\Sigma}}}_{\mathrm{p},\alpha}\right) = \mathcal{O}(1)\,, h \to 0\,. \tag{3.98}$$

Similarly, a preconditioner for the solenoidal part of $\tilde{\mathbf{T}}_\mathrm{s}$ is

$$\tilde{\mathbf{Q}}^{\tilde{\boldsymbol{\Lambda}}}_{\mathrm{p},\alpha} \coloneqq \sum_{l=2}^{N_{L,\alpha}}\left(\tilde{\mathbf{P}}^{\tilde{\boldsymbol{\Lambda}}}_{\alpha^{l}-1} - \tilde{\mathbf{P}}^{\tilde{\boldsymbol{\Lambda}}}_{\alpha^{l-1}-1}\right)\left[\mathbf{D}_{\tilde{\boldsymbol{\Lambda}}}\right]^{1/4}_{N_L-\alpha^{l-1}+1} + \left(\tilde{\mathbf{P}}^{\tilde{\boldsymbol{\Lambda}}} - \tilde{\mathbf{P}}^{\tilde{\boldsymbol{\Lambda}}}_{\alpha^{N_{L,\alpha}}-1}\right)\left[\mathbf{D}_{\tilde{\boldsymbol{\Lambda}}}\right]^{1/4}_{N_L-N_{L,\alpha}+1} \tag{3.99}$$

for which

$$\operatorname{cond}\left(\tilde{\mathbf{Q}}^{\tilde{\boldsymbol{\Lambda}}}_{\mathrm{p},\alpha}\tilde{\mathbf{T}}_\mathrm{s}\tilde{\mathbf{Q}}^{\tilde{\boldsymbol{\Lambda}}}_{\mathrm{p},\alpha}\right) = \mathcal{O}(1)\,, h \to 0\,. \tag{3.100}$$

The full EFIE preconditioner is then an appropriate linear combination of the solenoidal and non-solenoidal preconditioners above to cure also the low-frequency breakdown. In particular we define

$$\tilde{\mathbf{Q}} = \sqrt{b_{\tilde{\boldsymbol{\Lambda}}}}\tilde{\mathbf{Q}}^{\tilde{\boldsymbol{\Lambda}}}_{\mathrm{p},\alpha} + i\sqrt{b_{\tilde{\boldsymbol{\Sigma}}}}\tilde{\mathbf{Q}}^{\tilde{\boldsymbol{\Sigma}}}_{\mathrm{p},\alpha} + \sqrt{b_{\tilde{\mathbf{H}}}}\tilde{\mathbf{P}}^{H}\,, \tag{3.101}$$

where $\tilde{\mathbf{P}}^{H} = \mathbf{I} - \tilde{\mathbf{P}}^{\Sigma} - \tilde{\mathbf{P}}^{\Lambda}$ and

$$b_{\tilde{\boldsymbol{\Lambda}}} = \|\tilde{\mathbf{Q}}^{\tilde{\boldsymbol{\Lambda}}}_{\mathrm{p},\alpha}\tilde{\mathbf{T}}_\mathrm{s}\tilde{\mathbf{Q}}^{\tilde{\boldsymbol{\Lambda}}}_{\mathrm{p},\alpha}\|^{-1}\,, \tag{3.102}$$

$$b_{\tilde{\boldsymbol{\Sigma}}} = \|\tilde{\mathbf{Q}}^{\tilde{\boldsymbol{\Sigma}}}_{\mathrm{p},\alpha}\tilde{\mathbf{T}}_\mathrm{h}\tilde{\mathbf{Q}}^{\tilde{\boldsymbol{\Sigma}}}_{\mathrm{p},\alpha}\|^{-1}\,, \tag{3.103}$$

$$b_{\tilde{\mathbf{H}}} = \|\tilde{\mathbf{P}}^{\mathbf{H}}\tilde{\mathbf{T}}_\mathrm{s}\tilde{\mathbf{P}}^{H}\|^{-1}\,, \tag{3.104}$$

account for the frequency-scaling of the operators and the diameter of Γ. The preconditioned EFIE system is

$$\tilde{\mathbf{Q}}\tilde{\mathbf{T}}\tilde{\mathbf{Q}}\tilde{\mathbf{j}}_{\mathrm{qH}} = \tilde{\mathbf{Q}}\tilde{\mathbf{v}}\,, \tag{3.105}$$

with $\mathbf{j} = \mathbf{G}^{-1/2}\tilde{\mathbf{Q}}\tilde{\mathbf{j}}_{\mathrm{qH}}$.

3.3.5 Implementation Related Details and Further Improvements

The usage of the efficient filtering algorithms presented in section 3.3.3 is not sufficient to obtain a fast and efficient implementation of the proposed preconditioning scheme. A first precaution is to explicitly set to $\mathbf{0}$ all the terms of the form $\mathbf{T}_{\mathrm{h}}\mathbf{Q}^{\mathbf{\Lambda}}_{\mathrm{p},\alpha}$, $\mathbf{Q}^{\mathbf{\Lambda}}_{\mathrm{p},\alpha}\mathbf{T}_{\mathrm{h}}$, $\mathbf{P}^{H}\mathbf{T}_{\mathrm{h}}$, or $\mathbf{T}_{\mathrm{h}}\mathbf{P}^{H}$, in order to avoid numerical instabilities. In addition, further treatments on the right hand side and on the solution vector are required to ensure that the solution of the system remains accurate until arbitrarily low frequencies. These treatments are straightforward generalization of those required for standard quasi-Helmholtz preconditioning techniques that can be found in [5].

It is also possible to further lower the resulting condition number of the schemes by slightly modifying the preconditioners. In particular, the diagonal preconditioning based on the theoretical Laplacian eigenvalues can be modified using the matrices norms, resulting in the new preconditioners

$$\mathbf{Q}^{\mathbf{\Sigma}}_{\mathrm{p},\alpha} = \sum_{l=2}^{N_{S,\alpha}} \left(\mathbf{P}^{\mathbf{\Sigma}}_{\alpha^{l}-1} - \mathbf{P}^{\mathbf{\Sigma}}_{\alpha^{l-1}-1}\right) b_l + \left(\mathbf{P}^{\mathbf{\Sigma}} - \mathbf{P}^{\mathbf{\Sigma}}_{\alpha^{N_{S,\alpha}}-1}\right) b_{N_{S,\alpha}+1}\,, \tag{3.106}$$

where

$$b_l = \left\| \left(\mathbf{P}^{\mathbf{\Sigma}}_{\alpha^{l}-1} - \mathbf{P}^{\mathbf{\Sigma}}_{\alpha^{l-1}-1}\right)^{\mathrm{T}} \mathbf{T}_{\mathrm{h}} \left(\mathbf{P}^{\mathbf{\Sigma}}_{\alpha^{l}-1} - \mathbf{P}^{\mathbf{\Sigma}}_{\alpha^{l-1}-1}\right)\right\|^{-1/2} \qquad 2 \le l \le N_{S,\alpha}\,, \tag{3.107}$$

$$b_{N_{S,\alpha}+1} = \left\| \left(\mathbf{P}^{\mathbf{\Sigma}} - \mathbf{P}^{\mathbf{\Sigma}}_{\alpha^{N_{S,\alpha}}-1}\right)^{\mathrm{T}} \mathbf{T}_{\mathrm{h}} \left(\mathbf{P}^{\mathbf{\Sigma}} - \mathbf{P}^{\mathbf{\Sigma}}_{\alpha^{N_{S,\alpha}}-1}\right)\right\|^{-1/2}\,, \tag{3.108}$$

and

$$\mathbf{Q}^{\mathbf{\Lambda}}_{\mathrm{p},\alpha} = \sum_{l=2}^{N_{L,\alpha}} \left(\mathbf{P}^{\mathbf{\Lambda}}_{\alpha^{l}-1} - \mathbf{P}^{\mathbf{\Lambda}}_{\alpha^{l-1}-1}\right) d_l + \left(\mathbf{P}^{\mathbf{\Lambda}} - \mathbf{P}^{\mathbf{\Lambda}}_{\alpha^{N_{L,\alpha}}-1}\right) d_{N_{S,\alpha}+1}\,, \tag{3.109}$$

with

$$d_l = \left\| \left(\mathbf{P}^{\mathbf{\Lambda}}_{\alpha^{l}-1} - \mathbf{P}^{\mathbf{\Lambda}}_{\alpha^{l-1}-1}\right)^{\mathrm{T}} \mathbf{T}_{\mathrm{s}} \left(\mathbf{P}^{\mathbf{\Lambda}}_{\alpha^{l}-1} - \mathbf{P}^{\mathbf{\Lambda}}_{\alpha^{l-1}-1}\right)\right\|^{-1/2}\,, \qquad 2 \le l \le N_{L,\alpha}\,, \tag{3.110}$$

$$d_{N_{S,\alpha}+1} = \left\| \left(\mathbf{P}^{\mathbf{\Lambda}} - \mathbf{P}^{\mathbf{\Lambda}}_{\alpha^{N_{L,\alpha}}-1}\right)^{\mathrm{T}} \mathbf{T}_{\mathrm{s}} \left(\mathbf{P}^{\mathbf{\Lambda}} - \mathbf{P}^{\mathbf{\Lambda}}_{\alpha^{N_{L,\alpha}}-1}\right)\right\|^{-1/2}\,. \tag{3.111}$$

To avoid that the overall complexity of the algorithm increases, the values of $\{b_l\}_l$ and $\{d_l\}_l$ can be efficiently computed using, for example, power methods (in this case only to compute the norm of the matrix, and not to build a filter).

In conclusion, the overall efficient scheme can be obtained by combining the usage of Chebyshev filters to build the band-pass/high-pass filters with filtering indices that depends on N and the usage of power methods filtering or high order Butterworth matrix filters for the initial low-pass filters, where Chebyshev filters' performance can be poor. However, keeping the same truncation for the Chebyshev filters could render them less efficient in the transition region, as they decrease in efficiency away from the middle of the spectrum [62]. Fortunately, all preconditioning real case scenarios presented here, are not impacted by this fact as shown in the following section on numerical results.

3.4 Numerical Results

The following results are obtained with non-normalized matrices ($\mathbf{\Lambda}$, $\mathbf{\Sigma}$). This also highlight that in practical cases it is not necessary to use normalized matrices ($\tilde{\mathbf{\Lambda}}$, $\tilde{\mathbf{\Sigma}}$). The first set of results are obtained using filters based on SVD, focusing on the performance of the new filtering approach, leaving to the last set of results the focus on SVD-free implementation.

Figures 3.1 and 3.2 illustrate the spectral equivalence of $\mathbf{T}_\mathrm{s}$ and $\mathbf{T}_\mathrm{h}$ and appropriately scaled base obtained with the filtered Loop-Star preconditioning approach. The shown (ordered) spectra are obtained by projecting the operator matrices against the eigenvectors of the graph Laplacians. The spectrum of the not preconditioned version of $\mathbf{T}_\mathrm{s}$ and $\mathbf{T}_\mathrm{h}$ respectively show, as predicted by pseudo-differential operator theory, a trend of $\xi^{-1/2}$ and $\xi^{1/2}$, where ξ is the spectral index. Indeed, the preconditioners prove to be effective in countering this trend and thus preconditioning operators.

The capability of the filtered bases preconditioning schemes in regularizing the EFIE is shown in fig. 3.3. Here we show the condition number of the EFIE, the Loop-Star regularized EFIE and the filtered Loop-Star regularized EFIE (eq. (3.91)) for varying frequencies and discretization on the NASA almond [110]. It can be noticed that the standard Loop-Star approach regularize the low frequency conditioning breakdown, but not the dense discretization breakdowns, while the proposed approach is capable of regularizing the both.

Similarly to what is done for the filtered bases preconditioning schemes, in figs. 3.4 and 3.5 we show the spectra of the solenoidal and non-solenoidal parts of the EFIE obtained leveraging the filtered projectors schemes. Figure 3.6 shows the preconditioning performance on the overall EFIE system for a torus geometry. This also proves that the scheme can handle multiply-connected geometries.

Finally, as anticipated, we show some result obtained with SVD-free filter. In particular, fig. 3.7 shows the conditioning study of the NASA almond obtained using Chebyshev-interpolated filters (eq. (3.72)), approximating Butterworth filters of order 100 with 200 Chebyshev polynomials. The presented fast preconditioned scheme proves to be stable also for a structure such as the NASA almond.

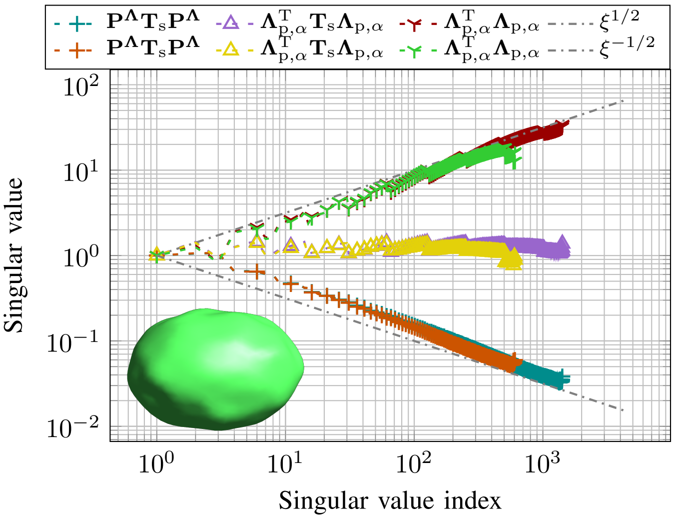

Figure 3.1: *Filtered Loop-Star preconditioning approach: Spectra (normalized so that their first singular value is one) of the solenoidal part of the vector potential, its preconditioner, and its preconditioned counterpart obtained for a smoothly-deformed sphere with a maximum diameter* 7.17 m*, frequency* 10^6 Hz*, and two different average edge lengths* h 0.31 m *and* 0.20 m*.*

3.5 Conclusions

In this chapter we introduced the main conditioning issues arising when dealing with electromagnetic integral equations and we proposed a new family of strategies for solving the low-frequency and the dense-discretization breakdowns. In addition, we also introduced the concept of fast solvers and we discussed techniques to make the new family of preconditioning strategies compatible with it. Preliminary application of frequency and h-refinement preconditioning of the EFIE has been presented and numerical results show the practical effectiveness of the newly proposed schemes.

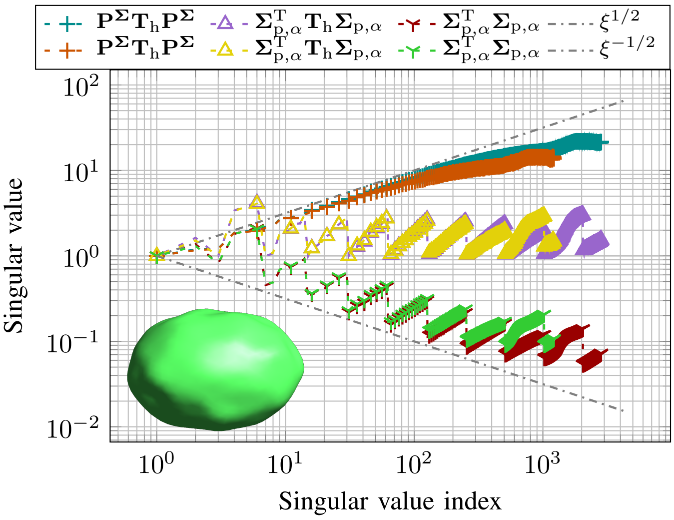

Figure 3.2: *Filtered Loop-Star preconditioning approach: Spectra (normalized so that their first singular value is one) of the non-solenoidal part of the vector potential, its preconditioner, and its preconditioned counterpart obtained for a smoothly-deformed sphere with a maximum diameter* $7.17\,\mathrm{m}$, *frequency* $10^{6}\,\mathrm{Hz}$, *and two different average edge lengths* h $0.31\,\mathrm{m}$ *and* $0.20\,\mathrm{m}$.

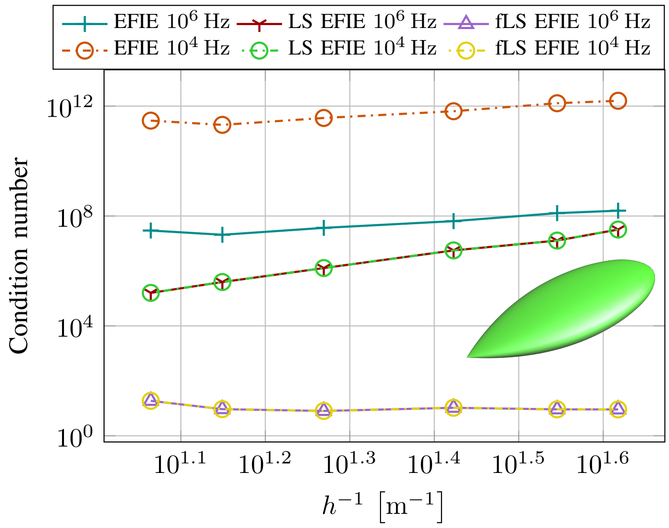

Figure 3.3: *Filtered Loop-Star preconditioning approach:Condition number (obtained after eliminating the isolated singular values by deletion of one column from each preconditioning matrices) of the EFIE eq.* (2.101), *Loop-Star EFIE, and filtered Loop-Star EFIE eq.* (3.91) *as a function of discretization for several frequencies. The simulated structure is the NASA almond re-scaled to be enclosed in a bounding box of diameter* $1.09\,\mathrm{m}$.

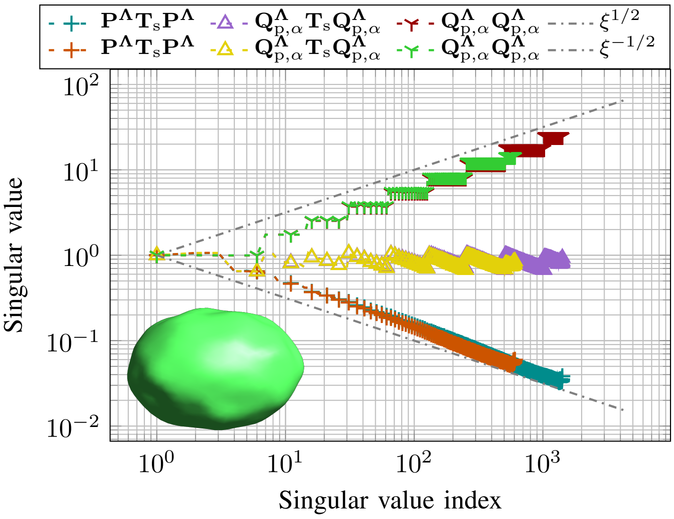

Figure 3.4: *Filtered projectors preconditioning approach: Spectra (normalized so that their first singular value is one) of the solenoidal part of the vector potential, its preconditioner, and its preconditioned counterpart obtained for a smoothly-deformed sphere with a maximum diameter* 7.17 m*, frequency* 10^6 Hz*, and two different average edge lengths* h 0.31 m *and* 0.20 m*.*

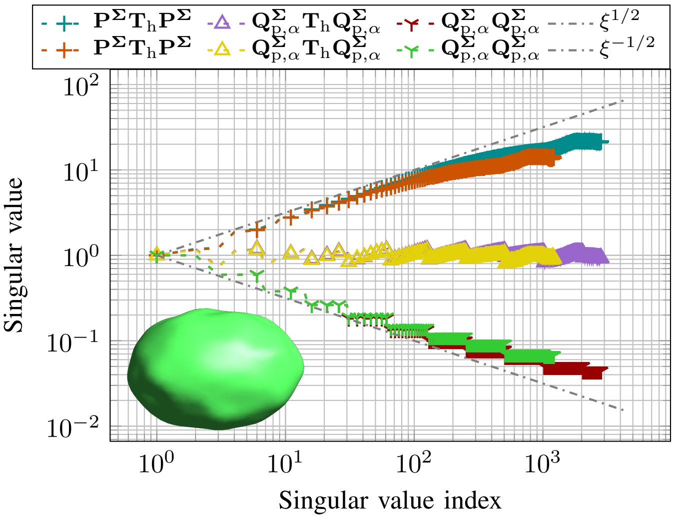

Figure 3.5: *Filtered projectors preconditioning approach: Spectra (normalized so that their first singular value is one) of the non-solenoidal part of the vector potential, its preconditioner, and its preconditioned counterpart obtained for a smoothly-deformed sphere with a maximum diameter* 7.17 m*, frequency* 10^6 Hz*, and two different average edge lengths* h 0.31 m *and* 0.20 m*.*

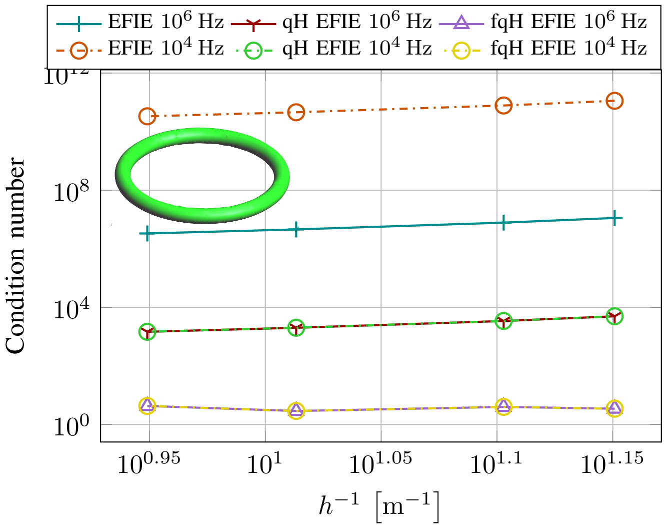

Figure 3.6: *Filtered projectors preconditioning approach: Condition number (obtained after eliminating the isolated singular values by deletion of one column from each preconditioning matrices) of the EFIE eq.* (2.101)*, quasi-Helmholtz (qH) projector EFIE, and filtered qH projector EFIE eq.* (3.105) *as a function of discretization for several frequencies. The simulated structure is a torus with inner radius* 0.9 m *and outer radius* 1.1 m*.*

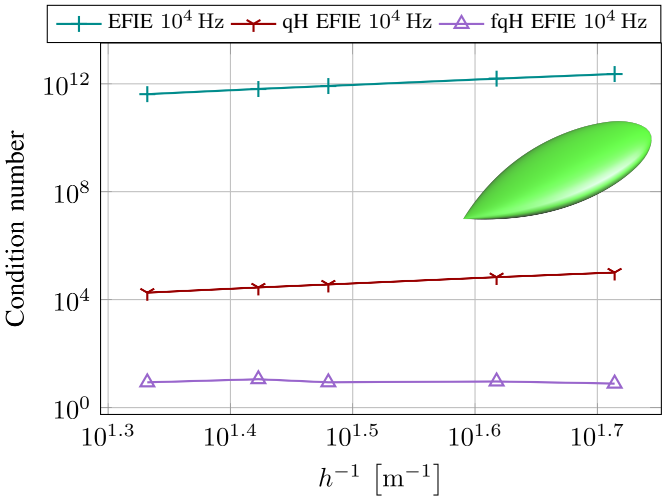

Figure 3.7: *SVD-free filtered projectors preconditioning approach: Condition number of the EFIE eq.* (2.101)*, quasi-Helmholtz (qH) projector EFIE, and filtered qH projector EFIE eq.* (3.105) *as a function of discretization. The simulated structure is the NASA almond re-scaled to be enclosed in a bounding box of diameter* 1.09 m*. The filters obtained with Chebyshev-interpolated Butterworth filters of order* 100*, expanded into* 200 *Chebyshev polynomials.*

Chapter 4

Fast Direct Solution of Electromagnetic Integral Equations

As we mentioned in chapter 3, when fast matrix-multiplication algorithms combined with preconditioning technique and iterative solvers are employed, integral equations strategies are an effective tool for solving scattering and radiation problems. However, if this approach is used when the solution for numerous RHSs is required, the repeated use of iterative solvers could lead to a high computational burden. In those scenarios, fast direct solvers (FDSs), which consist in directly building a compressed form of the inverse of the system matrix in reduced complexity, are more efficient options. Several effective strategies for direct solutions are available in literature—they often rely on hierarchical decompositions (see [2, 43, 97] and references therein)—but few of them are suitable to the high-frequency regime.

With the aim of filling this gap, in this chapter we tackle two problems. First we solve the conditioning issues appearing in the high-frequency regime that we mentioned in section 3.2, then we propose a scheme that results in a FDS suitable for this regime.

4.1 Introduction

In this section we extend the work presented in [31] to other formulations and application scenarios. First, we introduce the preconditioned equations used in the scheme, whose operators can be seen as the sum of a principal part contribution and a remainder. Peculiarly, to build our scheme, we then extract an associated circulant problem. This procedure has the advantage of automatically extracting the principal part contribution, leaving a remainder that, in case of smooth scatterers, can be compressed in favorable complexity. The resulting equation is amenable to a non-hierarchical FDS, for which a single skeleton form is required, and the solution for several RHSs can be obtained efficiently. Theoretical considerations are corroborated with numerical results, confirming and showing the practical relevance of the proposed scheme.

4.2 High Frequency Fast Direct Solver for Two-Dimensional Smooth Scatterers

The analysis is developed for 2D formulations, however, the same principles can be applied to 3D formulations.

4.2.1 Notation and Background

The 2D EFIE and MFIE modeling the electromagnetic scattering from a PEC body given a TE or a TM excitation have already been defined in section 2.4.3. As a first step to build our solver for high frequency, we define the combined field integral equation (CFIE) that, as mentioned in section 3.2.3, is a suitable solution to cure the resonances that appear in high frequency when using the standalone EFIE or MFIE, that can be observed for example in the spectrum of the MFIE, shown in fig. 4.1. The figure shows the singular values spectra of the TE-MFIE for increasing frequency calculated analytically on a circular geometry, ordered following the Fourier content of the eigenvectors of the operators (spatial frequency). In particular, the x-axis represents the spectral index of the associated eigenvalue, associating to the index 0 the highest negative spatial frequency and to the last index the highest positive spatial frequency, leaving in the middle of each curve the index associated to the constant eigenvector (null spatial frequency). The TM and TE CFIEs in 2D read respectively

$$\left(jk\mathbf{S}^k + \frac{\mathbf{G}}{2} + \mathbf{D}^{*,k}\right)\mathbf{j}_z = -\frac{1}{\eta}\mathbf{e}_z + \mathbf{h}_t, \tag{4.1}$$

$$\left(-\frac{1}{jk}\mathbf{N}^k + \frac{\mathbf{G}}{2} - \mathbf{D}^k\right)\mathbf{j}_t = -\frac{1}{\eta}\mathbf{e}_t - \mathbf{h}_z\,, \tag{4.2}$$

where the superscript ^{k} indicates the wavenumber used to compute the matrix elements (parameter relevant for the following passages). Since we choose equal balancing between the EFIE and the MFIE in our equations, we omitted the combination coefficient α that is usually present in the CFIEs definition (see for example [5, Equation 13]).

Unfortunately, in the high-frequency regime the CFIE still shows a condition number that grows with the frequency. For this reason, our solver is based on a modified version of the CFIE, introduced in the following section.

4.2.2 A Suitable Integral Equation and its Spectral Analysis

A well-conditioned and resonance-free equation is obtained by leveraging a modified version of the preconditioner proposed in [11], resulting, for the TM and TE modes respectively, in the equations

$$\left(\mathbf{N}^{\tilde{k}}\mathbf{G}^{-1}\mathbf{S}^{k}+\left(\frac{\mathbf{G}}{2}-\mathbf{D}^{*,\tilde{k}}\right)\mathbf{G}^{-1}\left(\frac{\mathbf{G}}{2}+\mathbf{D}^{*,k}\right)\right)\mathbf{j}_z=-\frac{1}{jk\eta}\mathbf{N}^{\tilde{k}}\mathbf{G}^{-1}\mathbf{e}_z+\left(\frac{\mathbf{G}}{2}-\mathbf{D}^{*,\tilde{k}}\right)\mathbf{G}^{-1}\mathbf{h}_t\,, \tag{4.3}$$

$$\left(\mathbf{S}^{\tilde{k}}\mathbf{G}^{-1}\mathbf{N}^{k}+\left(\frac{\mathbf{G}}{2}+\mathbf{D}^{\tilde{k}}\right)\mathbf{G}^{-1}\left(\frac{\mathbf{G}}{2}-\mathbf{D}^{k}\right)\right)\mathbf{j}_t=\frac{jk}{\eta}\mathbf{S}^{\tilde{k}}\mathbf{G}^{-1}\mathbf{e}_t-\left(\frac{\mathbf{G}}{2}+\mathbf{D}^{\tilde{k}}\right)\mathbf{G}^{-1}\mathbf{h}_z\,, \tag{4.4}$$

where $\tilde{k} := k - 0.4jk^{1/3}a^{-2/3}$, following [34, 20], with a being a suitable average of the radii of curvature along Γ. Figure 4.2 shows the analytical spectrum of the left hand sides (LHS) of eq. (4.4), following the same ordering previously described. In this case the spectral content of eq. (4.4) is resonance-free and it clusters, as expected, around the value 0.5. In addition, one can note that it is maximal around the surface resonant point attained when the spatial frequency equals $|ka|$. By retaining the information related to the singular vectors corresponding to this region of maximal spectral strength, and filtering out the deviation from the halved identity of the others, allows the compression of the electromagnetic operator in the high-frequency regime.

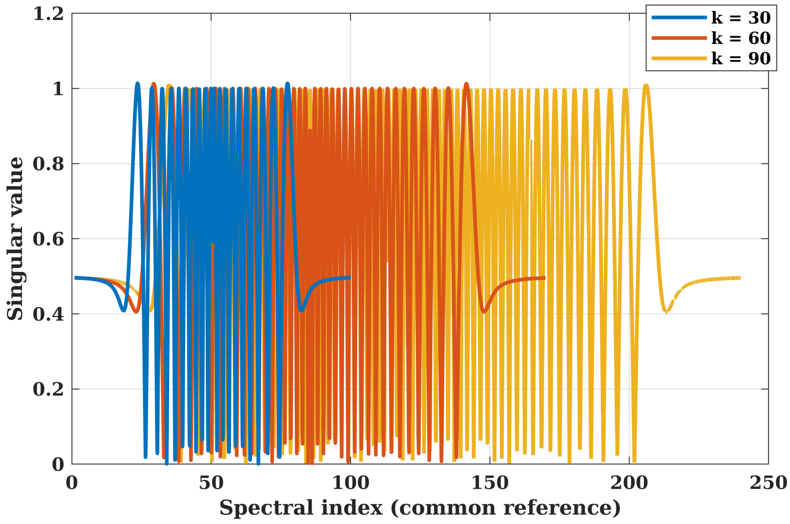

Figure 4.1: *Continuous spectrum of the 2D TE-MFIE obtained for a cylinder.*

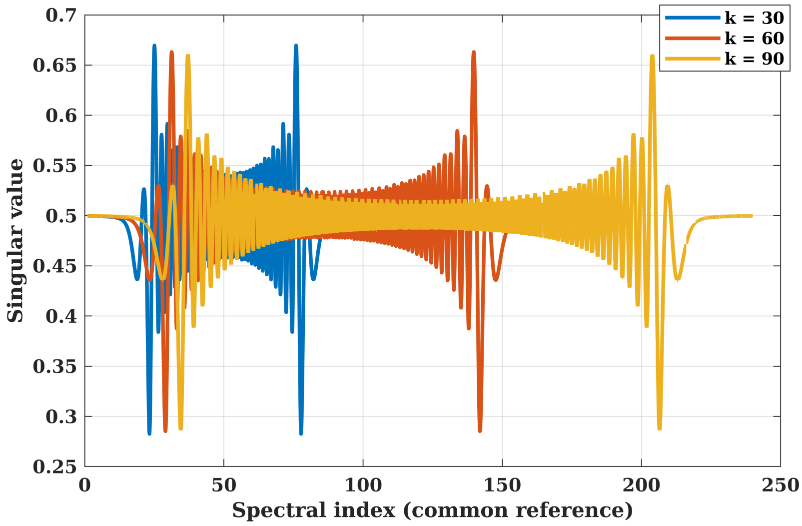

Figure 4.2: *Spectrum of the TE version of the modified Calderón CFIE used this work (continuous counterpart of* (4.4)*) obtained for a cylinder.*

4.2.3 Handling the Error on the Elliptic Spectrum

The spectra of the continuous counterparts of the LHSs of eq. (4.3) and eq. (4.4) (fig. 4.2) suggest that, by subtracting the identity $\mathsf{G}/2$ to both sides of eq. (4.3) and eq. (4.4), we can obtain operator matrices which are suitable for compression in skeleton form. Unfortunately, the discretization error in the elliptic part of the spectrum of such operators can limit the compressibility when this approach is employed. Indeed, the discretization causes a constant relative error (with respect to the identity) in the elliptic spectrum for second kind preconditioned operators, as shown in fig. 4.3. In this figure, on the y axis we show what we call ordered singular values, i.e. a form of projection of the operator matrix on the Laplacian operator of the structure.

As clearly visible from fig. 4.3, by setting a low enough threshold for the compression of such a spectrum, we would include in the skeleton many singular values in the elliptic spectrum, growing in number with frequency, leading to prohibitive computational complexity.

To overcome this problem, we adopted a different strategy that is based on subtracting an equivalent circular problem from the operators defined on γ, instead of simply subtracting the identity $\mathsf{G}/2$. More details on the implementation are given in section 4.3. The advantage is that, by extracting in this way the second kind part of the original operators, only a compact operator is left, for which the spectrum in the elliptic region is decreasing for growing spatial-frequencies. The practical impact of this strategy is evident when comparing fig. 4.3 with fig. 4.4, which represents the ordered singular values of the extracted part of eq. (4.4) resulting from the subtraction of the equivalent circulant problem. Indeed, differently from the case above, the compression threshold can be set at an arbitrarily low value without compromising the accuracy of the results and the computational complexity.

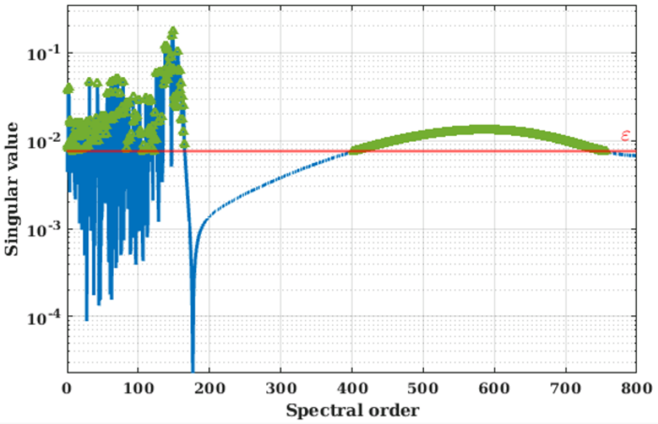

Figure 4.3: *Projected singular values of the operator on the LHS of eq.* (4.4) *after subtracting* $\mathbf{G}/2$.

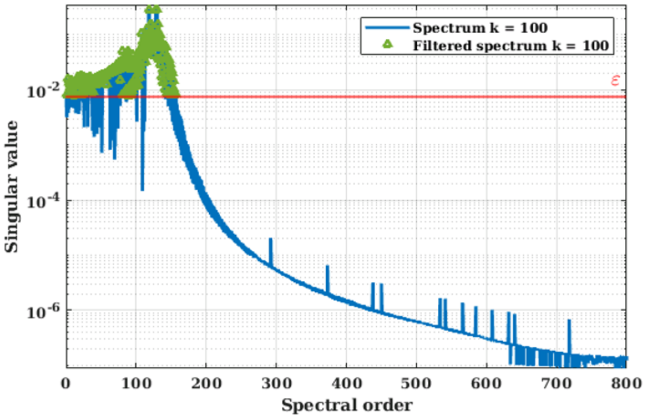

Figure 4.4: *Projected singular values of the operator on the LHS of eq.* (4.4) *after subtracting the equivalent circulant problem.*

4.3 The Direct Solver and Implementation Details

In this work the geometry is discretized with curvilinear segments that follow the boundary of the structures, of length l_Γ. Practically, cubic splines are used to describe the cells of the geometry and parameterize them with a curvilinear abscissa. Clearly, the resolution is determined by the number of points used to describe each segment (that is generally way lager then the number of basis functions used to discretize the problem). The obtained curvilinear cells are the domain of the triangular basis functions, described in section 2.4.2, used as both source and testing basis functions. Finally, we consider that the discretization will be uniform for all the geometries, so the length of each single curvilinear element will be equal to l_Γ/N.

For the implementation of the extraction based on the equivalent circulant problem, mentioned in section 4.2.3, we consider the manifold describing the boundary of the studied geometry Γ, with length l_Γ, and a circular manifold Γ_c built such that its length l_{Γ_c} equals the one of the manifold under study ($l_\Gamma = l_{\Gamma_c}$). Because of the symmetries of the circle and up to the choice of the center (irrelevant for our interest), the determination of this circular manifold is univocal.

Consider now the MoM matrices relative to any of the integral operators involved in eq. (4.3) or eq. (4.4) evaluated on the basis functions lying on Γ and Γ_c, generally denoted respectively with $\mathbf{O}$ and $\mathbf{O}_c$ (from now on, each interaction matrix relative to the circulant manifold will be distinguished by the subscript $_c$). Given these definitions, we define our extracted operator as $\mathbf{O}_e := \mathbf{O} - \mathbf{O}_c$. Note that, because of the uniformity of the discretization, we have by construction $\mathbf{G} = \mathbf{G}_c$. Moreover, we also notice that each matrix $\mathbf{O}_c$ is circulant. Finally, we specify that the matrices $\mathbf{O}_e$ are not built implicitly as subtraction between the $\mathbf{O}$ and the $\mathbf{O}_c$ contributions, but by explicit computation, i.e. the extraction is performed at the operator level by properly modifying the Green's function.

The definition of such operators is crucial for our direct solver, because they improve the compressibility of the operators on the LHS of eq. (4.3) and eq. (4.4). We define the operators

$$\mathbf{C}_{TM} := \mathbf{N}^{\tilde{k}}\mathbf{G}^{-1}\mathbf{S}^{k} + \left(\frac{\mathbf{G}}{2} - \mathbf{D}^{*,\tilde{k}}\right)\mathbf{G}^{-1}\left(\frac{\mathbf{G}}{2} + \mathbf{D}^{*,k}\right), \tag{4.5}$$

$$\mathbf{C}_{TE} := \mathbf{S}^{\tilde{k}}\mathbf{G}^{-1}\mathbf{N}^{k} + \left(\frac{\mathbf{G}}{2} + \mathbf{D}^{\tilde{k}}\right)\mathbf{G}^{-1}\left(\frac{\mathbf{G}}{2} - \mathbf{D}^{k}\right) \tag{4.6}$$

and, similarly to what was said above (and considering $\mathbf{G} = \mathbf{G}_c$ because of the uniformity of the mesh), their contributions

$$\mathbf{C}_{c,TM} := \mathbf{N}_c^{\tilde{k}}\mathbf{G}^{-1}\mathbf{S}_c^{k} + \left(\frac{\mathbf{G}}{2} - \mathbf{D}_c^{*,\tilde{k}}\right)\mathbf{G}^{-1}\left(\frac{\mathbf{G}}{2} + \mathbf{D}_c^{*,k}\right), \tag{4.7}$$

$$\mathbf{C}_{c,TE} := \mathbf{S}_c^{\tilde{k}}\mathbf{G}^{-1}\mathbf{N}_c^{k} + \left(\frac{\mathbf{G}}{2} + \mathbf{D}_c^{\tilde{k}}\right)\mathbf{G}^{-1}\left(\frac{\mathbf{G}}{2} - \mathbf{D}_c^{k}\right), \tag{4.8}$$

$$\mathbf{C}_{e,TM} := \mathbf{C}_{TM} - \mathbf{C}_{c,TM}, \tag{4.9}$$

$$\mathbf{C}_{e,TE} := \mathbf{C}_{TE} - \mathbf{C}_{c,TE}. \tag{4.10}$$

The matrices $\mathbf{C}_{e,TM}$ and $\mathbf{C}_{e,TE}$ can be generally compressed in skeleton form in favorable complexity. Indeed, differently from the matrices $\mathbf{C}_{TM} - \frac{\mathbf{G}}{2}$ and $\mathbf{C}_{TE} - \frac{\mathbf{G}}{2}$, $\mathbf{C}_{e,TM}$ and $\mathbf{C}_{e,TE}$ do not show criticalities in the elliptic region of the spectrum that limit their compressibility.

However, to achieve the coveted compressibility, particular care needs to be given in the computation of $\mathbf{C}_{e,TM}$ and $\mathbf{C}_{e,TM}$. To better understand, we expand here $\mathbf{C}_{TM}$ and $\mathbf{C}_{TE}$ in the matrix products necessary for their computation, recalling that the decomposition $\mathbf{O} = \mathbf{O}_c + \mathbf{O}_e$ holds for each operator involved, getting

$$\begin{aligned}\mathbf{C}_{TM} \coloneqq\, & \underbrace{\mathbf{N}_c^{\tilde{k}}\mathbf{G}^{-1}\mathbf{S}_c^{k}}_{\text{Circulant}} + \underbrace{\mathbf{N}_c^{\tilde{k}}\mathbf{G}^{-1}\mathbf{S}_e^{k} + \mathbf{N}_e^{\tilde{k}}\mathbf{G}^{-1}\mathbf{S}_c^{k} + \mathbf{N}_e^{\tilde{k}}\mathbf{G}^{-1}\mathbf{S}_e^{k}}_{\text{Extracted}} + \\ & \underbrace{\frac{\mathbf{G}}{4} - \frac{\mathbf{D}_c^{*,\tilde{k}}}{2} + \frac{\mathbf{D}_c^{*,k}}{2}}_{\text{Circulant}} - \underbrace{\frac{\mathbf{D}_e^{*,\tilde{k}}}{2} + \frac{\mathbf{D}_e^{*,k}}{2}}_{\text{Extracted}} - \\ & \underbrace{\mathbf{D}_c^{*,\tilde{k}}\mathbf{G}^{-1}\mathbf{D}_c^{*,k}}_{\text{Circulant}} - \underbrace{\mathbf{D}_c^{*,\tilde{k}}\mathbf{G}^{-1}\mathbf{D}_e^{*,k} - \mathbf{D}_e^{*,\tilde{k}}\mathbf{G}^{-1}\mathbf{D}_c^{*,k} - \mathbf{D}_e^{*,\tilde{k}}\mathbf{G}^{-1}\mathbf{D}_e^{*,k}}_{\text{Extracted}},\end{aligned} \tag{4.11}$$

$$\begin{aligned}\mathbf{C}_{TE} \coloneqq\, & \underbrace{\mathbf{S}_c^{\tilde{k}}\mathbf{G}^{-1}\mathbf{N}_c^{k}}_{\text{Circulant}} + \underbrace{\mathbf{S}_c^{\tilde{k}}\mathbf{G}^{-1}\mathbf{N}_e^{k} + \mathbf{S}_e^{\tilde{k}}\mathbf{G}^{-1}\mathbf{N}_c^{k} + \mathbf{S}_e^{\tilde{k}}\mathbf{G}^{-1}\mathbf{N}_e^{k}}_{\text{Extracted}} + \\ & \underbrace{\frac{\mathbf{G}}{4} + \frac{\mathbf{D}_c^{\tilde{k}}}{2} - \frac{\mathbf{D}_c^{k}}{2}}_{\text{Circulant}} + \underbrace{\frac{\mathbf{D}_e^{\tilde{k}}}{2} - \frac{\mathbf{D}_e^{k}}{2}}_{\text{Extracted}} - \\ & \underbrace{\mathbf{D}_c^{\tilde{k}}\mathbf{G}^{-1}\mathbf{D}_c^{k}}_{\text{Circulant}} - \underbrace{\mathbf{D}_c^{\tilde{k}}\mathbf{G}^{-1}\mathbf{D}_e^{k} - \mathbf{D}_e^{\tilde{k}}\mathbf{G}^{-1}\mathbf{D}_c^{k} - \mathbf{D}_e^{\tilde{k}}\mathbf{G}^{-1}\mathbf{D}_e^{k}}_{\text{Extracted}},\end{aligned} \tag{4.12}$$

where we highlighted the circulant components to be subtracted. Therefore, the circulant parts are given by

$$\begin{aligned}\mathbf{C}_{e,TM} \coloneqq\, & \underbrace{\mathbf{N}_c^{\tilde{k}}\mathbf{G}^{-1}\mathbf{S}_e^{k} + \mathbf{N}_e^{\tilde{k}}\mathbf{G}^{-1}\mathbf{S}_c^{k} + \mathbf{N}_e^{\tilde{k}}\mathbf{G}^{-1}\mathbf{S}_e^{k}}_{\text{EFIE part}} - \\ & \underbrace{\frac{\mathbf{D}_e^{*,\tilde{k}}}{2} + \frac{\mathbf{D}_e^{*,k}}{2} - \mathbf{D}_c^{*,\tilde{k}}\mathbf{G}^{-1}\mathbf{D}_e^{*,k} - \mathbf{D}_e^{*,\tilde{k}}\mathbf{G}^{-1}\mathbf{D}_c^{*,k} - \mathbf{D}_e^{*,\tilde{k}}\mathbf{G}^{-1}\mathbf{D}_e^{*,k}}_{\text{MFIE part}},\end{aligned} \tag{4.13}$$

$$\begin{aligned}\mathbf{C}_{e,TE} \coloneqq\, & \underbrace{\mathbf{S}_c^{\tilde{k}}\mathbf{G}^{-1}\mathbf{N}_e^{k} + \mathbf{S}_e^{\tilde{k}}\mathbf{G}^{-1}\mathbf{N}_c^{k} + \mathbf{S}_e^{\tilde{k}}\mathbf{G}^{-1}\mathbf{N}_e^{k}}_{\text{EFIE part}} + \\ & \underbrace{\frac{\mathbf{D}_e^{\tilde{k}}}{2} - \frac{\mathbf{D}_e^{k}}{2} - \mathbf{D}_c^{\tilde{k}}\mathbf{G}^{-1}\mathbf{D}_e^{k} - \mathbf{D}_e^{\tilde{k}}\mathbf{G}^{-1}\mathbf{D}_c^{k} - \mathbf{D}_e^{\tilde{k}}\mathbf{G}^{-1}\mathbf{D}_e^{k}}_{\text{MFIE part}}.\end{aligned} \tag{4.14}$$

We redirect to section 4.2.3 for comparison between spectral behavior $\mathbf{C}_{e,TE}$ and the one of $\mathbf{C}_{TE} - \frac{\mathbf{G}}{2}$. In addition, fig. 4.5 and fig. 4.6 show, respectively, the ordered spectra of $\mathbf{C}_{TE}$ and $\mathbf{C}_{TE}$ on an ellipse (semi-major axis 2 m and semi-minor axis 1 m) for increasing frequency. It can be noticed that, in both cases the norm of the of the operators grows only mildly, and that the singular values in the elliptic part of the spectrum of $\mathbf{C}_{e,TE}$ do not interfere in the compression of the operators, as they decay toward higher spectral indices. However, as it can be noticed in fig. 4.6, in the low spatial frequency region, we can have some singular values that have small value compared to the operator norm, but still not negligible. Since also those singular values heavily impact the compression performance of the scheme, they set a lower-bound for the achievable accuracy. Fortunately, in general cases, for higher simulation frequencies those singular values decrease in norm. Finally, because of the decrease in value with growing frequency, it could be possible to lower the compression threshold while increasing the frequency, improving the accuracy while mildly affecting the compression.

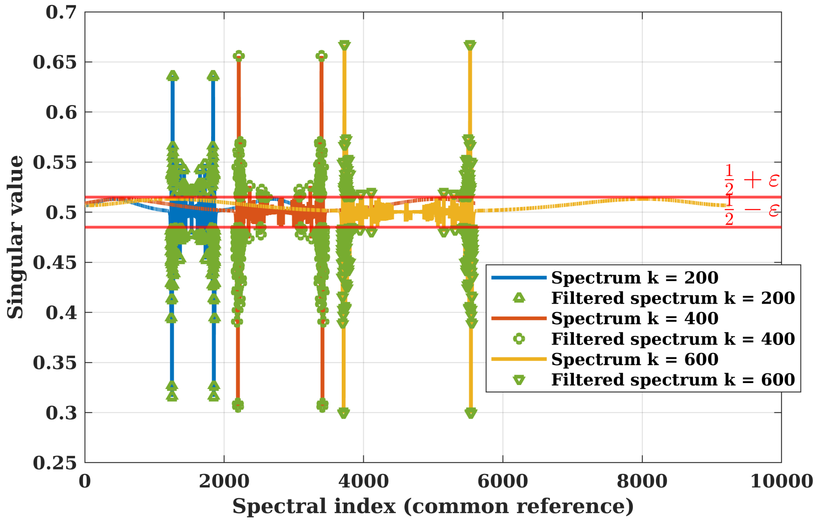

Figure 4.5: *Ordered spectrum, normalized by the inverse Gram matrix* $\mathbf{G}^{-1}$, *of the* $\mathbf{C}_{TE}$ *for increasing frequencies. The green markers indicate which singular values/singular vectors are selected by the compression scheme.*

Consequently, we can use a randomized adaptive cross approximation scheme, such as the one presented in [45, Algorithm 4.2], to compress the operator in skeleton form, resulting in

$$\mathbf{C}_{e,TM} \approx \mathbf{U}_{TM}\mathbf{V}_{TM}^{T}, \tag{4.15}$$

$$\mathbf{C}_{e,TE} \approx \mathbf{U}_{TE}\mathbf{V}_{TE}^{T}. \tag{4.16}$$

The threshold of the compression algorithm ϵ is set to guarantee the desired accuracy on the solution.

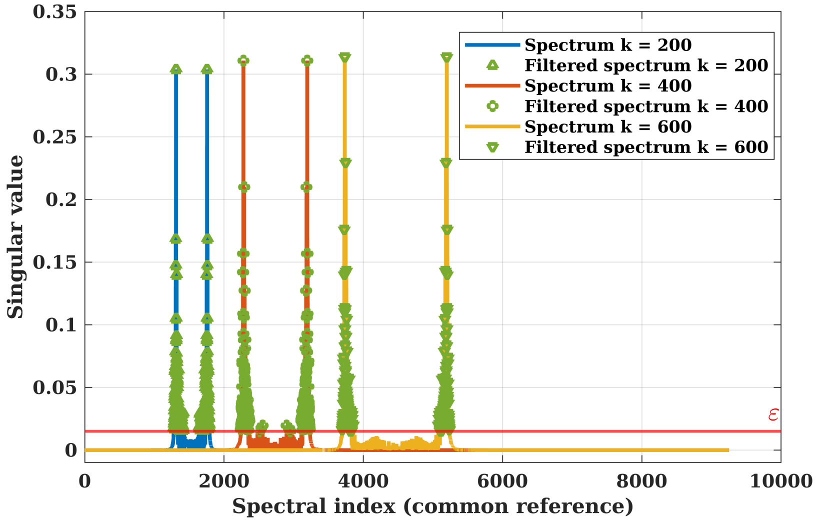

Figure 4.6: *Ordered spectrum, normalized by the inverse Gram matrix* $\mathbf{G}^{-1}$*, of the* $\mathbf{C}_{e,TE}$ *for increasing frequencies. The green markers indicate which singular values/singular vectors are selected by the compression scheme.*

Finally, by noticing that

$$\mathbf{C}_{TM} = \mathbf{C}_{c,TM}\left(\mathbf{I} + (\mathbf{C}_{c,TM})^{-1}\mathbf{U}_{TM}\mathbf{V}_{TM}^{T}\right), \tag{4.17}$$

$$\mathbf{C}_{TE} = \mathbf{C}_{c,TE}\left(\mathbf{I} + (\mathbf{C}_{c,TE})^{-1}\mathbf{U}_{TE}\mathbf{V}_{TE}^{T}\right), \tag{4.18}$$

where $\mathbf{I}$ is the identity matrix, the direct solver can be obtained by leveraging the Woodbury matrix identity [49], resulting in

$$\mathbf{C}_{TM}^{-1} = \mathbf{C}_{c,TM}^{-1} - \mathbf{C}_{c,TM}^{-1}\mathbf{U}_{TM}\left(\mathbf{I} + \mathbf{V}_{TM}^{\mathrm{T}}\mathbf{C}_{c,TM}^{-1}\mathbf{U}_{TM}\right)^{-1}\mathbf{V}_{TM}^{\mathrm{T}}\mathbf{C}_{c,TM}^{-1}, \tag{4.19}$$

$$\mathbf{C}_{TE}^{-1} = \mathbf{C}_{c,TE}^{-1} - \mathbf{C}_{c,TE}^{-1}\mathbf{U}_{TE}\left(\mathbf{I} + \mathbf{V}_{TE}^{\mathrm{T}}\mathbf{C}_{c,TE}^{-1}\mathbf{U}_{TE}\right)^{-1}\mathbf{V}_{TE}^{\mathrm{T}}\mathbf{C}_{c,TE}^{-1}. \tag{4.20}$$

Indeed, the above inverse matrices can be computed efficiently given the low-rank nature of the skeleton forms and by exploiting circulant algebra.

4.3.1 Details on Fast Implementation

To simulate electrically large structures at very high frequencies in reasonable time, we combined different strategies for the computation. As already mentioned, circulant algebra can be used to efficiently compute the inverse of the circulant matrices in eq. (4.19) and eq. (4.20) and their multiplication with a given RHS $\mathbf{b}$. In particular, in case of fast implementation, it is possible to compute the fast Fourier transform (FFT) of a row/column of the involved circulant matrix, perform an element-wise inversion to invert the operator, compute the FFT of the RHS $\mathbf{b}$, perform the element wise product between the two transformed vectors and finally compute the inverse fast Fourier transform (IFFT).

Note also that the number of such MVPs that needs to be computed in eq. (4.19) and eq. (4.20) is limited to the rank of the skeleton that, in general cases, when the operator is correctly compressed, is significantly smaller then the number of unknowns. We already mentioned the usage of [45, Algorithm 4.2] for the computation of the skeleton. However, since $\mathbf{C}_{e,TM}$ and $\mathbf{C}_{e,TE}$ involve the summation of matrices obtained by multiplying multiple operators, fast MVPs are needed to obtain the columns required by the compressing algorithm in quasi-linear complexity.

In eq. (4.13) and eq. (4.14) we can distinguish three different categories of operators involved in the formulation, that are (i) the circulant operators, (ii) the inverse Gram matrices and (iii) the extracted operators. For the first category, the fast MVP can be obtained relying on the FFT-IFFT approach just proposed. The inverse Gram matrix can be easily applied by using an iterative solver, since the matrix is sparse and well conditioned. Differently, the fast MVPs that involve extracted operators require using more complex strategies.

For this reason, we used an ad-hoc implementation of MLFMM that works with the curvilinear manifolds and is based on the circular extraction mentioned in the previous section. The computational core is based on the scheme proposed in the OpenFMM solver [39]. However, since the kernel of the extracted operators differs from the standard ones, their direct computation would require a preliminary study to obtain the plane-wave expansions necessary in the disaggregation-aggregation procedure performed for the computation of the far interactions. Fortunately, we notice that, in order to overcome the issue encountered in the elliptic part of the spectrum that limits the compressibility of the operator, mentioned in section 4.2.3, only the near interactions need to be computed by explicitly integrating the modified kernel. The far interactions, instead, can be computed implicitly by subtracting the elements of the circulant operator to the elements of the standard operator, without compromising the final compressibility. Summarizing, we have that the fast MVP of a general extracted operator $\mathbf{O}_e$ can be computed as the summation of multiple components. In terms of equation we have

$$\mathbf{O}_e = \mathbf{O}_{n,e} + \mathbf{O}_f - \mathbf{O}_{f,c} = \mathbf{O}_{n,e} + \mathbf{O}_f - \mathbf{O}_c + \mathbf{O}_{n,c}. \tag{4.21}$$

where, as before, the subscripts $_c$ and $_e$ indicate the circulant and the extracted parts of an operator, but we have in addition the subscripts $_n$ and $_f$, referring to the near and to the far interactions of an operator. By computing each extracted operator with this definition we obtain the final fast solver.

4.4 Numerical Results

Numerical results are reported both for the case where the MVP, and vector-matrix products (VMPs), are performed naively on the full matrices, and for the case where fast methods are employed. The results involves error checks only on the computation of the currents, $\mathbf{j}_z$ and $\mathbf{j}_t$, that are the solution of the linear systems. Since numerical issues of the solver would manifest during their computation, making those checks a conservative choice.

Numerical results are reported for an elliptical manifold with semi-major axis 1 m and semi-minor axis 0.5 m. To obtain the skeleton of $\mathbf{C}_{e,TM}$ and $\mathbf{C}_{e,TE}$ it the randomized compression algorithm mentioned in section 4.3 has been used. The probability coefficient hyperparameter has been set to 7.0 for all the experiments, and different relative compression thresholds are used (respectively normalized by the norm of $\mathbf{C}_{TM}$ and $\mathbf{C}_{TE}$). The computational cost is estimated in function of the wavenumber k, that for 2D structures in the high-frequency regime is in linear relationship with the number of unknowns. In the following experiments, the ratio between the wavelength λ and the discretization parameter h is kept fixed at 10. For the check of the solution error, the vectors on the RHS are computed for a plane wave excitation with polar incident angle $2/3\pi$ and amplitude 1.

Figure 4.7 and fig. 4.8 show the rank of the compressed skeleton for varying frequency and different compression thresholds, respectively for the TM and TE polarizations. For both polarizations, after a certain simulation frequency (that depends on the compression threshold), the rank shows a growth that scales as $k^{\frac{1}{3}}$ (a bound that can be theoretically predicted for the circular case). For high simulation frequencies, this provides an overall computational complexity that, when the MVP/VMP are performed naively, scales as $\mathcal{O}(k^{\frac{7}{3}})$. Figure 4.9 and fig. 4.10 show the relative error on the solution for the two polarizations. As mentioned in section 4.3, the beginning of the aimed compression regime start at higher frequencies for a lower threshold. More accurate considerations about the optimal setting of the compression threshold are left for future work. In any case, in this frequency range, the error on the solution is always inferior to the respective compression threshold, and we can even observe a decreasing trend for both polarizations.

The second set of experiments reports the performance of the solver when the fast solvers based implementation for the MVPs/VMPs is employed. The far interactions are compressed with the MLFMM implementation mentioned in section 4.3, with a compression threshold of 10^{-9}, while for the randomized compression algorithm we used a relative threshold of 0.05. Table 4.1 reports the relative errors on the solution for different frequencies and for both polarizations. It can be noticed that the error is always inferior to the compression threshold. For higher frequencies, no checks are performed on the solution error since we do not have available references that can be computed in feasible time, and we assume the correctness

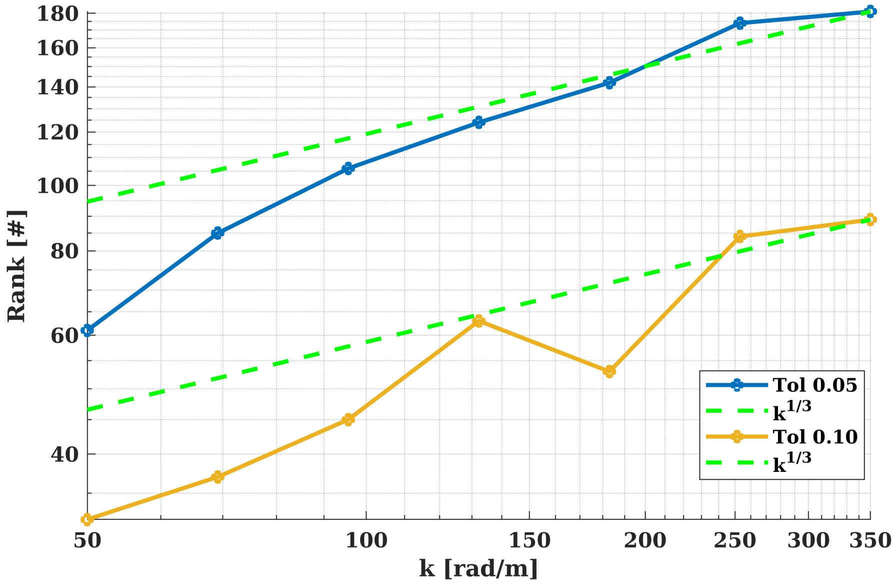

Figure 4.7: *TM formulation: check of the compression performance of the fast compression algorithm in function of k for different tolerances. Green dashed curves show the trend of* $k^{\frac{1}{3}}$.

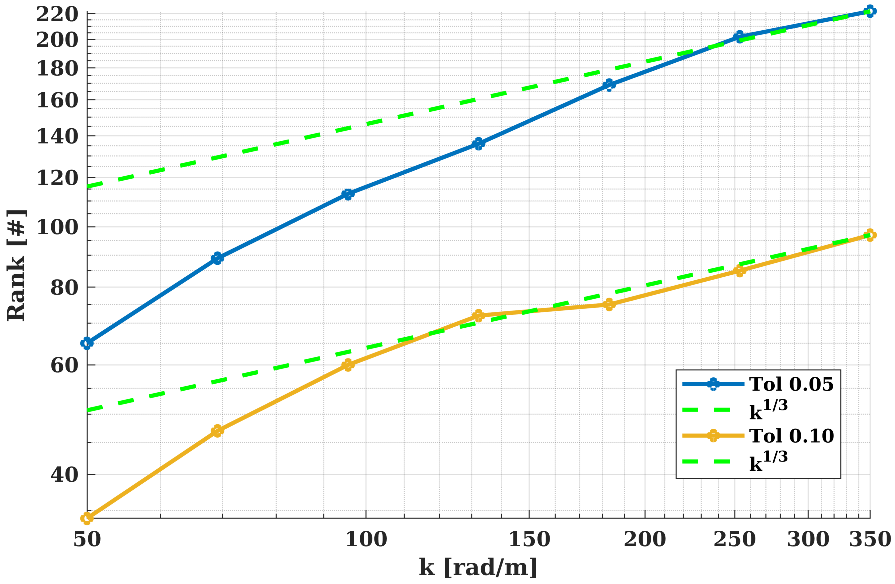

Figure 4.8: *TE formulation: check of the compression performance of the fast compression algorithm in function of k for different tolerances. Green dashed curves show the trend of* $k^{\frac{1}{3}}$.

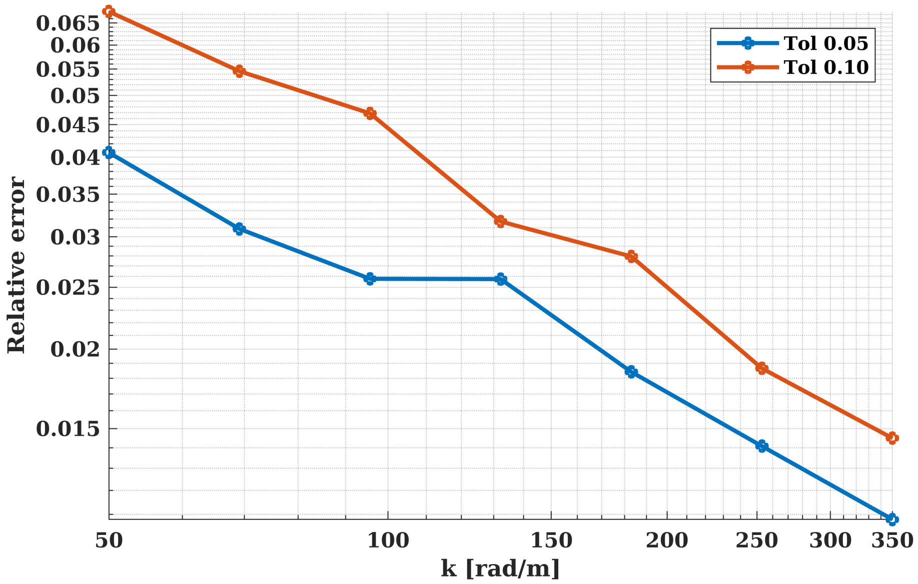

Figure 4.9: *TM formulation: check of the relative error of the fast compression algorithm in function of k for different tolerances.*

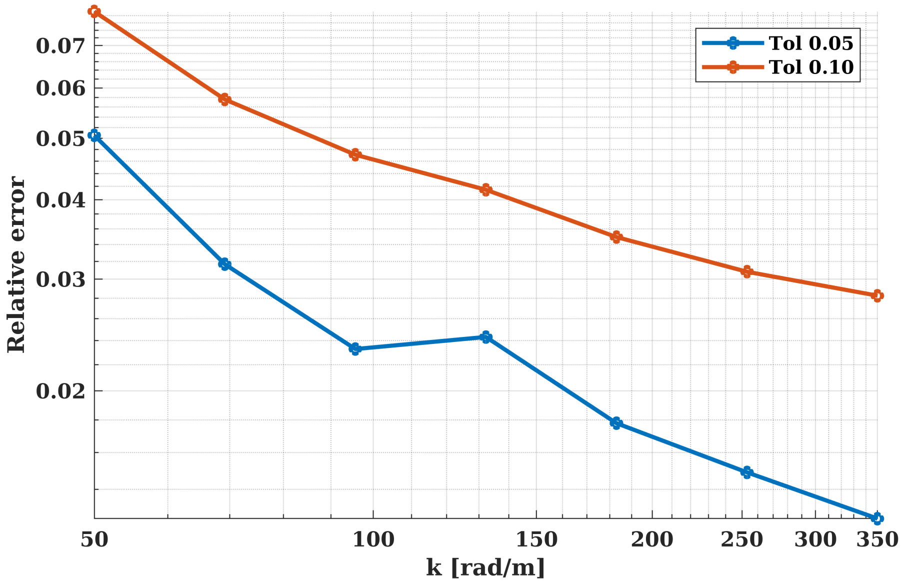

Figure 4.10: *TE formulation: check of the relative error of the fast compression algorithm in function of k for different tolerances.*

of the scheme considering its behavior at lower frequencies. The rank of the skeleton and the overall setup and compression time are reported for several simulation frequencies in fig. 4.11 and fig. 4.12, respectively (running on a single node and single thread). It can be noticed that, as expected, the rank and the timing respectively scale as $\mathcal{O}(k^{\frac{1}{3}})$ and $\mathcal{O}(k^{\frac{4}{3}})$ (a more precise estimate of the trend of the timing could also include the logarithmic factor resulting from the usage of the FFT and MLFMM).

ω $[rad/s]$	$6 \cdot 10^{10}$	$8 \cdot 10^{10}$	10^{11}
TM formulation	2.5%	2.5%	2.1%
TE formulation	2.2%	2.2%	2.0%

Table 4.1: *Relative error on the solution of the fast implementation of the direct solver against the non compressed formulation for different simulation frequencies.*

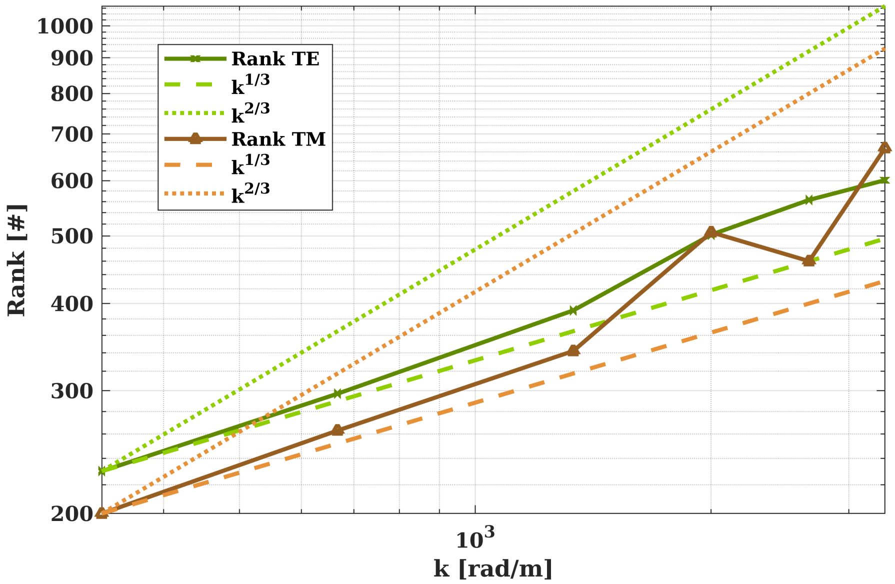

Figure 4.11: *Rank of the compressed skeletons of the fast direct solver in function of k for TM and TE formulations.*

4.5 Conclusion

Summarizing, we presented a new scheme for solving a electromagnetic integral equations at high frequency in a fast and direct way. The solver relies on a formulation that is well conditioned and stable in many applications scenarios, specially at very high frequency, where, combined with the usage of fast methods, can retrieve

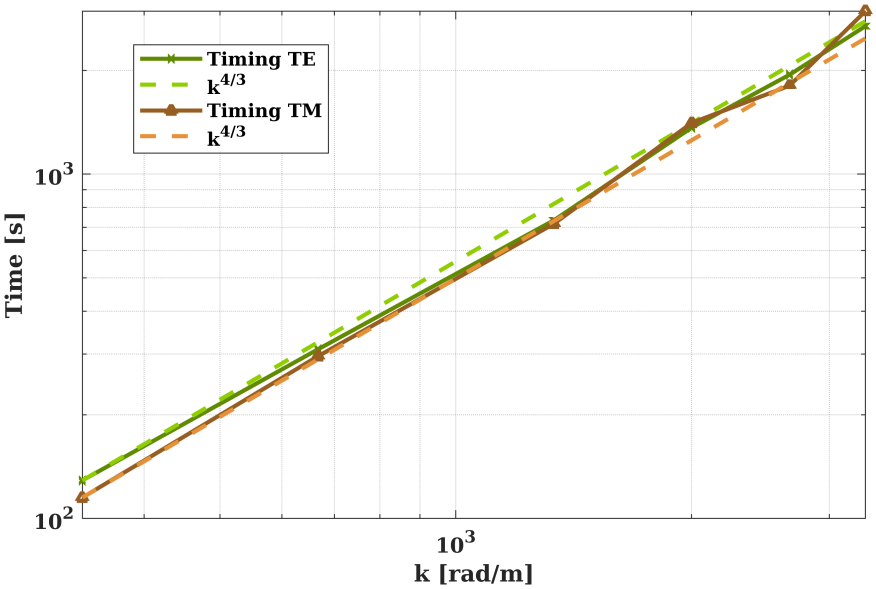

Figure 4.12: *Total set-up and computation time of the fast direct solver in function of k for TM and TE formulations.*

the direct solution of the problem with a computational complexity that scale as $\mathcal{O}(N^{\frac{4}{3}})$.

Chapter 5

Brain-Computer Interfaces and Brain Modeling Techniques

In this chapter we present some application scenarios where our solver can be applied. In particular, we focus on biomedical applications related to the brain. The chapter starts with an introduction to brain-computer interfaces (BCIs), then we present our recent contributions regarding a new BCI paradigm [82]. The application of the new paradigm shows encouraging results that have been presented at a conference of the reference community. Further publications with new results are work-in-progress and this chapter summarizes what has been achieved so far. Finally, we show the role of numerical methods for this application and in brain source imaging.

5.1 Introduction on Brain-Computer Interfaces

Brain-computer interfaces are systems that allow to control an external device through the neural activity, creating new non-muscular channels to transmit the person's intentions [86]. Their relevance crosses different clinical fields, from performance enhancements, to life quality improvement for patients suffering from motor impairments (e.g. like amyotrophic lateral sclerosis , paralysis, locked-in syndrome or brain stem stroke) [59]. Summarizing, in a BCI setting we have a subject performing a task among the ones in a predefined set, the brain activity of the subject generates an electrical signal that is monitored, processed and classified to predict which task the subject is executing. The result of the prediction(s) is used to drive the interface, that could be either purely software or, in some cases, electromechanical. The block scheme of a BCI is shown in fig. 5.1.

Among the existing recording (or monitoring) techniques used in BCIs, the electroencephalography (EEG) is the most widely adopted both in research and in commercial applications. EEG measures the electric potential related to the subject's brain activity through a set of electrodes placed on its scalp. It is a non invasive technique, characterized by great temporal resolution but, unfortunately, by poor spatial resolution when compared to other approaches. The main EEG signals, related to specific brain behaviors, that are commonly used in BCIs are: slow cortical potentials, P300 evoked potentials, sensory motor rhythms, and steady-state visually evoked potentials (SSVEPs) [109]. In particular, SSVEPs have gained attention in BCI studies, by virtue of the high information transfer rate, the minimal training required and the significant robustness of the paradigm [25, 26, 103]. The SSVEPs are defined as brain activity modulations occurring in the occipital area of the brain after repetitive visual stimuli, such as a pattern-changing checkerboard or a light flashing [33], usually in the frequency range 5-15 Hz, which result in peaks in the power spectral density (PSD) of the EEG acquisitions, both at the frequency of the stimulus and at its higher order harmonics. The pipeline setting requires a set of patterns flickering at different frequencies to be presented to the user. The objective of the subject driving the interface is to focus and fixate the gaze on only one of them, then a PSD analysis can discriminate among the panels and find the selected one.

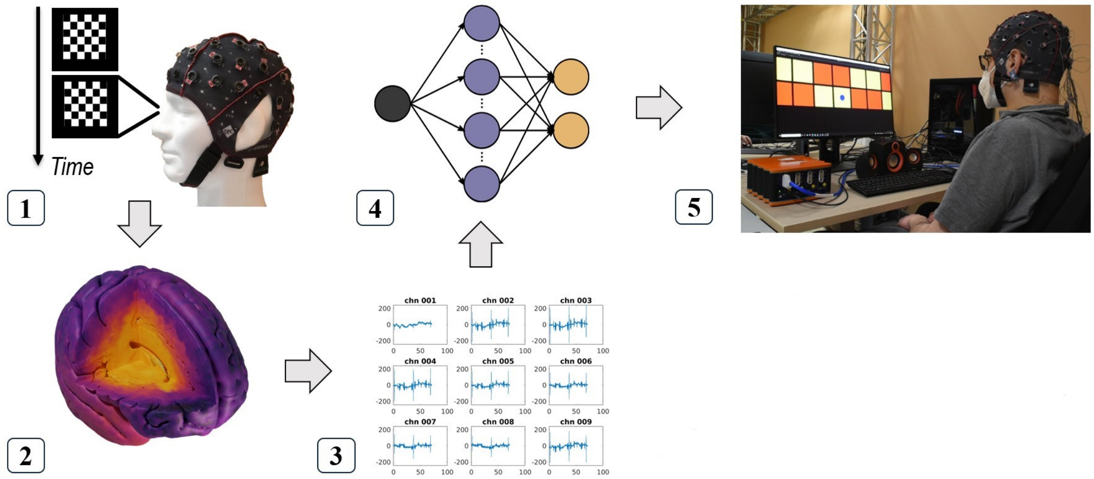

__Figure 5.1:__ A general BCI pipeline: (1) a subject perform a task among the ones of a predetermined set; (2) a characteristic electric activity associated to the task is generated in the subject's brain; (3) the electric brain activity is recorded with monitoring techniques; (4) the recorded signals are processed and used as feature to feed a classifier; (5) the predicted labels is used to control an interface.

5.2 A New BCI Paradigm Based on Visual Imagery Signals

A full SSVEP-BCI pipeline has been set-up in the CERL@Polito laboratory in Turin. Unfortunately, the SSVEP-BCIs come with some drawbacks. Eye-gazing a target might be unsuitable for patients with degraded vision or severely impaired motor conditions. Furthermore, the continuous flashing at the eyes might become annoying and stressful for the user, in addition to cause eye fatigue. For those reasons, we developed an alternative and innovative BCI paradigm that could overcome the limits of SSVEPs, based on visual imagery (VI), which may be defined as the representation of information related to perception in absence of retinal inputs [54]. This concept collides with the usual visual perception (VP) notion, which on the contrary is associated with the achievement of visual information through the eyes [57].

5.2.1 Visual Imagery Signals

The origin and the regions of activation of VI signals are still a subject of debate, as it can be evidenced among previous literature works [38, 60, 72]. Many studies demonstrated that the occipital region is suitable to acquire VP signals, and several research groups investigated if there is an activation of the same regions during VI. However, until now, there are not evident proofs of this, and there is also the possibility that only memory-associated areas are actually implied, excluding the involvement of the occipital area, as Roland and Gulyás stated [93]. During imagination, an important part of the VP hierarchy is missing, that is the acquisition through the eyes, resulting, perhaps, in different stimulation of the visual cortex. Studies based on fMRI demonstrated that during VI tasks, an activation of the calcarine region could be observed [60]. Furthermore, Sabbah et al. experimented a condition derived from the observation and the consequent visual recall of a flashing light, evidencing not only an activation of the occipital zone, but also of other parts of the brain implied in visual perception, that Sabbah et al. described as extrastriate visual areas [95]. However, other groups did not observe a clear activation of the occipital region [57], while some others highlighted the involvement of frontal and parietal networks during VI tasks [56]. De Borst et al. in 2012 determined that the frontal area would have a critical role while performing visual imagery, connecting to parietal and occipital regions, reflecting retrieval and integration of the information [35]. This was confirmed by other research groups, which defined the frontal and parietal networks (mainly on the right) as the principal activation zones during visual imagery [15, 99].

Recently, EEG BCIs based on visual imagery were proposed. For instance, Azmy et al. detected brain activation signals that could be provided to a BCI system to control a robot. They reported that the optimal location was given by

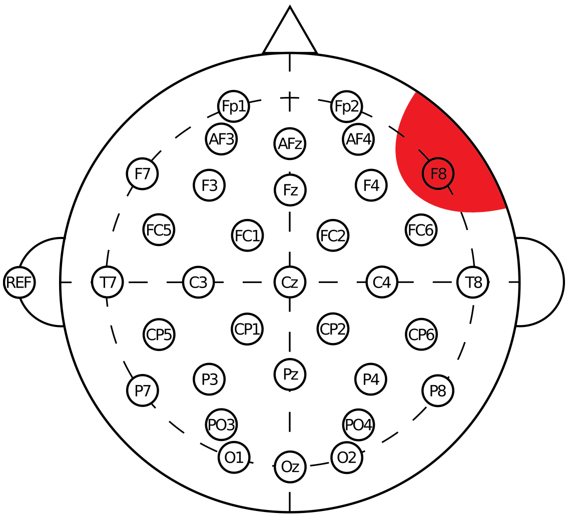

Figure 5.2: *Brain model showing the main region of interest (right-frontal area, F8) useful to control BCIs based on visual imagery, according to Azmy et al. [15].*

position F8, as shown in fig. 5.2 [15]. Moreover, Sousa et al. stated that EEG-recorded visual motion imagery signals are usable to drive multi-class BCIs, as a consequence of frontal α band power changes [101]. In 2018 Kosmyna et al. made a group of participants observe a visual cue, asking them to imagine it, obtaining classification accuracy above 70% both between VI and rest and between VI and visual observation, by virtue of VI related α band power alterations [56]. Finally, in 2019 Lee et al. obtained a robust classification of 13 classes (12 words/images and rest) of both visual imagery and imagined speech, with a precision of 26.7% [61].

In this work, we propose a new scheme for the acquisition and classification of VI signals deriving from visual imagination of flickering patterns. In particular, we examined whether mental reproductions of flashing images could provide frequency-specific power increases in PSD analyses, similar to those experienced with SSVEPs, thus making the continuous gaze of a screen unnecessary. Moreover, such implementation might grant the users the capability of switching the BCI off and on at will, addressing the issue of BCIs relying on external stimuli.

5.2.2 Experiments Setup

In order to accomplish the training of the subjects, we realized three experimental protocols. These protocols, explained in details in following sections, allowed to obtain both the visualization and the classification of SSVEP, rest and VI EEG signals. This study included 5 participants between 23 and 27 years old (all males, mean age 25 years old), without any disabilities proclaimed. All the participants were part of our research group, and all the subjects were new to EEG recordings. Preliminary experiments were conducted only on one subject (*Subject 1*), so as to test the feasibility of the paradigm.

The experimental setting for this study consisted of a workstation (with Intel Core i9 9700K @ 3.60GHz CPU, a Nvidia GeForce RTX 2080Ti GPU and 64 GB RAM), a g.HIamp EEG amplifier (256 channels, FDA and CE approved), a g.Nautilus EEG cap (g.GAMMAcap[2]), 16 active electrodes, a 64-channel driver box, a monitor showing from one to two checkerboards flickering at controllable frequencies, and three speakers allowing the reproduction of auditory stimuli.

Many previous studies in literature showed reliable SSVEP-signal EEG recordings with the electrodes mainly located in the occipital and parietal area, most commonly in Oz, O1, O2, PO3, PO4, PO7, PO8 and Pz, following the International $10-20$ system [112, 42, 71]. Regarding VI, the principal locations found were: AF4, F4, F8, O1, O2, Pz, P3, P4, Fz, Cz, Oz, T7, T8, P7 and P8 [15, 56, 61, 72]. Considering that, as stated in section 5.2.1, the exact position of VI-elicited brain activation is still uncertain, all the electrodes previously mentioned were taken into consideration for acquisitions. Figure 5.3 displays the setup adopted. The reference electrode was placed on the left earlobe, and the ground electrode was located in AFz.

As software, different tools are used, in particular Simulink, Matlab, Unity and SimBCI, an object-oriented open source MATLAB framework that can be used to generate simulated BCI data to test and debug BCI signal processing and classification approaches [65]. Our BCI pipeline was divided in three main components, that will be presented in following sections.

5.2.3 The Protocol

The sampling rate was set to 256 Hz for all the acquisitions. The frequencies used are in the low and medium frequency range (LF, MF respectively), in the range 5 and 12 Hz [73]. In particular, we use the frequencies 5 and 7 Hz, for all the protocols developed proposed in this work. These frequencies were chosen because they were considered sufficiently distant from each other to be correctly classified, and at the same time adequately low to be imagined by the subjects. In the first protocol, experiments are conducted using one single frequency at a time (either 5 or 7 Hz), concurrently classifying VI trials with SSVEP and rest trials. As previously mentioned, in VI trials the user has to imagine SSVEP-elicited visual stimuli. For this reason, SSVEP trials are also part of the training protocol, in order to introduce the user to the task it needs to imagine.

The first protocol involves tests performed with a single (slower) frequency. In its first two steps (1.*a* and 1.*b* in the list below), an additional support is supplied to the subject: the learning process is improved through the inclusion of auditory co-stimuli during VI trials, beeping at the same frequency chosen for the VI task

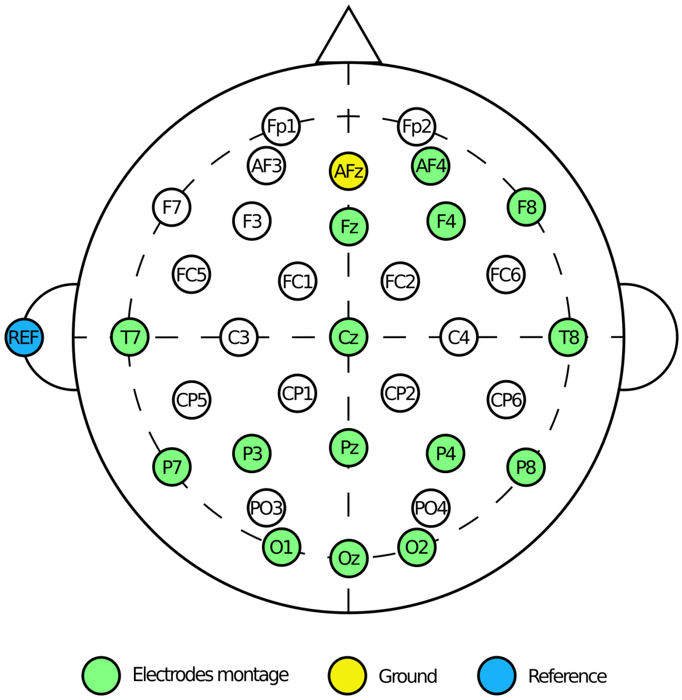

Figure 5.3: *Electrode positioning on the EEG cap, using the international* $10-20$ *system. Our signal acquisition electrodes are indicated in green, while yellow and blue indicate the the ground and reference electrodes, respectively.*

[81]. Then, once the users feel more confident with VI, these acoustic co-stimuli are removed (experiments from $1.c$ to $3.a$). In the second protocol, experiments involve two different frequencies at a time (5 and 7 Hz), with the concurrent classification of both SSVEP, VI and rest trials. The imagination exercise requested to the user is the same as in the first protocol, but without auditory co-stimuli. In the third and last protocol, experiments involve again two different frequencies at a time (5 and 7 Hz). However, in this case SSVEP-related trials are not included, as well as auditory co-stimuli, resulting in a sessions with concurrent classification of VI and rest trials only.

The aforementioned protocols are summarized in the list below. The first three numbers of the passages respectively stand for the trial duration (in seconds), the number of repetitions of the trials, and the amount of different classes involved per session.

1. **Single frequency concurrent VI and SSVEP** – Concurrent classification of SSVEP, VI, and rest at one single frequency
    (a) $6s \times 15 \times 3$ at 5 Hz, with SSVEP, VI, rest, with auditory co-stimuli during VI trials;

   (b) $6s \times 15 \times 3$ at 7 Hz, with SSVEP, VI, rest, with auditory co-stimuli during VI trials;
   (c) $6s \times 15 \times 3$ at 5 Hz, with SSVEP, VI, rest;
   (d) $6s \times 15 \times 3$ at 7 Hz, with SSVEP, VI, rest;

2. **Multiple frequencies concurrent VI and SSVEP** – Concurrent classification of SSVEP, VI and rest at two frequencies

   (a) $6s \times 18 \times 5$, with 5 Hz on the left side of the monitor and 7 Hz on the right side (for SSVEPs only), including SSVEP, VI, and rest;

3. **Multiple frequencies VI only** – Concurrent classification of VI and rest classes at two frequencies

   (a) $9s \times 20 \times 3$, with 5 Hz and 7 Hz, including only VI and rest trials;

On each experiment, a buzzer notifies the beginning of the successive trial 200 ms before the end of the previous one. The total time required for a single repetition of all the tests is 36 minutes, without considering any pauses. In most cases, with the purpose of recording more data to analyze and for better training the participants, this protocols are repeated multiple times. Figure 5.4 shows the patterns that are shown to the user during the SSVEP experiments. The graphic interface is implemented inside the Unity framework. During single frequencies SSVEP trials (protocols from $1.a$ to $1.d$), a single checkerboard flickering at the desired frequency is shown to the user (fig. 5.4.a). With the inclusion of two frequencies in the same trial, a second checkerboard is added to the Unity scene, providing an arrow which indicates where the subject has to focus his gaze (fig. 5.4.d, protocol $2.a$). Similarly, the subject can perform VI using a completely black screen (fig. 5.4.b shows a green checkerboard only for visualization purposes). With the same arrow system described above, the user can perform VI even inserting two frequencies at a time, choosing the frequency to focus at depending on the arrow orientation. The rest condition is distinguished from VI trials through the insertion of a blue rectangle (fig. 5.4.c), for all protocols.

5.2.4 The BCI Pipeline

During off-line experiments, the data acquired with EEG is collected and divided in two sets, one for the training and one for the testing. As explained more in details in the following, a part of the training set is used as validation set to determine which electrode channels to use for each experiment.

The processing and the classification are implemented in MATLAB and in particular inside the SimBCI environment [65], a software framework that allows to develop and simulate BCIs pipelines. A pre-processing of the data is performed, in

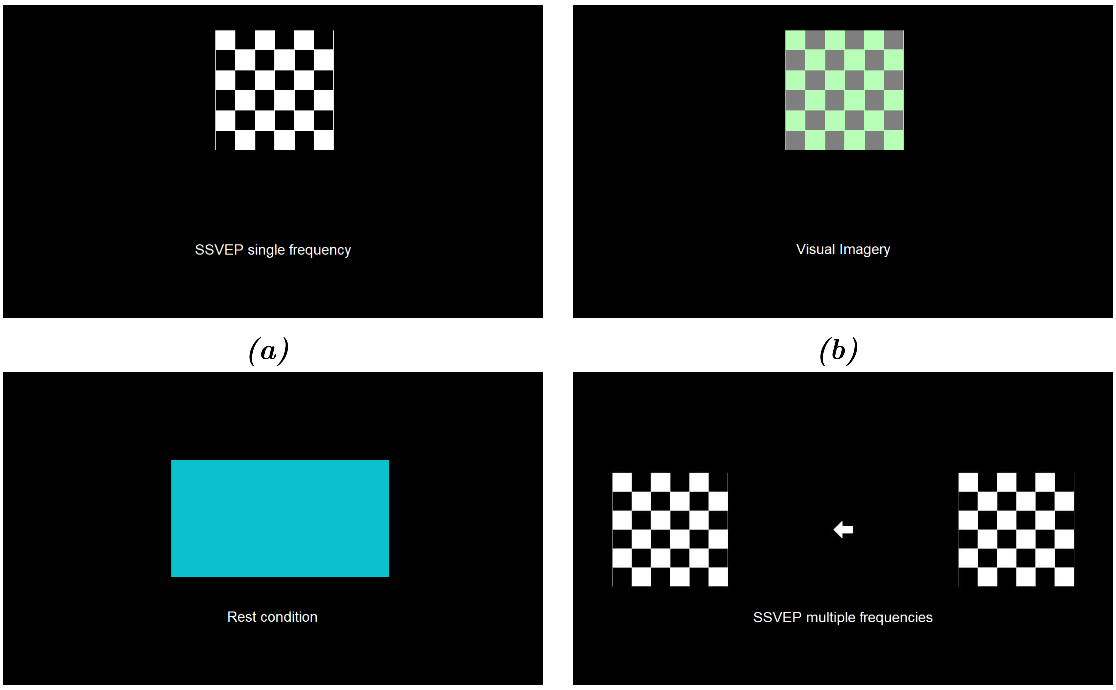

(a) *(b)* *(c)* *(d)*

Figure 5.4: *(a) Checkerboard used for SSVEP signals. (b) Visual Imagery state (green checkerboard present only for graphic purposes). (c) Rest condition. (d) Setup for two frequencies at the same time for SSVEP signals.*

order to achieve a sufficient signal-to-noise ratio (SNR), applying two filters to all the acquisitions: a 60 Hz low-pass filter for electromyography and high frequency noise attenuation, and a 48–52 Hz notch filter for the line noise rejection. In addition, a 8$^{\text{th}}$ order Butterworth with band-pass frequencies in the range 2–36 Hz filter is also applied. Then, the collected raw data is cropped into windows of 4 seconds for each trial, keeping seconds from 2 to 6 for the first two protocols and seconds from 3 to 7 for the third protocol. For each electrode and each windowed trial, PSDs estimations is performed, obtaining, for each trial-electrode combination, a vector containing the average power spectral density, with content in frequency ranging 2–36 Hz. These data vectors are therefore used as input features for the classifier [67]. For all the experiments, the classification is performed via a regularized multi-class support vector machine (SVM) classifier [68], using a linear kernel and based a multiple One-vs-All implementation [23]. The classifier has the role of predicting the labels associated with a certain task performed from a user.

The whole pipeline includes two hyper-parameters to be set. The first one, as anticipated, is the set of electrodes to be used for the classification. The second one is the C-regularization parameter of the SVM classifier. We decided to keep those hyper-parameters because, as explained in the introduction to VI signals, the literature does not yet agree on a precise location of VI-related EEG activity, and also we noticed that for each subject/experiment the classification accuracy is particularly sensible to the value of the regularization parameter. To determine those hyper-parameters, we implemented a heuristic algorithm that by using a part of the training set as a validation set iteratively adds or removes an electrode from the final set, or tune more and more finely the C-parameter.

Finally, the processing and classification parts of the pipeline are coupled with interactive interface implemented within the Simulink and Unity environments. In particular, the two environments communicate to each other via transmission control protocol (TCP), and Simulink, being part of the Mathworks suite that includes MATLAB as well, communicates with SimBCI. The Simulink part of the interface is shown in fig. 5.5.

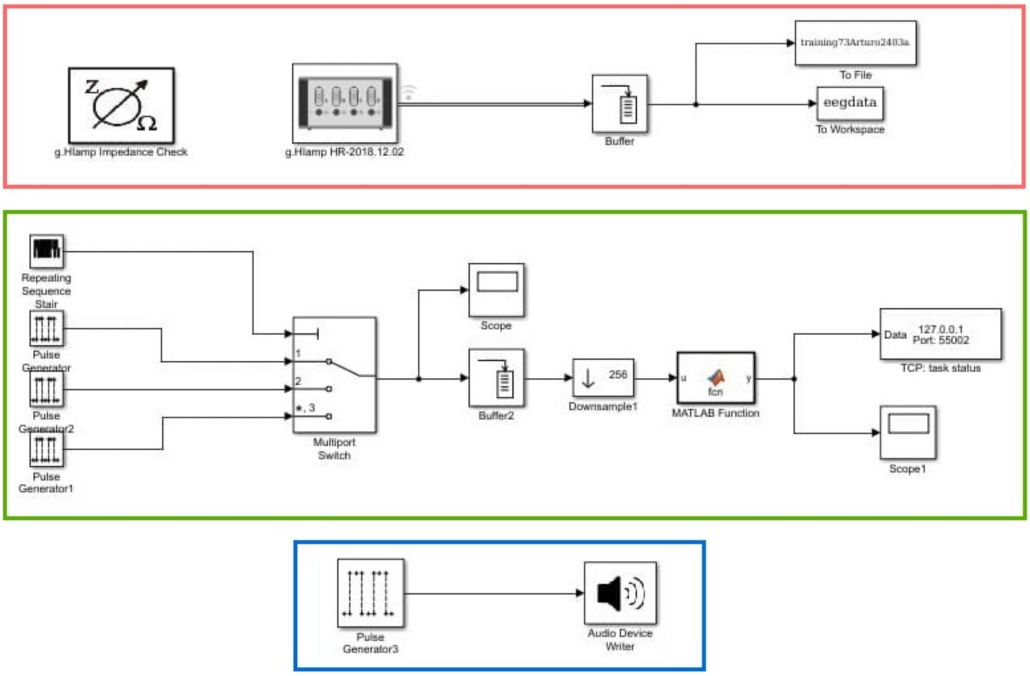

Figure 5.5: *Block scheme of the Simulink part of the interface.*

5.2.5 BCIs Enhanced via Inverse Source Techniques

A front of research investigated the usage of inverse source techniques in EEG-based BCI to improve their performance [28, 69, 70, 18, 37, 30]. To the best of our knowledge, no ground-breaking results were obtained so far with those approaches. However, if properly exploited, the usage of the bio-electrical description of the brain, should help to improve the quantity of information that a classifier can exploit to better predict the correct label. For this reason, we are convinced that

EEG source imaging (ESI) techniques, if properly used, could be a relevant help to improve the BCI performance. As mentioned in [67], in this context, ESI should be seen as a spatial filter that, by removing information that is outside the regions of interest of the classified signals, can improve the overall SNR. Indeed, we decided to explore the usage of such filters that we build via accurate brain models that we obtain with the numerical methods that are the central topic of previous sections. The usage of spatial filters could fill the gap of performance that there is between SSVEP-BCI and VI-BCI, leading to a new state-of-the-art. Unfortunately, at the moment, the achieved improvements are still minimal, but still promising, and since it is part of the current research we report some implementation details.

The first step required for ESI is the solution of the forward problem (FP), that for a certain dipole (used to model the electric activity of a cluster of neurons inside brain tissues) characterized by a position and a momentum allows to compute the associated electric potential on the scalp of a subject. The solution of the FP allows to solve the inverse problem (IP), that is the estimation of the dipoles activity starting from the electric potential recorded from the EEG [41, 46]. Several options are available for solving both the FP and the IP. For the solution of the FP problem we used a model obtained with an implementation of the BEM single layer formulation proposed in [58]. For the resolution of the IP, after having comparing performance of various techniques, we chose to adopt the Weighted Minimum Norm (WMN) inverse algorithm. Processed and windowed EEG acquisitions are filtered through session-specific narrow band-pass Chebyshev II IIR digital filters, for each trial/electrode combination. Thus, the sources of EEG signals is imaged through the WMN inverse algorithm. Consequently, during the training phase, a set of sources is selected through one-way analysis of variance (ANOVA1) statistical test, keeping the most prominent sources emerging characterized by a lower p-value, that are supposed to give an higher impact to the SNR. In conclusion, the new BCI pipeline is slightly modified with respect to fig. 5.1, adding an additional block relative to the ESI, as shown in fig. 5.6.

5.3 Numerical Results

Our result are obtained conducting experiments on one subject member of our research group (male, 23 years old). As preliminary result, fig. 5.8 shows the power spectral density analysis of the processed recordings averaged among the trials, giving a visual insight on the spectral content of VI signals. When comparing the curve in the center (background brain activity) with the top curve (VI at 5 Hz) and with the bottom one (VI at 7 Hz), it can be noticed that we have an increase of the spectral component at the task VI frequency.

Then, the performance of the full BCI pipeline are reported in terms of classification accuracy of the model on both the training and testing datasets. The

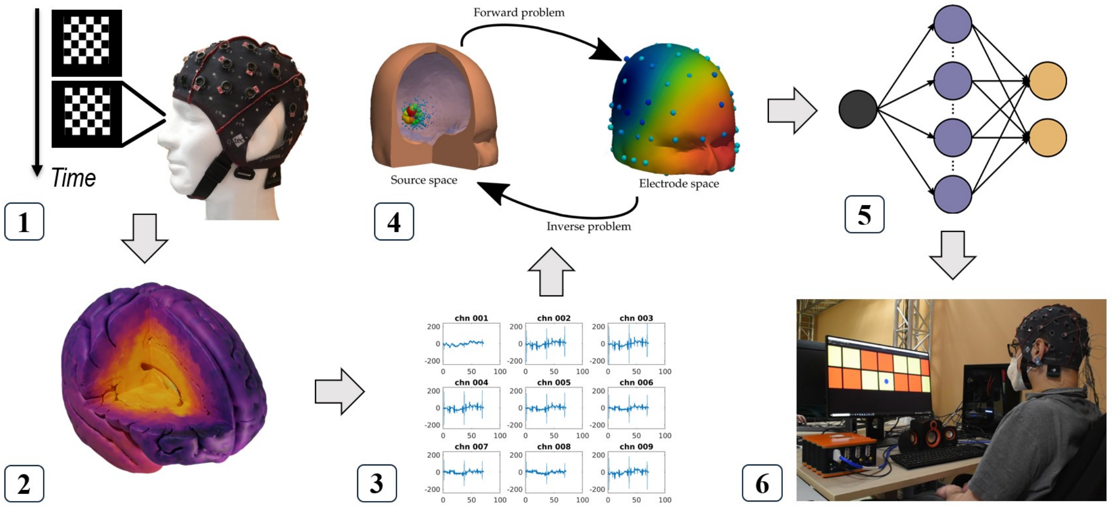

Figure 5.6: *A ESI-based BCI pipeline: (1) a subject perform a task among the ones of in a predetermined set; (2) a characteristic electric activity associated to the task is generated in the subject's brain; (3) the electric brain activity is recorded with EEG; (4) an ESI techniques are used to pass from EEG potential to the electric sources activities; (5) the electric sources activities are processed and used as feature to feed a classifier; (6) the predicted labels is used to control an interface.*

performance on all the steps of the three protocols for a collection of recordings obtained from multiple sessions are reported in table 5.1. The last two columns of table 5.1 report the size of the training and testing sets (total number of trials) for the different phases.

The initial protocol phases $1.a - 1.b$, relative to single frequency experiments with auditory co-stimuli (see section 5.2), show a prediction accuracy superior to 80% on the testing dataset. When the auditory co-stimuli are removed, in protocol phases $1.c - 1.d$, the average prediction accuracy slightly decreases, but the performance are comparable. In single frequency experiments, some of the sessions under-performed. This is probably due to the fact that in these tests we can observe that the model is over-fitting. This leaves margins for future improvements by simply better regularizing the classification algorithm. In two-frequencies sessions (protocol phase $2.a$) the accuracy attained for the test set is 72.78%, comparable to the one of the experiments including only visually imagined patterns and rest (protocol phase $3.a$), with accuracy of 71.39%. It can be noticed that an even in the most critical case a percentage above 70% is reached, a value significantly higher than the case related to random classification (33.3% for 3 classes experiments), and rendering promising the usage of the proposed VI signals for BCIs applications. In this setting the offline bit-rate is approximately 4 bits/min, following the

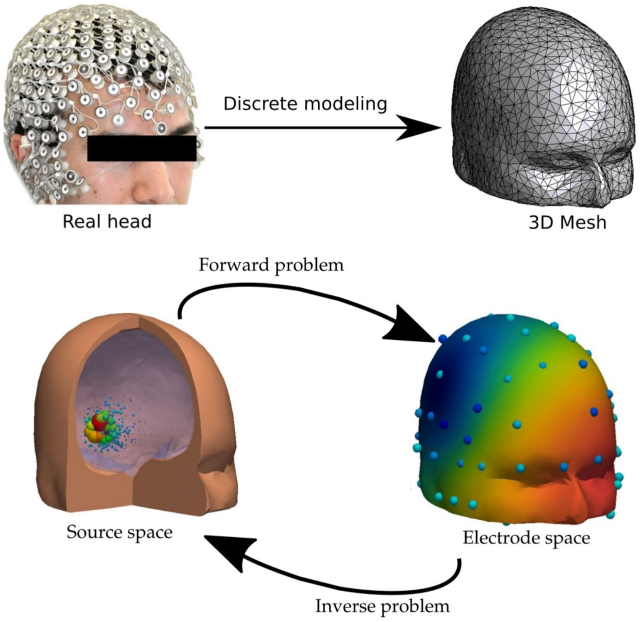

Figure 5.7: *Block scheme of the EEG source imaging procedure: the first step requires the discretizaion of the subject head in a multi-layer triangular mesh; the second step requires to use an electromagnetic solver to model the neural activity.*

Table 5.1: *Classification accuracy on training and testing sets, "Train/Test acc." and relative size of data-sets in number of trials, "Train/Test #". Table legend: "5-7 Hz w/ s.": single frequency with auditory co-stimuli; "5-7 Hz w/o s.": single frequency without auditory co-stimuli; "Mult. freq.": multiple frequencies with SSVEPs; "Pure VI": only VI multiple frequencies and rest, no visual stimuli.*

Session	**Train acc.**	**Test acc.**	**Train #**	**Test #**
5 Hz w/ s.	100.00%	81.11%	450	180
7 Hz w/ s.	96.48%	88.15%	540	270
5 Hz w/o s.	94.72%	85.00%	360	180
7 Hz w/o s.	100.00%	75.56%	450	180
Mult. freq.	91.67%	72.78%	1080	540
Pure VI	75.77%	71.39%	780	360

definition of [77]. Additional details on the performance can be obtained observing the confusion matrices reported in fig. 5.9. In particular, it can be noticed from the last experiment that the wrong guesses often involve the confusion between the two VI classes, highlighting that in any case it is possible to distinguish the VI activity

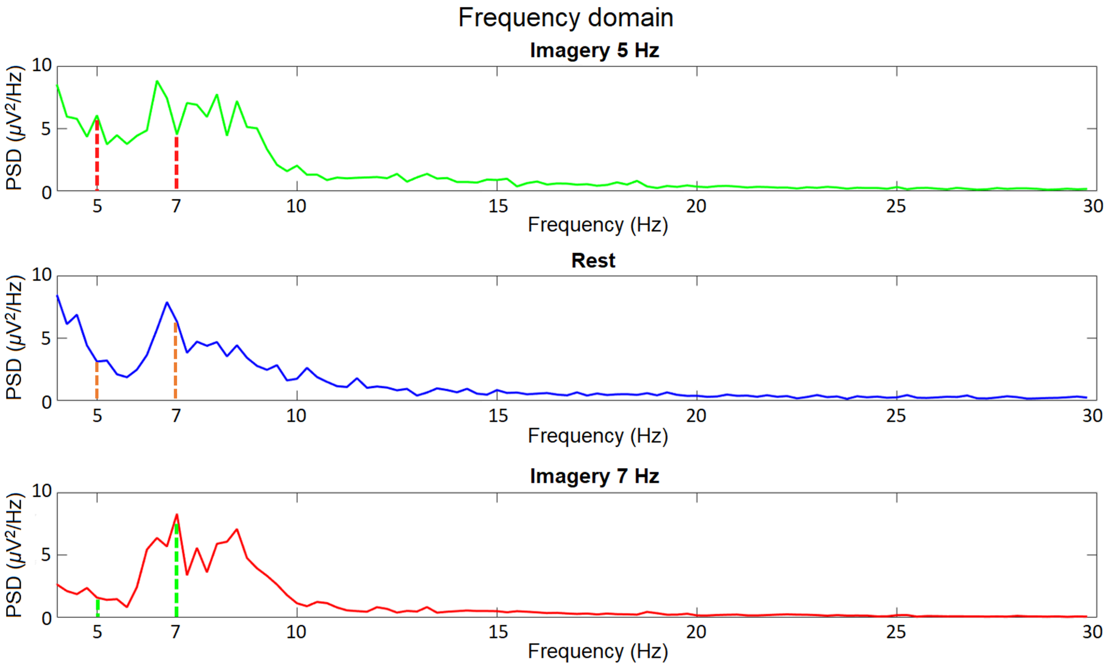

Figure 5.8: *Averaged PSD of the signals regarding the sessions involving visual imagination and rest only, acquired from the AF4 electrode. Peaks can be seen at 5 Hz and at 7 Hz.*

from the rest one.

To validate the robustness of our paradigm, additional tests were conducted on the same subject after a period of time of 9 months, during which the user did not perform further experiments. The new recordings are used as testing data-set, while as training data-set all previously recorded data are used. The so obtained results are shown in table 5.2, where, comparing with the results in table 5.1, it is visible that the accuracy even increased in most of the cases. Even if this increase is probably due to the larger size of the training dataset, the result suggests that a BCI based on VI signals would not require an extensive and continuous training. The results presented here are very preliminary and have to be confirmed by following the protocol on a larger number of subjects, and this is part of the current work.

At the moment, the usage of spatial filters based on ESI did not lead to relevant improvements of the BCI performance. However, since the preliminary results already helped us in visualizing the VI signals and the brain cortex level, we report here a sample of them. The brain leadfield was obtained with the aforementioned BEM solver, with the help of the Brainstorm MATLAB toolbox (3.4.0.0 version) for the placement of the electrodes on the head scalp. As for the head model, we used a non-linear average of 152 T1-weighted MRI scans of the brain obtained from 152 different subjects (ICBM152 template). The MRI data are segmented in the

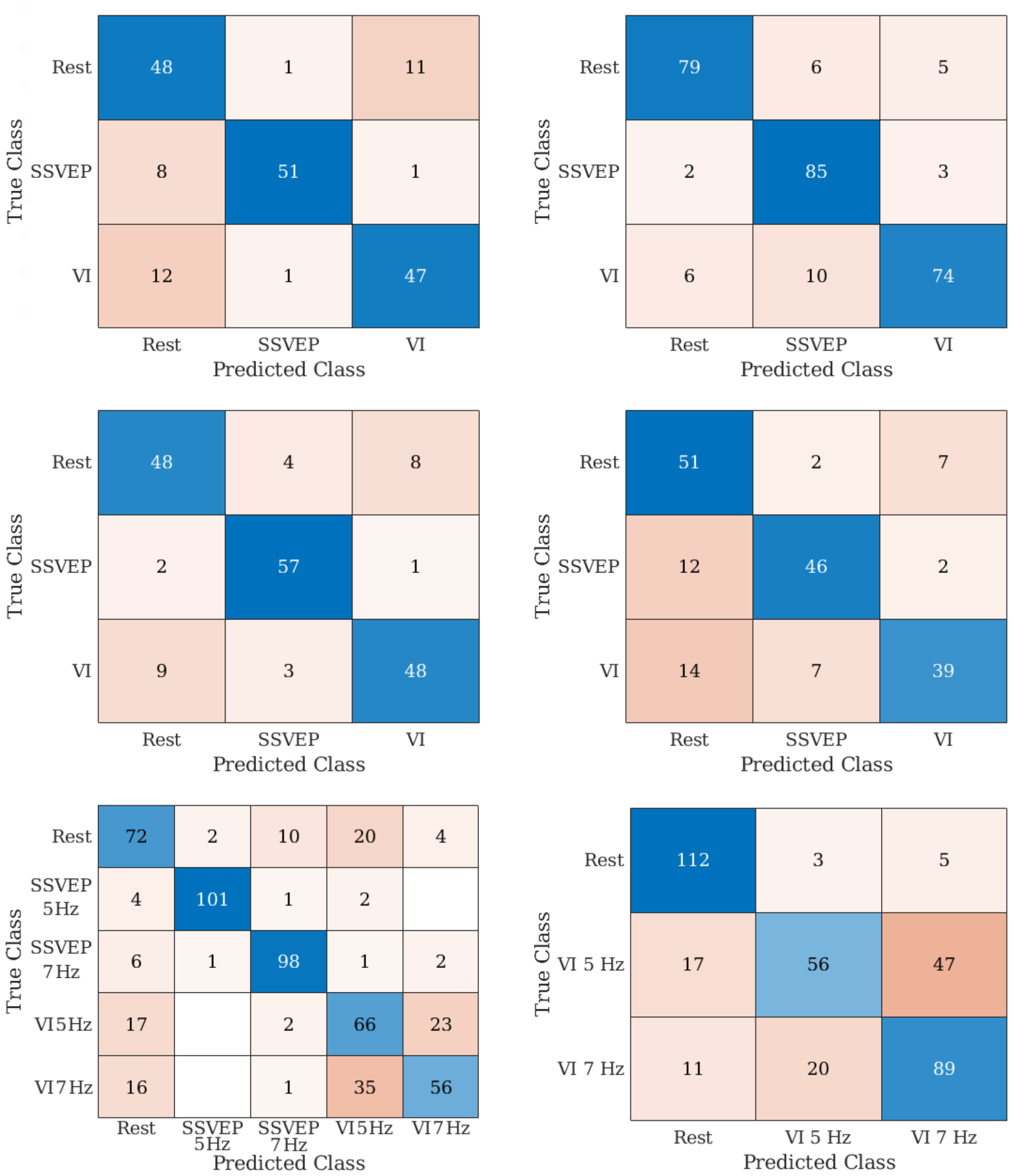

	Rest	SSVEP	VI
Rest	48	1	11
SSVEP	8	51	1
VI	12	1	47

	Rest	SSVEP	VI
Rest	79	6	5
SSVEP	2	85	3
VI	6	10	74

	Rest	SSVEP	VI
Rest	48	4	8
SSVEP	2	57	1
VI	9	3	48

	Rest	SSVEP	VI
Rest	51	2	7
SSVEP	12	46	2
VI	14	7	39

	Rest	SSVEP 5Hz	SSVEP 7Hz	VI5Hz	VI7Hz
Rest	72	2	10	20	4
SSVEP 5Hz	4	101	1	2	
SSVEP 7Hz	6	1	98	1	2
VI5Hz	17		2	66	23
VI7Hz	16		1	35	56

	Rest	VI 5 Hz	VI 7 Hz
Rest	112	3	5
VI 5 Hz	17	56	47
VI 7 Hz	11	20	89

Figure 5.9: *Confusion matrices of the classification results shown in Table 5.1. Experiments ordered from top left to bottom right follow the order used for the Table.*

different tissues and a surface mesh of multiple nested layers is obtained. For the electrodes we used an ASA $10-20$ EEG cap configuration (94 electrodes). The solver is used to build the leadfield matrix with dimensions 94×45006 (number of electrodes $\times$ number of sources for the unconstrained problem, with 3 coordinate values for every vertex). Figure 5.10 shows the dipole activity estimated inverting

Table 5.2: *Average classification accuracy for tests on the same subject after 9 months without training. Classification accuracy on training and testing sets, "Train/Test acc." and relative size of data-sets in number of trials, "Train/Test #". Table legend: "5-7 Hz w/ s.": single frequency with auditory co-stimuli; "5-7 Hz w/o s.": single frequency without auditory co-stimuli; "Mult. freq.": multiple frequencies with SSVEPs; "Pure VI": only VI multiple frequencies and rest, no visual stimuli.*

Session	Train acc.	Test acc.	Train #	Test #
5 Hz w/ s.	100.00%	82.22%	630	45
7 Hz w/ s.	95.80%	88.89%	810	45
5 Hz w/o s.	93.15%	91.11%	540	45
7 Hz w/o s.	100.00%	86.67%	630	45
Mult. freq.	89.38%	72.22%	1620	90
Pure VI	76.93%	73.33%	1140	60

with the WMN algorithm leadfield matrix and applying it to the pre-processed potentials recorded during a trial of VI signals. It can be noticed that in some areas the activity is more evident. It is difficult to validate our ESI approach because of the different opinions present in literature, but future works aim to have a functional validation of our method.

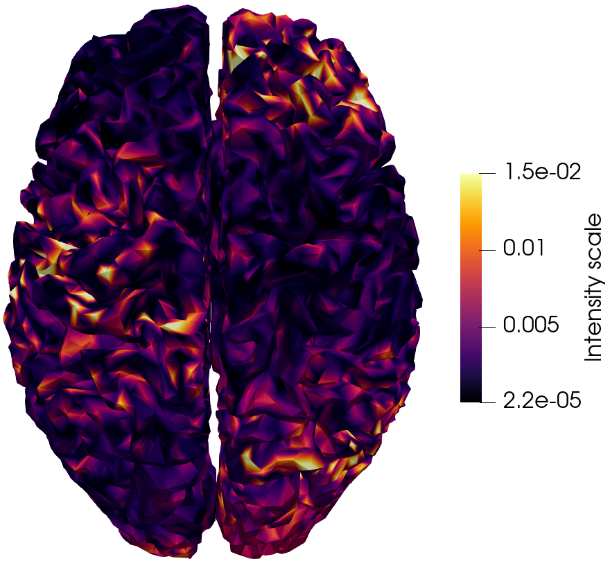

Figure 5.10: *Dipole activation obtained using ESI techniques on a trial of VI signals.*

5.4 Conclusion

In conclusion, we have seen one application of CEM techniques to BCIs. In addition, we proposed a new BCI paradigm based on flickering VI signals that overcomes the unpracticalities SSVEP BCIs. Even if the results are only preliminary, they seem quite promising, and the usage of BCI enhanced with ESI techniques could be an option to reach, or exceed, the performance of state-of-the-art BCI pipelines also in term of bit-rates, in addition to the already achieved practical advantages.

Chapter 6

Conclusion and Future Works

This work focused on the analysis, the resolution, and the application of electromagnetic integral equations. We proposed new preconditioning strategies that can cure the low-frequency and dense discretization breakdowns simultaneously. The proposed schemes rely on the new concepts of filtered Loop-Star bases and quasi-Helmholtz Laplacian filters. Preliminary results on the 3D-PEC EFIE show promising performances, leaving room for further research and extension to other applications.

In addition, we developed a new fast direct solver capable of working in the high-frequency regime on electrically large objects. The final solver results in a hierarchical-free skeleton that can be efficiently applied to several RHS. In this work, we also detailed their implementation and key concepts. Preliminary numerical results demonstrate relevant performances, especially when accelerated with fast solvers. The solver has been presented for a 2D formulation, but most of the introduced concepts apply also to 3D formulations. Indeed, extension to 3D is part of the current research.

Finally, an innovative brain-computer interfaces paradigm has been presented. The scheme, based on visual imagery signals, overcomes the drawbacks of SSVEP based BCIs that need external stimuli for their functioning. The obtained preliminary results are encouraging, and even if the performances in terms of bit-rate are still not the same of SSVEP algorithms, they are already comparable. On going research focuses on the usage of new feature extraction and classifications strategies to render the paradigm the new state-of-the-art. Among the new strategies, we are trying to create a spatial filter that by filtering out, at the brain cortex level, the component of the signals that does not contribute to functional information aims to improve the overall signal-to-noise ratio, and consequently the classification accuracy. Those spatial filters are built leveraging the solution of electromagnetic integral equations obtained with our solvers. Further developments on both the CEM solvers and the BCI fronts will jointly and reciprocally enable their advances.

Appendix A

Complementarity of the projectors

This appendix shows that $\tilde{\mathbf{P}}^{\Lambda} + \tilde{\mathbf{P}}^{\Sigma} = \mathbf{I}$ and $\tilde{\mathbb{P}}^{\Lambda} + \tilde{\mathbb{P}}^{\Sigma} = \mathbf{I}$ hold true on genus-0 geometries. Similarly to what is done in eq. (3.2), where we assume that the proper number of columns from the matrices is removed to ensure a full column rank, we prove that $\tilde{\mathbf{j}}$ can be decomposed as

$$\tilde{\mathbf{j}} = \mathbf{G}^{-\frac{1}{2}}\mathbf{j} = \tilde{\boldsymbol{\Lambda}}\tilde{\mathbf{l}} + \tilde{\boldsymbol{\Sigma}}\tilde{\mathbf{s}}, \tag{A.1}$$

in which $\tilde{\mathbf{l}}$ and $\tilde{\mathbf{s}}$ are the coefficient vectors of the normalized Loop and Star parts. Since $\mathbf{G}$, $\mathbf{G}_{\rho}$, and $\mathbf{G}_{\lambda}$ are invertible matrices, we have that $\operatorname{rank}(\tilde{\boldsymbol{\Sigma}}) = \operatorname{rank}(\boldsymbol{\Sigma})$ and $\operatorname{rank}(\tilde{\boldsymbol{\Lambda}}) = \operatorname{rank}(\boldsymbol{\Lambda})$. In addition, since $\tilde{\boldsymbol{\Lambda}}^{\mathrm{T}}\tilde{\boldsymbol{\Sigma}} = \mathbf{0}$, we also have that the columns of $\tilde{\boldsymbol{\Lambda}}$ and $\tilde{\boldsymbol{\Sigma}}$ are independent, meaning that $\operatorname{rank}([\tilde{\boldsymbol{\Lambda}}\ \tilde{\boldsymbol{\Sigma}}]) = \operatorname{rank}(\tilde{\boldsymbol{\Lambda}}) + \operatorname{rank}(\tilde{\boldsymbol{\Sigma}}) = N$, stating existence and unicity of eq. (A.1).

Now, we apply $\tilde{\boldsymbol{\Lambda}}^{\mathrm{T}}$ and $\tilde{\boldsymbol{\Sigma}}^{\mathrm{T}}$ to eq. (A.1) in order to express $\tilde{\mathbf{j}}$ in the two different bases

$$\tilde{\boldsymbol{\Lambda}}^{\mathrm{T}}\tilde{\mathbf{j}} = \tilde{\boldsymbol{\Lambda}}^{\mathrm{T}}\tilde{\boldsymbol{\Lambda}}\tilde{\mathbf{l}}\,, \tag{A.2}$$

$$\tilde{\boldsymbol{\Sigma}}^{\mathrm{T}}\tilde{\mathbf{j}} = \tilde{\boldsymbol{\Sigma}}^{\mathrm{T}}\tilde{\boldsymbol{\Sigma}}\tilde{\mathbf{s}}\,, \tag{A.3}$$

where we used that the fact that $\tilde{\boldsymbol{\Lambda}}^{\mathrm{T}}\tilde{\boldsymbol{\Sigma}} = \mathbf{0}$ and $\tilde{\boldsymbol{\Sigma}}^{\mathrm{T}}\tilde{\boldsymbol{\Lambda}} = \mathbf{0}$, as stated in eq. (3.13). At this point, the coefficients of the normalized Loop and Star bases can be expressed as a function of $\tilde{\mathbf{j}}$

$$\tilde{\mathbf{l}} = \left(\tilde{\boldsymbol{\Lambda}}^{\mathrm{T}}\tilde{\boldsymbol{\Lambda}}\right)^{+}\tilde{\boldsymbol{\Lambda}}^{\mathrm{T}}\tilde{\mathbf{j}}\,, \tag{A.4}$$

$$\tilde{\mathbf{s}} = \left(\tilde{\boldsymbol{\Sigma}}^{\mathrm{T}}\tilde{\boldsymbol{\Sigma}}\right)^{+}\tilde{\boldsymbol{\Sigma}}^{\mathrm{T}}\tilde{\mathbf{j}}\,. \tag{A.5}$$

Finally, applying $\tilde{\mathbf{\Lambda}}$ and $\tilde{\mathbf{\Sigma}}$ to eq. (A.4) and eq. (A.5) we obtain a new set of normalized projectors

$$\tilde{\mathbf{\Lambda}}\tilde{\mathbf{l}} = \tilde{\mathbf{\Lambda}}\left(\tilde{\mathbf{\Lambda}}^{\mathrm{T}}\tilde{\mathbf{\Lambda}}\right)^{+}\tilde{\mathbf{\Lambda}}^{\mathrm{T}}\tilde{\mathbf{j}} = \tilde{\mathbf{P}}^{\Lambda}\tilde{\mathbf{j}}, \tag{A.6}$$

$$\tilde{\mathbf{\Sigma}}\tilde{\mathbf{s}} = \tilde{\mathbf{\Sigma}}\left(\tilde{\mathbf{\Sigma}}^{\mathrm{T}}\tilde{\mathbf{\Sigma}}\right)^{+}\tilde{\mathbf{\Sigma}}^{\mathrm{T}}\tilde{\mathbf{j}} = \tilde{\mathbf{P}}^{\Sigma}\tilde{\mathbf{j}}, \tag{A.7}$$

with $\tilde{\mathbf{P}}^{\Lambda} + \tilde{\mathbf{P}}^{\Sigma} = \mathbf{I}$ by leveraging eq. (A.6), eq. (A.7), and eq. (A.1). Similarly, simply using $\tilde{\mathbb{\Lambda}}$ and $\tilde{\mathbb{\Sigma}}$ in the initial decomposition, it can be shown that also $\tilde{\mathbb{P}}^{\Lambda} + \tilde{\mathbb{P}}^{\Sigma} = \mathbf{I}$ holds true.

List of Symbols

Abbreviations

1D	One dimension/dimensional
2D	Two dimension/dimensional
3D	Three dimension/dimensional
ADLP	Adjoint Double Layer Potential
BC	Buffa-Christiansen
BCI	Brain Computer Interface
BEM	Boundary Element Method
BIO	Boundary Integral Operator
CEM	Computational ElectroMagnetics
CFIE	Combined Field Integral Equation
DLP	Double Layer Potential
EEG	ElectroEncephaloGraphy
EFIE	Electric Field Integral Equation
ESI	EEG Source Imaging
FDS	Fast Direct Solver
FEM	Finite Element Method
FFT	Fast Fourier Transform
HS	HyperSingular
IFFT	Inverse Fast Fourier Transform

LHS	Left Hand Side
MFIE	Magnetic Field Integral Equation
MoM	Method of Moments
MVP	Matrix Vector Product
PEC	Perfect Electric Conductor
PML	Perfectly Matched Layer
PSD	Power Spectral Density
RHS	Right Hand Side
RWG	Rao-Wilton-Glisson
SLP	Single Layer Potential
SNR	Signal-to-Noise Ratio
SSVEP	Steady-State Visually Evoked Potentials
SVD	Singular Value Decomposition
SVM	Support Vector Machine
TE	Transverse Electric
TM	Transverse Magnetic
VI	Visual Imagery
VIE	Volume Integral Equation
WMN	Weighed Minimum Norm

Functions

G	Green's function
G_0	Green's function in statics

Matrices

$\mathbf{I}$	Identity matrix
$\mathbf{O}$	General MoM matrix of an integral operator

Notations

a, b	Scalar in $\mathbb{C}$
$\mathbf{a}, \mathbf{b}$	Vector in $\mathbb{C}^m$
$\mathbf{A}, \mathbf{B}$	Matrix in $\mathbb{C}^{m\times n}$
$(\mathbf{A})_{mn}$	Element (m, n) of $\mathbf{A}$
$\mathbf{A}^\dagger, \mathbf{b}^\dagger$	Conjugate-transpose of $\mathbf{A}$, $\mathbf{b}$
$\mathbf{A}^\mathrm{T}, \mathbf{b}^\mathrm{T}$	Transpose of $\mathbf{A}$, $\mathbf{b}$
$\mathbf{A}^{-1}$	Matrix inverse of $\mathbf{A}$
$\mathbf{A}^{+}$	Moore-Penrose pseudo inverse of $\mathbf{A}$
$\Re$, $\Im$	Real, imaginary part
$\|\cdot\|$	Euclidean norm or matrix spectral norm
$\nabla \times \mathbf{A}$	Curl of $\mathbf{A}$
$\nabla \cdot \mathbf{A}$	Divergence of $\mathbf{A}$
$\nabla\Phi$	Gradient of Φ
∇^2, Δ	Laplace operator
$\mathcal{O}$	Big-O Landau symbol

Physical Quantities

ϵ, ϵ_0, ϵ_r	Electric permittivity, of the vacuum (F/m), relative
μ, μ_0, μ_r	Magnetic permeability, of the vacuum (H/m), relative
η	Characteristic impedance of the vacum (Ω)
f	Frequency (Hz)
ω	Angular frequency (rad/s)
λ	Wavelength (m)
k	Wave number (rad/m)
c	Speed of light (m/s)

Other Quantities

$\hat{\boldsymbol{n}}$	Unit normal vector
$\hat{\boldsymbol{t}}$	Unit tangent vector
h	Average mesh element edge length (m)
$\sigma_n(\mathbf{A})$	Nth singular value of $\mathbf{A}$

Bibliography

[1] Robert J Adams. "Combined field integral equation formulations for electromagnetic scattering from convex geometries". In: *IEEE transactions on antennas and propagation* 52.5 (2004), pp. 1294–1303.

[2] Robert J. Adams, Yuan Xu, Xin Xu, Jun-shik Choi, Stephen D. Gedney, and Francis X. Canning. "Modular Fast Direct Electromagnetic Analysis Using Local-Global Solution Modes". In: *IEEE Transactions on Antennas and Propagation* 56.8 (Aug. 2008), pp. 2427–2441. ISSN: 0018-926X. DOI: `10.1109/TAP.2008.926769`.

[3] S.B. Adrian, F.P. Andriulli, and T.F. Eibert. "A Hierarchical Preconditioner for the Electric Field Integral Equation on Unstructured Meshes Based on Primal and Dual Haar Bases". In: *Journal of Computational Physics* 330 (Feb. 2017), pp. 365–379. ISSN: 00219991. DOI: `10.1016/j.jcp.2016.11.013`.

[4] S.B. Adrian, F.P. Andriulli, and T.F. Eibert. "On a Refinement-Free Calderón Multiplicative Preconditioner for the Electric Field Integral Equation". In: *Journal of Computational Physics* (Oct. 2018). ISSN: 00219991. DOI: `10.1016/j.jcp.2018.10.009`.

[5] Simon B Adrian, Alexandre Dely, Davide Consoli, Adrien Merlini, and Francesco P Andriulli. "Electromagnetic integral equations: Insights in conditioning and preconditioning". In: *IEEE Open Journal of Antennas and Propagation* (2021).

[6] Simon B. Adrian, Alexandre Dély, Davide Consoli, Adrien Merlini, and Francesco P. Andriulli. "Electromagnetic Integral Equations: Insights in Conditioning and Preconditioning". In: *IEEE Open Journal of Antennas and Propagation* 2 (2021), pp. 1143–1174. ISSN: 2637-6431. DOI: `10.1109/OJAP.2021.3121097`.

[7] Francesco P Andriulli. "Loop-Star and Loop-Tree Decompositions: Analysis and Efficient Algorithms". In: *IEEE Transactions on Antennas and Propagation* 60.5 (2012), pp. 2347–2356.

[8] Francesco P Andriulli, Kristof Cools, Hakan Bagci, Femke Olyslager, Annalisa Buffa, Snorre Christiansen, and Eric Michielssen. “A Multiplicative Calderon Preconditioner for the Electric Field Integral Equation”. In: *IEEE Transactions on Antennas and Propagation* 56.8 (2008), pp. 2398–2412.

[9] Francesco P Andriulli, Kristof Cools, Ignace Bogaert, and Eric Michielssen. “On a well-conditioned electric field integral operator for multiply connected geometries”. In: *IEEE transactions on antennas and propagation* 61.4 (2012), pp. 2077–2087.

[10] Francesco P. Andriulli. “Loop-Star and Loop-Tree Decompositions: Analysis and Efficient Algorithms”. In: *IEEE Transactions on Antennas and Propagation* 60.5 (May 2012), pp. 2347–2356. ISSN: 0018-926X, 1558-2221. DOI: `10.1109/TAP.2012.2189723`.

[11] Francesco P. Andriulli, Ignace Bogaert, and Kristof Cools. “On the High Frequency Behavior and Stabilization of a Preconditioned and Resonance-Free Formulation”. In: *2015 International Conference on Electromagnetics in Advanced Applications (ICEAA)*. Sept. 2015, pp. 1321–1324. DOI: `10.1109/ICEAA.2015.7297331`.

[12] Francesco P. Andriulli, Kristof Cools, Ignace Bogaert, and Eric Michielssen. “On a Well-Conditioned Electric Field Integral Operator for Multiply Connected Geometries”. In: *IEEE Transactions on Antennas and Propagation* 61.4 (Apr. 2013), pp. 2077–2087. ISSN: 0018-926X, 1558-2221. DOI: `10.1109/TAP.2012.2234072`.

[13] Douglas N Arnold, Pavel B Bochev, Richard B Lehoucq, Roy A Nicolaides, and Mikhail Shashkov. *Compatible spatial discretizations*. Vol. 142. Springer Science & Business Media, 2007.

[14] Steven F Ashby, Thomas A Manteuffel, and James S Otto. “A comparison of adaptive Chebyshev and least squares polynomial preconditioning for Hermitian positive definite linear systems”. In: *SIAM Journal on Scientific and Statistical Computing* 13.1 (1992), pp. 1–29.

[15] Husnaini Azmy and Norlaili Mat Safri. “EEG based BCI using visual imagery task for robot control”. In: *Jurnal Teknologi (Sciences and Engineering)* 61.2 SUPPL (2013), pp. 7–11. ISSN: 01279696. DOI: `10.11113/jt.v61.1628`.

[16] Mario Bebendorf. “A Note on the Poincaré Inequality for Convex Domains”. In: *Zeitschrift für Analysis und ihre Anwendungen* (2003), pp. 751–756. ISSN: 0232-2064. DOI: `10.4171/ZAA/1170`.

[17] Bernhard Beckermann and Arno BJ Kuijlaars. “Superlinear CG convergence for special right-hand sides.” In: *ETNA. Electronic Transactions on Numerical Analysis [electronic only]* 14 (2002), pp. 1–19.

[18] Michel Besserve, Jacques Martinerie, and Line Garnero. "Improving quantification of functional networks with EEG inverse problem: Evidence from a decoding point of view". In: *NeuroImage* 55.4 (2011), pp. 1536–1547. ISSN: 1053-8119. DOI: https://doi.org/10.1016/j.neuroimage.2011.01.056. URL: http://www.sciencedirect.com/science/article/pii/S1053811911000929.

[19] Thomas E Booth. "Power iteration method for the several largest eigenvalues and eigenfunctions". In: *Nuclear science and engineering* 154.1 (2006), pp. 48–62.

[20] Yassine Boubendir and Catalin Turc. "Well-Conditioned Boundary Integral Equation Formulations for the Solution of High-Frequency Electromagnetic Scattering Problems". In: *Computers & Mathematics with Applications* 67.10 (June 2014), pp. 1772–1805. ISSN: 08981221. DOI: 10.1016/j.camwa.2014.04.003.

[21] Annalisa Buffa and Snorre Christiansen. "A Dual Finite Element Complex on the Barycentric Refinement". In: *Mathematics of Computation* 76.260 (2007), pp. 1743–1769.

[22] Wenwen Chai and Dan Jiao. "An H2-Matrix-Based Integral-Equation Solver of Reduced Complexity and Controlled Accuracy for Solving Electrodynamic Problems". In: *IEEE transactions on antennas and propagation* 57.10 (2009), pp. 3147–3159.

[23] Chih-Chung Chang and Chih-Jen Lin. "LIBSVM: A library for support vector machines". In: *ACM Transactions on Intelligent Systems and Technology* 2 (3 2011). Software available at http://www.csie.ntu.edu.tw/~cjlin/libsvm, 27:1–27:27.

[24] Q. Chen and D.R. Wilton. "Electromagnetic Scattering by Three-Dimensional Arbitrary Complex Material/Conducting Bodies". In: *Antennas and Propagation Society International Symposium, 1990. AP-S. Merging Technologies for the 90's. Digest.* May 1990, 590–593 vol.2. DOI: 10.1109/APS.1990.115179.

[25] Xiaogang Chen, Zhikai Chen, Shangkai Gao, and Xiaorong Gao. "A high-ITR SSVEP-based BCI speller". In: *Brain-Computer Interfaces* 1.3-4 (2014), pp. 181–191. ISSN: 23262621. DOI: 10.1080/2326263X.2014.944469.

[26] Xiaogang Chen, Yijun Wang, Masaki Nakanishi, Xiaorong Gao, Tzyy Ping Jung, and Shangkai Gao. "High-speed spelling with a noninvasive brain-computer interface". In: *Proceedings of the National Academy of Sciences of the United States of America* 112.44 (2015), E6058–E6067. ISSN: 10916490. DOI: 10.1073/pnas.1508080112.

[27] Snorre H Christiansen and Jean-Claude Nédélec. “A Preconditioner for the Electric Field Integral Equation Based on Calderon Formulas”. In: *SIAM Journal on Numerical Analysis* 40.3 (2002), pp. 1100–1135.

[28] Febo Cincotti, Donatella Mattia, Fabio Aloise, Simona Bufalari, Laura Astolfi, Fabrizio De Vico Fallani, Andrea Tocci, Luigi Bianchi, Maria Grazia Marciani, Shangkai Gao, Jose Millan, and Fabio Babiloni. “High-resolution EEG techniques for brain-computer interface applications”. In: *Journal of Neuroscience Methods* 167.1 (2008). Brain-Computer Interfaces (BCIs), pp. 31–42. ISSN: 0165-0270. DOI: `https://doi.org/10.1016/j.jneumeth.2007.06.031`.

[29] Ronald Coifman, Vladimir Rokhlin, and Stephen Wandzura. “The Fast Multipole Method for the Wave Equation: A Pedestrian Prescription”. In: *IEEE Antennas and Propagation Magazine* 35.3 (1993), pp. 7–12.

[30] Davide Consoli. “Computationally Enhanced Brain-Computer Interfaces Trained via Inverse Source Data”. PhD thesis. Politecnico di Torino, 2018.

[31] Davide Consoli, Clément Henry, Alexandre Dély, Lyes Rahmouni, John Erik Ortiz Guzman, Tiffany L. Chhim, Simon B. Adrian, Adrien Merlini, and Francesco P. Andriulli. “On the Fast Direct Solution of a Preconditioned Electromagnetic Integral Equation”. In: *2022 International Conference on Electromagnetics in Advanced Applications (ICEAA)*. 2022, pp. 193–195. DOI: `10.1109/ICEAA49419.2022.9899870`.

[32] Kristof Cools, Francesco P Andriulli, Femke Olyslager, and Eric Michielssen. “Nullspaces of MFIE and Calderón preconditioned EFIE operators applied to toroidal surfaces”. In: *IEEE Transactions on Antennas and Propagation* 57.10 (2009), pp. 3205–3215.

[33] D. Creel. “Visually evoked potentials”. In: *Handbook of Clinical Electrophysiology of Vision* (2012), pp. 19–28. DOI: `10.1007/978-3-030-30417-1_2`.

[34] Marion Darbas. “Generalized Combined Field Integral Equations for the Iterative Solution of the Three-Dimensional Maxwell Equations”. In: *Applied Mathematics Letters* 19.8 (Aug. 2006), pp. 834–839. ISSN: 08939659. DOI: `10.1016/j.aml.2005.11.005`.

[35] Aline W. De Borst, Alexander T. Sack, Bernadette M. Jansma, Fabrizio Esposito, Federico De Martino, Giancarlo Valente, Alard Roebroeck, Francesco Di Salle, Rainer Goebel, and Elia Formisano. “Integration of "what" and "where" in frontal cortex during visual imagery of scenes”. In: *NeuroImage* 60.1 (2012), pp. 47–58. ISSN: 10538119. DOI: `10.1016/j.neuroimage.2011.12.005`. URL: `http://dx.doi.org/10.1016/j.neuroimage.2011.12.005`.

[36] Arnaud Deraemaeker, Ivo Babuška, and Philippe Bouillard. "Dispersion and pollution of the FEM solution for the Helmholtz equation in one, two and three dimensions". In: *International journal for numerical methods in engineering* 46.4 (1999), pp. 471–499.

[37] Bradley J Edelman, Bryan Baxter, and Bin He. "EEG source imaging enhances the decoding of complex right-hand motor imagery tasks". In: *IEEE Transactions on Biomedical Engineering* 63.1 (2015), pp. 4–14.

[38] Martha J. Farah. "Is Visual Imagery Really Visual? Overlooked Evidence From Neuropsychology". In: *Psychological Review* 95.3 (1988), pp. 307–317. ISSN: 0033295X. DOI: `10.1037/0033-295X.95.3.307`.

[39] Jan Fostier and Femke Olyslager. "Full-wave electromagnetic scattering at extremely large 2-D objects". In: *Electronics letters* 45.5 (2009), pp. 245–246.

[40] Gene H. Golub and Charles F. Van Loan. *Matrix Computations*. Vol. 3. JHU Press, 2012.

[41] Roberta Grech, Tracey Cassar, Joseph Muscat, Kenneth P Camilleri, Simon G Fabri, Michalis Zervakis, Petros Xanthopoulos, Vangelis Sakkalis, and Bart Vanrumste. "Review on Solving the Inverse Problem in EEG Source Analysis". In: *Journal of NeuroEngineering and Rehabilitation* 5.1 (2008), p. 25. ISSN: 1743-0003. DOI: `10.1186/1743-0003-5-25`.

[42] Christoph Guger, Brendan Z. Allison, Bernhard Großwindhager, Robert Prückl, Christoph Hintermüller, Christoph Kapeller, Markus Bruckner, Gunther Krausz, and Günter Edlinger. "How many people could use an SSVEP BCI?" In: *Frontiers in Neuroscience* 6.NOV (2012), pp. 2–7. ISSN: 16624548. DOI: `10.3389/fnins.2012.00169`.

[43] Han Guo, Yang Liu, Jun Hu, and Eric Michielssen. "A Butterfly-Based Direct Integral-Equation Solver Using Hierarchical LU Factorization for Analyzing Scattering From Electrically Large Conducting Objects". In: *IEEE Transactions on Antennas and Propagation* 65.9 (Sept. 2017), pp. 4742–4750. ISSN: 1558-2221. DOI: `10.1109/TAP.2017.2727511`.

[44] Wolfgang Hackbusch and Zenon Paul Nowak. "On the Fast Matrix Multiplication in the Boundary Element Method by Panel Clustering". In: *Numerische Mathematik* 54.4 (1989), pp. 463–491.

[45] Nathan Halko, Per-Gunnar Martinsson, and Joel A Tropp. "Finding structure with randomness: Probabilistic algorithms for constructing approximate matrix decompositions". In: *SIAM review* 53.2 (2011), pp. 217–288.

[46] Hans Hallez, Bart Vanrumste, Roberta Grech, Joseph Muscat, Wim De Clercq, Anneleen Vergult, Yves D'Asseler, Kenneth P Camilleri, Simon G Fabri, Sabine Van Huffel, and Ignace Lemahieu. "Review on Solving the Forward Problem in EEG Source Analysis". In: *Journal of NeuroEngineering and Rehabilitation* 4.1 (2007), p. 46. ISSN: 1743-0003. DOI: `10.1186/1743-0003-4-46`.

[47] David K. Hammond, Pierre Vandergheynst, and Rémi Gribonval. "Wavelets on Graphs via Spectral Graph Theory". In: *Applied and Computational Harmonic Analysis* 30.2 (Mar. 2011), pp. 129–150. ISSN: 1063-5203. DOI: `10.1016/j.acha.2010.04.005`.

[48] Roger F. Harrington. *Field Computation by Moment Methods*. Wiley, May 1993. ISBN: 978-0-7803-1014-8.

[49] H. V. Henderson and S. R. Searle. "On Deriving the Inverse of a Sum of Matrices". In: *SIAM Review* 23.1 (Jan. 1981), pp. 53–60. ISSN: 0036-1445, 1095-7200. DOI: `10.1137/1023004`.

[50] N. Higham. *Functions of Matrices*. Other Titles in Applied Mathematics. Society for Industrial and Applied Mathematics, Jan. 2008. ISBN: 978-0-89871-646-7. DOI: `10.1137/1.9780898717778`.

[51] Jian-Ming Jin. *Theory and Computation of Electromagnetic Fields*. John Wiley & Sons, 2015.

[52] Jian-Ming Jin. *Theory and Computation of Electromagnetic Fields*. 2nd ed. Piscataway, NJ: IEEE Press, 2015. ISBN: 978-1-119-10804-7 978-1-119-10808-5.

[53] Olin G Johnson, Charles A Micchelli, and George Paul. "Polynomial preconditioners for conjugate gradient calculations". In: *SIAM Journal on Numerical Analysis* 20.2 (1983), pp. 362–376.

[54] Diego Kaski. "Revision: Is visual perception a requisite for visual imagery?" In: *Perception* 31.6 (2002), pp. 717–731. ISSN: 03010066. DOI: `10.1068/p3360`.

[55] Robert C Kirby. "From functional analysis to iterative methods". In: *SIAM review* 52.2 (2010), pp. 269–293.

[56] Nataliya Kosmyna, Jussi T. Lindgren, and Anatole Lécuyer. "Attending to Visual Stimuli versus Performing Visual Imagery as a Control Strategy for EEG-based Brain-Computer Interfaces". In: *Scientific Reports* 8.1 (2018), pp. 1–14. ISSN: 20452322. DOI: `10.1038/s41598-018-31472-9`.

[57] Stephen M. Kosslyn and William L. Thompson. "When Is Early Visual Cortex Activated during Visual Mental Imagery?" In: *Psychological Bulletin* 129.5 (2003), pp. 723–746. ISSN: 00332909. DOI: `10.1037/0033-2909.129.5.723`.

[58] J. Kybic, M. Clerc, T. Abboud, O. Faugeras, R. Keriven, and T. Papadopoulo. "A Common Formalism for the Integral Formulations of the Forward EEG Problem". In: *IEEE Transactions on Medical Imaging* 24.1 (Jan. 2005), pp. 12–28. ISSN: 0278-0062. DOI: `10.1109/TMI.2004.837363`.

[59] Ioulietta Lazarou, Spiros Nikolopoulos, Panagiotis C. Petrantonakis, Ioannis Kompatsiaris, and Magda Tsolaki. "EEG-based brain–computer interfaces for communication and rehabilitation of people with motor impairment: A novel approach of the 21st century". In: *Frontiers in Human Neuroscience* 12.January (2018), pp. 1–18. ISSN: 16625161. DOI: `10.3389/fnhum.2018.00014`.

[60] D. Le Bihan, R. Turner, T. A. Zeffiro, C. A. Cuenod, P. Jezzard, and V. Bonnerot. "Activation of human primary visual cortex during visual recall: A magnetic resonance imaging study". In: *Proceedings of the National Academy of Sciences of the United States of America* 90.24 (1993), pp. 11802–11805. ISSN: 00278424. DOI: `10.1073/pnas.90.24.11802`.

[61] Seo Hyun Lee, Minji Lee, Ji Hoon Jeong, and Seong Whan Lee. "Towards an EEG-based intuitive BCI communication system using imagined speech and visual imagery". In: *Conference Proceedings - IEEE International Conference on Systems, Man and Cybernetics* 2019-October (2019), pp. 4409–4414. ISSN: 1062922X. DOI: `10.1109/SMC.2019.8914645`.

[62] Ron Levie, Federico Monti, Xavier Bresson, and Michael M Bronstein. "Cayleynets: Graph convolutional neural networks with complex rational spectral filters". In: *IEEE Transactions on Signal Processing* 67.1 (2018), pp. 97–109.

[63] Jörg Liesen and Zdenek Strakos. *Krylov subspace methods: principles and analysis*. Oxford University Press, 2013.

[64] J. S. Lim, S. Rao, and D. R. Wilton. "A Novel Technique to Calculate the Electromagnetic Scattering by Surfaces of Arbitrary Shape". In: *1993 URSI Radio Science Meeting Digest*. 1993, p. 322.

[65] Jussi T. Lindgren, Adrien Merlini, Anatole Lecuyer, and Francesco P. Andriulli. "SimBCI-A framework for studying BCI methods by simulated EEG". In: *IEEE Transactions on Neural Systems and Rehabilitation Engineering* 26.11 (2018), pp. 2006–2105. ISSN: 15344320. DOI: `10.1109/TNSRE.2018.2873061`.

[66] Qin S Liu, Sheng Sun, and Weng Cho Chew. "A potential-based integral equation method for low-frequency electromagnetic problems". In: *IEEE transactions on antennas and Propagation* 66.3 (2018), pp. 1413–1426.

[67] F. Lotte, L. Bougrain, A. Cichocki, M. Clerc, M. Congedo, A. Rakotomamonjy, and F. Yger. “A review of classification algorithms for EEG-based brain-computer interfaces: A 10 year update”. In: *Journal of Neural Engineering* 15.3 (2018), aab2f2. ISSN: 17412552. DOI: 10.1088/1741-2552/aab2f2. URL: https://doi.org/10.1088/1741-2552/aab2f2.

[68] F. Lotte, M. Congedo, A. Lécuyer, F. Lamarche, and B. Arnaldi. “A review of classification algorithms for EEG-based brain-computer interfaces”. In: *Journal of Neural Engineering* 4.2 (2007). ISSN: 17412560. DOI: 10.1088/1741-2560/4/2/R01.

[69] F. Lotte, A. Lecuyer, and B. Arnaldi. “FuRIA: A Novel Feature Extraction Algorithm for Brain-Computer Interfaces using Inverse Models and Fuzzy Regions of Interest”. In: *2007 3rd International IEEE/EMBS Conference on Neural Engineering*. May 2007, pp. 175–178. DOI: 10.1109/CNE.2007.369640.

[70] F. Lotte, A. Lecuyer, and B. Arnaldi. “FuRIA: An Inverse Solution Based Feature Extraction Algorithm Using Fuzzy Set Theory for Brain-Computer Interfaces”. In: *IEEE Transactions on Signal Processing* 57.8 (Sept. 2009), pp. 3253–3263. ISSN: 1053-587X. DOI: 10.1109/TSP.2009.2020752.

[71] Nikolay V. Manyakov, Nikolay Chumerin, and Marc M. Van Hulle. “Multichannel decoding for phase-coded SSVEP brain-computer interface”. In: *International Journal of Neural Systems* 22.5 (2012), pp. 1–8. ISSN: 01290657. DOI: 10.1142/S0129065712500220.

[72] David F. Marks and Anne R. Isaac. “Topographical distribution of EEG activity accompanying visual and motor imagery in vivid and non-vivid imagers”. In: *British Journal of Psychology* 86.2 (1995), pp. 271–282. ISSN: 20448295. DOI: 10.1111/j.2044-8295.1995.tb02561.x.

[73] Pablo Martinez, Hovagim Bakardjian, and Andrzej Cichocki. “Fully online multicommand brain-computer interface with visual neurofeedback using SSVEP paradigm”. In: *Computational Intelligence and Neuroscience* 2007.i (2007). ISSN: 16875265. DOI: 10.1155/2007/94561.

[74] J Mautz and R Harrington. “A combined-source solution for radiation and scattering from a perfectly conducting body”. In: *IEEE Transactions on Antennas and Propagation* 27.4 (1979), pp. 445–454.

[75] J Mautz and R Harrington. “An E-field solution for a conducting surface small or comparable to the wavelength”. In: *IEEE Transactions on Antennas and Propagation* 32.4 (1984), pp. 330–339.

[76] J. Mautz and R. Harrington. “An E-field Solution for a Conducting Surface Small or Comparable to the Wavelength”. In: *IEEE Transactions on Antennas and Propagation* 32.4 (1984), pp. 330–339.

[77] Dennis J McFarland and Jonathan R Wolpaw. "Brain-computer interfaces for communication and control". In: *Communications of the ACM* 54.5 (2011), pp. 60–66.

[78] William McLean and William Charles Hector McLean. *Strongly elliptic systems and boundary integral equations*. Cambridge university press, 2000.

[79] Adrien Merlini, Yves Beghein, Kristof Cools, Eric Michielssen, and Francesco P Andriulli. "Magnetic and Combined Field Integral Equations Based on the Quasi-Helmholtz Projectors". In: *IEEE Transactions on Antennas and Propagation* (2020).

[80] Adrien Merlini, Clément Henry, Davide Consoli, Lyes Rahmouni, Alexandre Dély, and Francesco P. Andriulli. "Laplacian Filtered Loop-Star Decompositions and Quasi-Helmholtz Laplacian Filters: Definitions, Analysis, and Efficient Algorithms". en. In: arXiv:2211.07704 (Nov. 2022). arXiv:2211.07704 [cs, math]. URL: http://arxiv.org/abs/2211.07704.

[81] Micheli. "Transition from Visually Evoked to Purely Imagined Steady State Potentials in Brain-Computer Interfaces: Computational Schemes and Feasibility Assessments". In: *Politecnico di Torino* (2021).

[82] Arturo Micheli, Davide Consoli, Adrien Merlini, Paolo Ricci, and Francesco Andriulli. "Brain-Computer Interfaces: Investigating the Transition from Visually Evoked to Purely Imagined Steady-State Potentials". In: (Apr. 2022).

[83] Eric Michielssen and Amir Boag. "A Multilevel Matrix Decomposition Algorithm for Analyzing Scattering from Large Structures". In: *IEEE Transactions on Antennas and Propagation* 44.8 (1996), pp. 1086–1093.

[84] R. Mitharwal and F.P. Andriulli. "On the Multiplicative Regularization of Graph Laplacians on Closed and Open Structures With Applications to Spectral Partitioning". In: *IEEE Access* 2 (2014), pp. 788–796. ISSN: 2169-3536. DOI: 10.1109/ACCESS.2014.2345657.

[85] Jean-Claude Nedelec. *Acoustic and Electromagnetic Equations: Integral Representations for Harmonic Problems*. Springer Science & Business Media, Mar. 2001. ISBN: 978-0-387-95155-3.

[86] Luis Fernando Nicolas-alonso and Jaime Gomez-gil. "Brain Computer Interfaces, a Review". In: *Sensors* January (2012), pp. 1211–1279. ISSN: 14248220. DOI: 10.3390/s120201211.

[87] Michael O'Neil. "Second-Kind Integral Equations for the Laplace-Beltrami Problem on Surfaces in Three Dimensions". In: *Advances in Computational Mathematics* 44.5 (Oct. 2018), pp. 1385–1409. ISSN: 1572-9044. DOI: 10.1007/s10444-018-9587-7.

[88] Christopher C Paige. “Computational variants of the Lanczos method for the eigenproblem”. In: *IMA Journal of Applied Mathematics* 10.3 (1972), pp. 373–381.

[89] William H. Press. *Numerical Recipes 3rd Edition: The Art of Scientific Computing*. Cambridge University Press, Sept. 2007. ISBN: 978-0-521-88068-8.

[90] Zhi Guo Qian and Weng Cho Chew. “An augmented electric field integral equation for high-speed interconnect analysis”. In: *Microwave and Optical Technology Letters* 50.10 (2008), pp. 2658–2662.

[91] Luis Garcia Ramos and Reinhard Nabben. “A two-level shifted Laplace preconditioner for Helmholtz problems: Field-of-values analysis and wavenumber-independent convergence”. In: *arXiv preprint arXiv:2006.08750* (2020).

[92] Sadasiva M Rao, Donald R Wilton, and Allen W Glisson. “Electromagnetic Scattering by Surfaces of Arbitrary Shape”. In: *IEEE Transactions on Antennas and Propagation* 30.3 (1982), pp. 409–418.

[93] P. E. Roland and B. Gulyás. “Visual imagery and visual representation”. In: *Trends in Neurosciences* 17.7 (1994), pp. 281–287. ISSN: 01662236. DOI: `10.1016/0166-2236(94)90057-4`.

[94] Youcef Saad and Martin H Schultz. “GMRES: A generalized minimal residual algorithm for solving nonsymmetric linear systems”. In: *SIAM Journal on scientific and statistical computing* 7.3 (1986), pp. 856–869.

[95] Sabbah, Simond G, Levrier O, Habib M, Trabaud V, Murayama N, Mazoyer BM, Briant JF, Raybaud C, and Salamon G. “Functional magnetic resonance imaging at 1.5 T during sensorimotor and cognitive task”. In: *European Neurology* 35 (1995), pp. 131–136. DOI: `10.1159/000117108`.

[96] Stefan A Sauter and Christoph Schwab. “Boundary element methods”. In: *Boundary Element Methods*. Springer, 2010, pp. 183–287.

[97] Arkadi Sharshevsky, Yaniv Brick, and Amir Boag. “Direct Solution of Scattering Problems Using Generalized Source Integral Equations”. In: *IEEE Transactions on Antennas and Propagation* 68.7 (July 2020), pp. 5512–5523. ISSN: 1558-2221. DOI: `10.1109/TAP.2020.2975549`.

[98] Jonathan Richard Shewchuk et al. *An introduction to the conjugate gradient method without the agonizing pain*. 1994.

[99] Scott D. Slotnick, William L. Thompson, and Stephen M. Kosslyn. “Visual memory and visual mental imagery recruit common control and sensory regions of the brain”. In: *Cognitive Neuroscience* 3.1 (2012), pp. 14–20. ISSN: 17588928. DOI: `10.1080/17588928.2011.578210`.

[100] Peter Sonneveld. "CGS, a fast Lanczos-type solver for nonsymmetric linear systems". In: *SIAM journal on scientific and statistical computing* 10.1 (1989), pp. 36–52.

[101] Teresa Sousa, Carlos Amaral, João Andrade, Gabriel Pires, Urbano J. Nunes, and Miguel Castelo-Branco. "Pure visual imagery as a potential approach to achieve three classes of control for implementation of BCI in non-motor disorders". In: *Journal of Neural Engineering* 14.4 (2017). ISSN: 17412552. DOI: `10.1088/1741-2552/aa70ac`.

[102] Klaus Stüben. "A review of algebraic multigrid". In: *Numerical Analysis: Historical Developments in the 20th Century* (2001), pp. 331–359.

[103] Jiabei Tang, Minpeng Xu, Jin Han, Miao Liu, Tingfei Dai, Shanguang Chen, and Dong Ming. "Optimizing SSVEP-Based BCI System towards Practical High-Speed Spelling". In: *Sensors* 20.15 (2020). ISSN: 1424-8220. DOI: `10.3390/s20154186`. URL: `https://www.mdpi.com/1424-8220/20/15/4186`.

[104] Matti Taskinen and Pasi Yla-Oijala. "Current and charge integral equation formulation". In: *IEEE Transactions on Antennas and Propagation* 54.1 (2006), pp. 58–67.

[105] Giuseppe Vecchi. "Loop-Star Decomposition of Basis Functions in the Discretization of the EFIE". In: *IEEE Transactions on Antennas and Propagation* 47.2 (1999), pp. 339–346.

[106] Giuseppe Vecchi. "Loop-star decomposition of basis functions in the discretization of the EFIE". In: *IEEE Transactions on Antennas and Propagation* 47.2 (1999), pp. 339–346.

[107] Felipe Vico, Miguel Ferrando, Leslie Greengard, and Zydrunas Gimbutas. "The decoupled potential integral equation for time-harmonic electromagnetic scattering". In: *Communications on Pure and Applied Mathematics* 69.4 (2016), pp. 771–812.

[108] D. R. Wilton. "Topological Consideration in Surface Patch and Volume Cell Modeling of Electromagnetic Scatterers". In: *Proc. URSI Int. Symp. Electromagn. Theory.* 1983, pp. 65–68.

[109] Wolpaw. *Brain-Computer Interfaces Principles and Practice.* Vol. 53. Oxford University Press, 2012, pp. 1689–1699. ISBN: 9788578110796. arXiv: `arXiv:1011.1669v3`.

[110] A.C. Woo, H.T.G. Wang, M.J. Schuh, and M.L. Sanders. "EM Programmer's Notebook-Benchmark Radar Targets for the Validation of Computational Electromagnetics Programs". In: *IEEE Antennas and Propagation Magazine* 35.1 (Feb. 1993), pp. 84–89. ISSN: 1558-4143. DOI: `10.1109/74.210840`.

[111] Wen-Liang Wu, Allen W. Glisson, and Darko Kajfez. “A Study of Two Numerical Solution Procedures for the Electric Field Integral Equation at Low Frequency”. In: *Applied Computational Electromagnetics Society Journal* 10.3 (1995), pp. 69–80.

[112] Brendan Z. Allison, Jing Jin, Yu Zhang, and Xingyu Wang. “A four-choice hybrid P300/SSVEP BCI for improved accuracy”. In: *Brain-Computer Interfaces* 1.1 (2014), pp. 17–26. ISSN: 23262621. DOI: `10.1080/2326263X.2013.869003`.

[113] Jun-Sheng Zhao and Weng Cho Chew. “Integral Equation Solution of Maxwell’s Equations from Zero Frequency to Microwave Frequencies”. In: *Antennas and Propagation, IEEE Transactions on* 48.10 (2000), pp. 1635–1645.

[114] K. Zhao, M.N. Vouvakis, and J.-F. Lee. “The Adaptive Cross Approximation Algorithm for Accelerated Method of Moments Computations of EMC Problems”. In: *IEEE Transactions on Electromagnetic Compatibility* 47.4 (Nov. 2005), pp. 763–773. ISSN: 0018-9375. DOI: `10.1109/TEMC.2005.857898`.

This Ph.D. thesis has been typeset by means of the TEX-system facilities. The typesetting engine was pdfLATEX. The document class was `toptesi`, by Claudio Beccari, with option `tipotesi=scudo`. This class is available in every up-to-date and complete TEX-system installation.